Multiscale Models of Neural Tissue

Funda Catan, MSc

Thesis submitted to the University of Nottingham

for the degree of Master of Philosophy

June 2016

Abstract

The brain is a complex system which contains a large number of neurons. This complex nature of the brain can be simplified by mathematical models. Mathematical models are almost equally as important as biological experiments and represent some part of the real world by mathematical terms. They help us to understand mathematical neuroscience. The functional dynamics of brain and the behaviour of neurons have become popular recently. Hence, mathematical neuroscience becomes an attractive prospective to study because of a large availability of biological and computation data.

In the first part of the thesis, we outline a literature review covering background material for this thesis. Neuroimaging techniques are used to understand the structure and dynamics of the brain. Then, we analyse the Liley and Janset-Rit model as the neural mass models.

After a brief and selective description of neurobiology, our study demonstrates the relationship between functional connectivity (FC) and structural connectivity (SC) via using Wilson-Cowan model. The bifurcation diagram of Wilson-Cowan model is plotted in XPP package programme. While SC is calculated from CoComac database which are taken from the macaque brain, FC is calculated by correlation. Then, the relationship between FC and SC is measured by the Pearson and Spearman correlation. A greater similarity is seen along the border of the Hopf bifurcation. Hence, phase response curves are calculated by the adjoint method, and then phase interaction functions are produced in Matlab in order to examine the stability of the synchronised solutions.

Following this, one question of interest is the relationship between epileptic discharges as measured by EEG and the haemodynamic response as measured by fMRI. The haemodynamic model is discussed and its outputs as BOLD signals are computed. Then, the haemodynamic model is coupled to the Wilson-Cowan model and the Liley model. Eventually the BOLD signals are calculated after coupling. The system has BOLD signal dynamics including an initial dip, positive response and poststimulus undershoot.

Acknowledgements

First and foremost, I would like to express my deepest gratitude to my supervisors, Prof. Stephen Coombes and Prof. Markus Owen, for their aspiring guidance, and encouragement. I am grateful to my supervisors for sharing their time and truthful views on a number of issues related to the project.

Additionally, my sincere appreciation also extends to all my family; my mother, my father, my brother and my sister. They always love and encourage me with their best wishes; understanding me throughout writing this thesis and my life in general. My research would not have completed without their supports.

I owe sincere and earnest thankfulness to my invaluable network of supportive, forgiving, generous, and loving friends, especially Mehtap Aygun and Deniz Sevinc. In order to complete my acknowledgements, a special thank goes to Goknur Yasa for her unlimited love and support. I would like to thank Ruth Smith, for her scientific views and her great humanity.

Last, but by no means least, most profuse thanks must go to the Turkish Government for giving me financial support enabling to study in UK.

Contents

List of Abbreviations

BOLD **B**lood **O**xygen **L**evel **D**ependent

EEG **E**lectroencephalography

FC **F**unctional **C**onnectivity

fMRI **F**unctional **M**agnetic **R**esonance **I**maging

GABA **G**amma-**A**mino**b**utyric **A**cid

MEG **M**agnetoencephalography

MHM **M**etabolic **H**aemodynamic **M**odel

MPC **M**ean **P**hase **C**oherence

MRI **M**agnetic **R**esonance **I**maging

NMM **N**eural **M**ass **M**odel

PIF **P**hase **I**nteraction **F**unction

PRC **P**hase **R**esponse **C**urve

SC **S**tructural **C**onnectivity

SQUID **S**uperconducting **Q**uantum **I**nterference **D**evice

Chapter 1

Introduction

This is an introductory chapter that includes a literature review covering background material for this thesis. We commence, in section 1.1 with an introduction to basic knowledge of neurobiology. Neuroimaging methods are then described in section 1.2. Section 1.3 is dedicated to basic metabolism in the brain and the use of mathematical models in neuroscience is outlined in section 1.4. Mathematical models of synapses followed by several examples of Neural Mass models are outlined in section 1.4.1. The final section of the introduction chapter presents information about the aim of this study and works of the next chapters.

1.1 Brief Overview of Relevant Neurobiology

The human brain has a nervous system which is a complex network of nerves. Neurons, first observed in detail by Santiago Ramón y Cajal, are the specialised cells for carrying signals electronically and chemically via synapses to other cells in the nervous system [62]. As shown in Figure 1.1, neurons are made up of a cell body (soma), dendrites and an axon. Dendrites, discovered by William His in 1889 [33], play the key role as input devices; they collect the electrical signals from other neurons and transmit them towards the cell body. The axon, a name coined by Rudolph Albert von Kolliker in 1896, sends signals away from the cell body to other neurons like an output device [41, 17, 87, 62]. Synapses, a term coined by Michael Foster in 1897, allow a neuron to transmit signals chemically to other cells [17, 111]. The nerve cell transmitting a signal is called the presynaptic cell, and the cell receiving signal is called the postsynaptic cell [62].

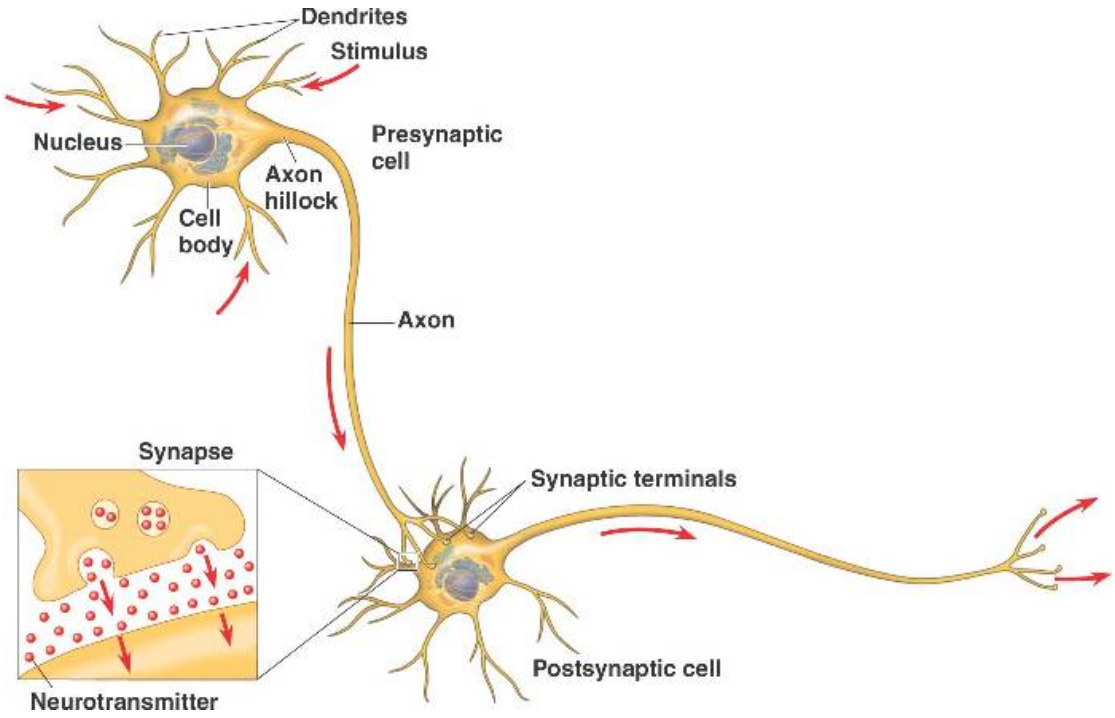

Figure 1.1: A neuron consists of a soma, dendrites and an axon. Neurotransmitter is released probabilistically at synapse in response to the arrival of an action potential. Figure is taken from [16].

.

A brain contains billions of cells. Two major types of cells in the nervous system are neurons and glia cells. Two types of neurons are inhibitory neurons and excitatory neurons. Excitatory neurons are typically pyramidal in shape. There are a large number of them, and they are morphologically similar. In contrast, inhibitory neurons have a diversity of shapes and morphologies: Cajal, known as father of modern neuroscience, described them "mariposas del alma". It means the butterflies of the soul [13]. These different subtypes express different markers and often have different patterns of firing [62]. Furthermore, while inhibitory neurons often make local connections, excitatory neurons can make long-range connections between different cortical areas. Excitatory neurons are responsible to flow the information in the brain whereas inhibitory neurons are responsible to regulate the activation of excitatory neurons. Brain functions work properly due to the special property of inhibitory neuron.

Brain chemicals, called neurotransmitters enable to transmit the signals from one neuron to the next across synapses. Glutamate (excitatory) and gamma-aminobutyric

acid (inhibitory) are the most popular neurotransmitters in the brain. They act on several different types of receptors. While glutamate has excitatory and modulatory effects, gamma-aminobutyric acid ($GABA_A$) has inhibitory effects [73, 112]. Excitatory neurons are defined as cells which release excitatory neurotransmitter such as glutamate, whereas inhibitory neurons are defined as the cells that release inhibitory neurotransmitter such as $GABA_A$. Therefore, neurotransmitters have a crucial role in all brain functions.

1.2 Neuroimaging Techniques

Neuroimaging helps to measure the brain function to understand anatomical structure of the brain and how the brain works. Neuroimaging techniques enable us to produce images of the brain without invasive surgery, incision of scalp or any part of body. They allow the noninvasive visualisation of the structure and functionality of the brain, the activity and problems within the brain. The images produced by structural imaging techniques, for illustration magnetic resonance imaging (MRI), are used to show the structure of brain, and diagnose brain injury and diseases. Moreover, the images produced by functional imaging help to understand and quantify the cognitive task of certain brain regions. They are significant tools for both research and medical diagnosis. In this section, we will consider 4 types of neuroimaging techniques, beginning with electroencephalography and magnetoencephalography in section 1.2.1.

1.2.1 EEG and MEG

Electroencephalography (EEG) is one of the functional neuroimaging techniques which is used to measure the voltage alterations generated by neural electrical activity at the surface of scalp [5, 82]. The first human electroencephalograms were recorded by Hans Berger in 1924 [43]. While temporal resolution is high for the most of EEG devices, spatial resolution is relatively low [110]. This technique is useful for understanding the behaviours of some disorders like epilepsy, schizophrenia and Alzheimer's as it is noninvasive [106].

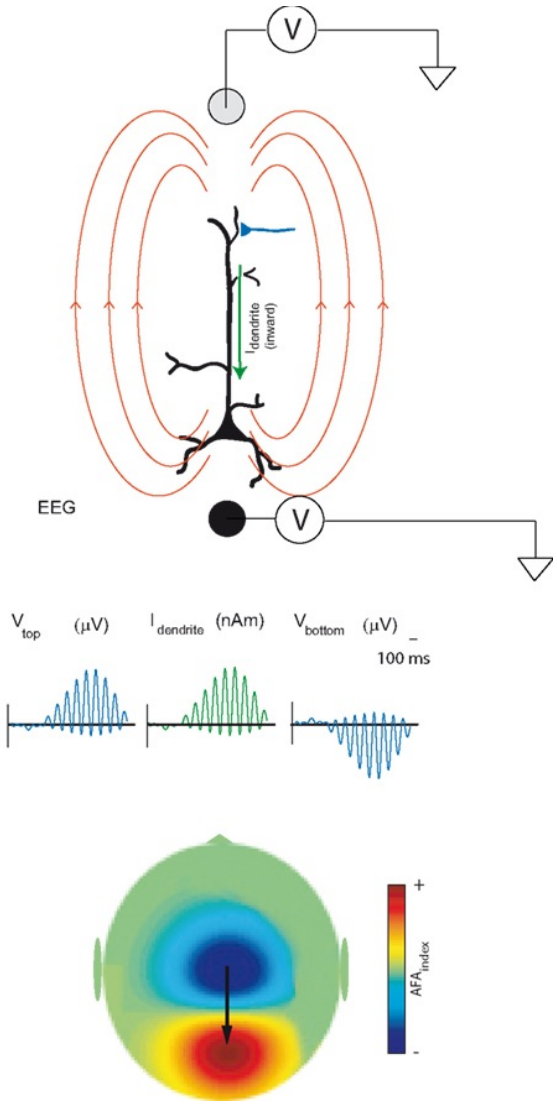

Figure 1.2: It is seen from the first part of the figure that EEG identifies the differences in scalp potentials consisted of the currents. The inward and outward direction of the currents in the dendrites detects the polarity of the field. In the second part of the figure, the amplitude modulations of the oscillatory activity are asymmetric. The dips are weaker than the peaks. The last part of the figure shows the topography of the amplitude asymmetry of the EEG potentials. The peaks and dips are modulated similarly and the amplitude fluctuations of the signal are symmetric, if an Amplitude Fluctuation Asymmetry Index (AFA_{index}), which measures the asymmetry of amplitude fluctuations, is close to 0. Moreover, the dips are weaklier modulated than the peaks and vice versa if an AFA_{index} is positive. Figure 1.2 is adapted from [78].

EEG signals arise from the coordinated activity of $\sim 10^6$ pyramidal cells in the cortex as figure 1.2 shows [23]. These are parallel to their dendrites and perpendicular to the cortical surface. Synchronously activated population of cortical pyramidal cells, that has behaviour like dipole layer, generates the potential field at the population level. For

excitatory (inhibitory) synapses this creates a sink (source) with a negative (positive) extracellular potential.

Magnetoencephalography (MEG) is another technique used to measure magnetic fields in the brain through magnetometers on the surface of scalp. The first MEG signals were measured by David Cohen in 1968 [5, 6, 18]. While MEG has as high temporal resolution (1 ms or better) as EEG, it has a higher spatial resolution than EEG [19, 6]. However, the detection of magnetic fields is difficult as they need to be close to the surface of the brain. The magnetic fields induced are $\sim 10^{-15}$ T in magnitude; therefore they require sensitive magnetic field detectors. The only detectors are Superconducting Quantum Interference Devices (SQUIDs). These detectors were introduced by James Zimmerman in the late 1960s [49].

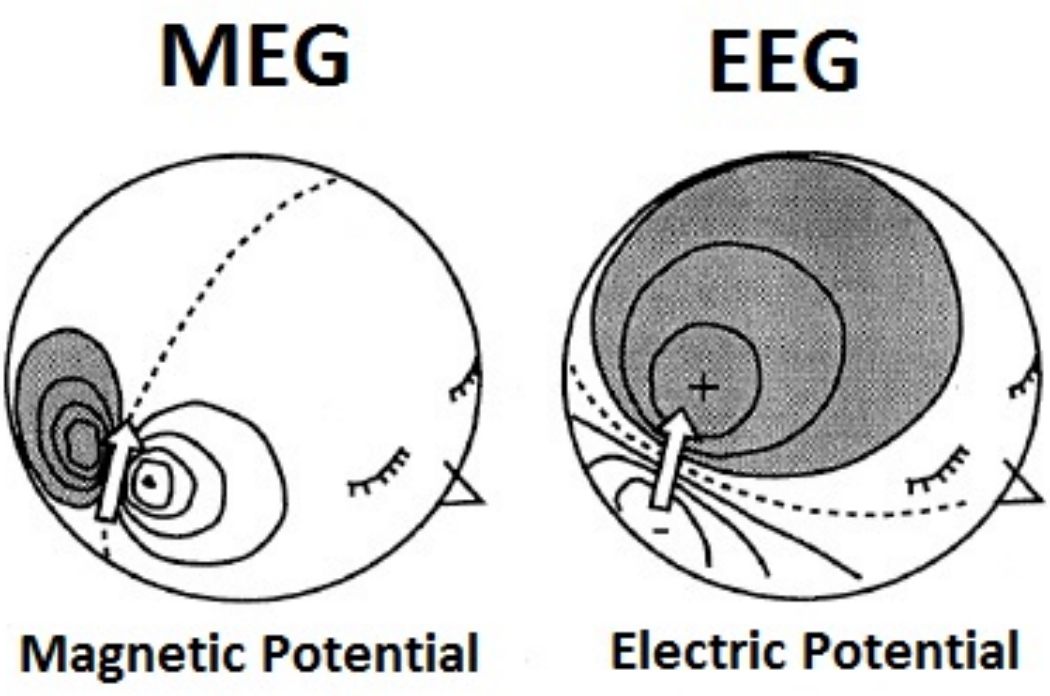

Figure 1.3: EEG is based on the detection of small changes in voltage at the scalp that are caused by electrical currents in neurons in the brain. MEG is based on the detection of small magnetic fields, which are induced by same electrical current in the brain. Figure is taken from [92].

As seen in Figure 1.3, EEG detects small changes in voltage at the scalp that are caused by electrical currents in neurons whereas MEG detects small magnetic fields which are induced by same electrical current in the brain. It is shown in Figure 1.4 that

in EEG systems, electrodes are positioned in different locations of the scalp. Anywhere between 32 and 128 electrodes are used for whole head measurements. In MEG systems, almost 300 radially oriented pick up coils are used. SQUIDs generally keep in a bath of helmet shaped liquid helium and they place on above the head of the subject at a distance of $2-3$ cm. Both techniques measure a topographical map of electric or magnetic field across the surface of the head. This topographic map gives some information about the distribution of electrical current in the head.

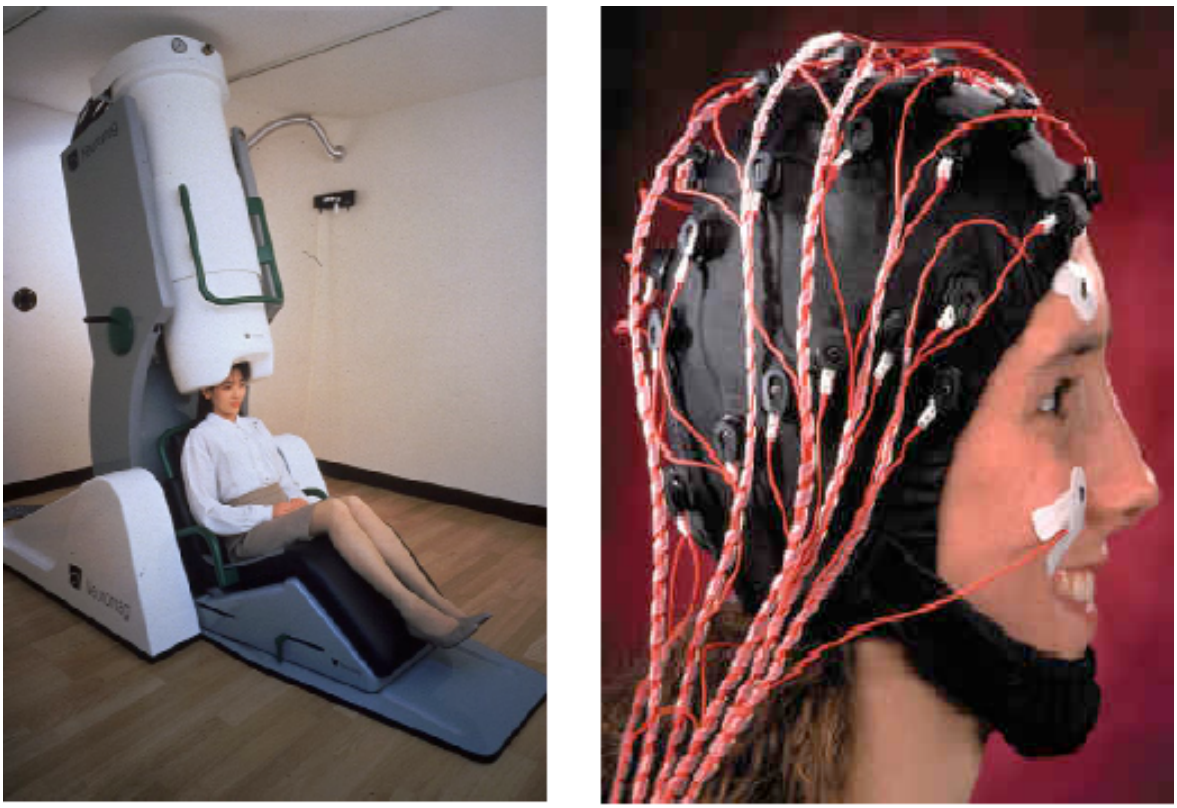

Figure 1.4: To visualise the brain, EEG electrodes are placed on the scalp. On the other hand, MEG sensors are put outside of the head. They are in a helmet shaped tank which contains liquid helium to improve the level of superconductivity. The SQUID is used to detect the magnetic fields [49]. Figure is taken from [92].

EEG is used largely for research and clinical diagnosis. MEG is not extensively used clinically as it is expensive, however it has a important role in the pre−surgical mapping, epilepsy, Parkinson's disease and post traumatic stress syndrome.

1.2.2 MRI, fMRI and BOLD-fMRI

Neuroimaging plays a significant role in determining the structure and the dynamics of brain by the help of various techniques. Magnetic resonance imaging (MRI) allows to view the parts of the brain with the use of a magnetic field and radio waves [15, 6]. This technique is noninvasive and safe to use. Moreover, MRI signals are sensitive to tissue oxygenation. Magnetic susceptibility of blood rises linearly with increasing oxygenation. Therefore, functional changes induced by neural activity in the brain is shown by MRI.

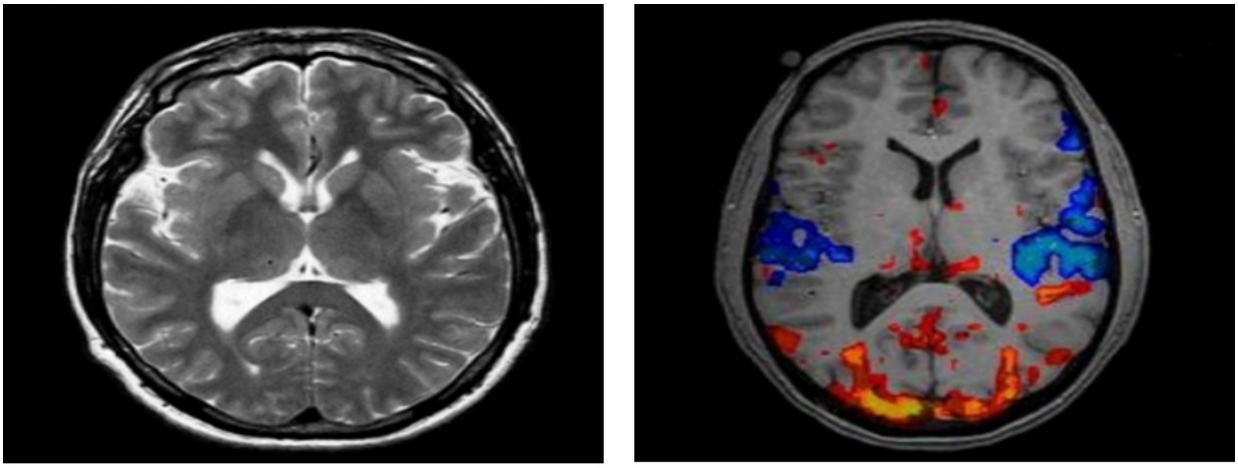

Figure 1.5: Although MRI is used to study brain anatomy, fMRI is used to study brain function [122].

One of the important neuroimaging technique is functional magnetic resonance imaging (fMRI). fMRI is a noninvasive imaging technique used by clinicians and neuroscientists. It represents an indirect measurement of neural activity by tracking metabolism alterations in figure 1.5 [15, 57]. The link between changes in neural activity and cerebral blood flow is called neurovascular coupling. When neural activity increases, active tissues require more energy. Therefore, a higher energy requirement induces an increase in blood flow which affects the alterations in neural activity [28]. Neural responses cause to a rise in oxygenated haemoglobin, but a decrease in deoxygenated haemoglobin. fMRI allows to visualise the function of the brain, showing which parts of the brain have important tasks and how these are affected in diseases such as epilepsy, tumours and Alzemier's [57]. Furthermore, fMRI has a high spatial resolution,

even though its temporal resolution is low [106].

fMRI data via the blood oxygen level dependent (BOLD) signals demonstrate dynamical changes in the oxygenation levels in blood as seen in figure 1.6. The primary form of fMRI uses BOLD. BOLD measures neural activity indirectly [11, 38, 29], since the necessary thing to determine BOLD signal is to make a link to neural activity by interacting the physical haemodynamic operations and models. BOLD-fMRI depends on the relation between neural activity and its corresponding change in cerebral blood flow, cerebral metabolic rates of oxygen and glucose consumption [105]. These cause the changes in deoxyhemoglobin level which affects BOLD signals.

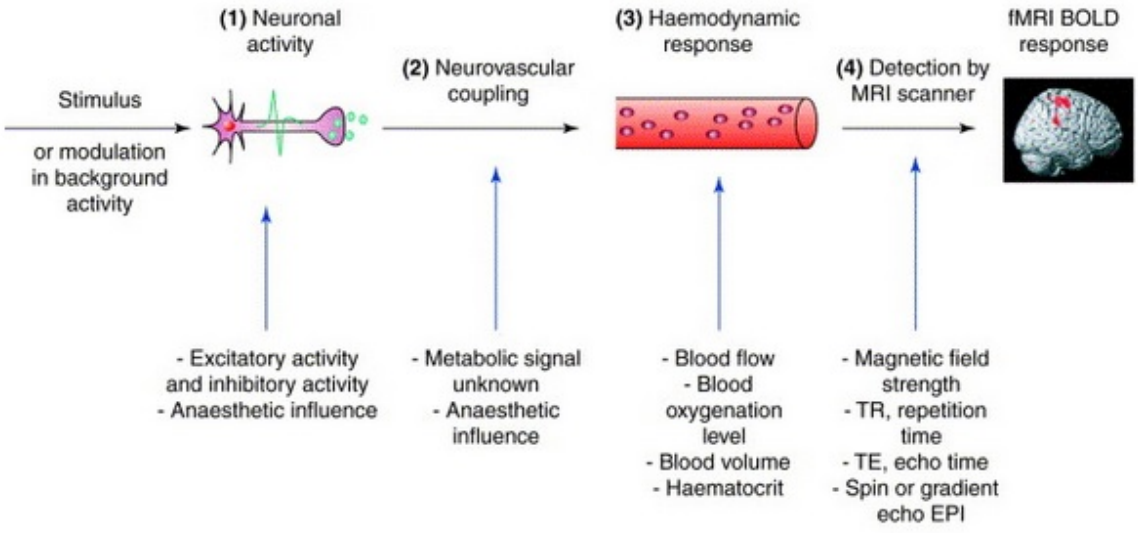

Figure 1.6: The blood oxygen level-dependent signal has several key components. The BOLD signal is dependent on the neuronal response to a stimulus and neural activity which gives rise to the haemodynamic response (known as neurovascular coupling). Other constituents of the BOLD signal include the haemodynamic response itself, and the way in which this response is determined by the MRI scanner [4].

Spatial resolution is used to determine the alteration in signal across different spatial locations whereas temporal resolution is used to identify the rate of changes in signal. Furthermore, as it is seen in figure 1.7, the temporal and spatial resolution of functional neuroimaging techniques are different from each other. Temporal resolutions of MEG and EEG ($< 0.1s$) seem to be higher than fMRI's temporal resolution ($> 1s$) [123]. fMRI has high spatial resolution ($< 5mm$) while EEG and MEG have low spatial resolution,

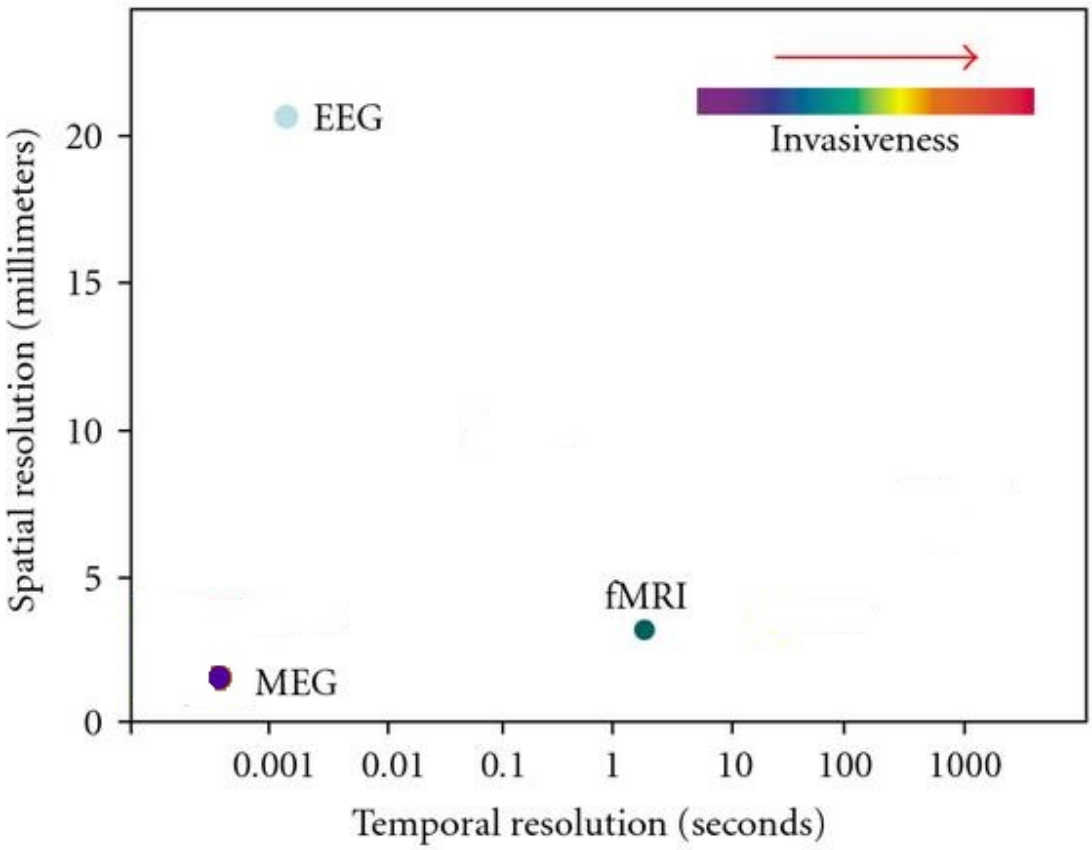

Figure 1.7: The comparison of the spatial and temporal resolution of MEG, EEG and fMRI. Adapted from [123].

however MEG has better spatial resolution than EEG. These techniques are noninvasive and they measure neuronal activity directly.

1.3 Basic Metabolism in the Brain

In section 1.2, popular neuroimaging methods are explained and in this section, we will define basic metabolism in the brain. The cortex does not include only neurons. It has also a great number of supportive cells called glia [62]. They are necessary for controlling synapse function and brain development [41]. Astrocytes are the star-shaped glia cells which help to indicate neural activity and regulate synaptic transmission and plasticity, they also provide physical and metabolic support for neurons [89, 42].

Figure 1.8 shows that neuroglial interaction happens in several steps at the tripar-

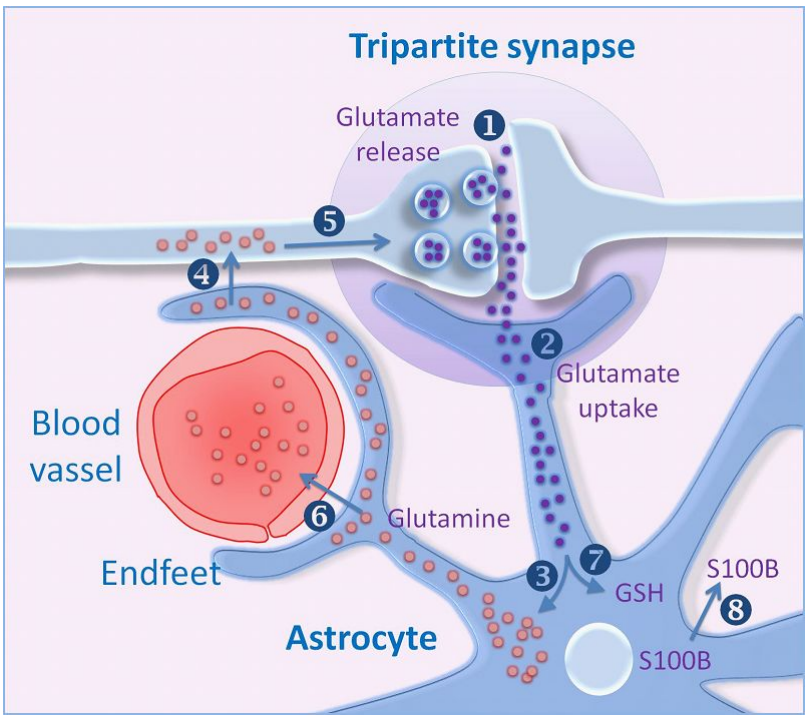

Figure 1.8: Neurotransmitters are released from the synapse into the synaptic cleft. The tripartite synapse has three parts, a presynaptic neuron, a postsynaptic neuron and an astrocyte for synaptic modulation [44].

tite synapses [42]. The close interaction between a presynaptic neuron, a postsynaptic neuron and an astrocytic network, integrating synaptic activity and releasing neuromodulators has been described as a tripartite synapse [3, 89]. At the tripartite synapse astrocytes can not only contact with presynaptic neurons and postsynaptic neurons but also control plasticity and synaptic transmission [3, 80].

1.4 Mathematical Models

Mathematical models in neuroscience aim to study neuronal phenomena by using biophysical models of neurons and networks. For example, the leaky integrate and fire model, which was developed by Lapicque in 1907, is the simplest neuron model [1]. Furthermore, the four-dimensional Hodgkin-Huxley (HH) model (coined by Alan Hodgkin and Andrew Huxley in 1952 [53]) denotes the nonlinear dynamics of a squid axon, and represents how action potentials start and spread [20]. Following this, the cable of dendritic tree was described by Wilfrid Rall in 1962 [93, 20]. Since then, tissue level models which are obtained by using so-called neural mass equations, such as the Wilson-Cowan

[119], Jansen-Rit [60] and Liley [70] models, have been developed [21, 20]. Furthermore, these neural mass models (NMM) are used to understand the macroscopic electrical activity of the brain [105, 106] and the neural population activity of a great number of neurons in a cortical area [26]. Moreover, the metabolic haemodynamic models symbolise the mechanism of neurovascular coupling [35]. They are also more recent and more physiologically realistic.

1.4.1 Mathematical Model of Synapse

When a presynaptic neuron becomes active, it causes a release of neurotransmitters. This leads to an alteration in the membrane conductance of the postsynaptic neuron and activates receptors of the postsynaptic membrane. This opens ion channels in inhibitory and excitatory postsynaptic current (IPSC and EPSC) [41, 62]. Synaptic currents are often modelled using Ohm's law:

$$I_s = g_s s(V_s - V). \tag{1.4.1}$$

In this equation, the voltage of the postsynaptic neuron is represented by V, V_s signifies the membrane reversal potential and the value of maximum conductance, g_s, is constant. The probability of a channel being open is given by s. This probability is related to concentration of neurotransmitter. Moreover, the synapse is excitatory in the case of $V_s > 0$, but is inhibitory if $V_s < 0$. Therefore, if $V_s \gg V$ and $V_s - V \approx V_s$, with V_s absorbed into g_s, then for synaptically interacting neurons this drive is directly proportional to the conductance state of the presynaptic neuron.

A postsynaptic response is described by

$$s(t) = \eta(t - T), \tag{1.4.2}$$

where $t \geq T$. The function $\eta(t)$ gives the shape of a conductance change in reply to the arrival of an action potential, and T is the arrival time of a presynaptic action potential. A typical choice is the difference of exponentials:

$$\eta(t) = \left(\frac{1}{\alpha} - \frac{1}{\beta}\right)^{-1} \left[e^{-\alpha t} - e^{-\beta t}\right] H(t), \tag{1.4.3}$$

where *H(t)* is a Heaviside step function. Another common choice is the alpha function in figure 1.9:

$$\eta(t) = \alpha^2 t e^{-\alpha t} H(t) \tag{1.4.4}$$

obtained in the limit $\alpha \to \beta$.

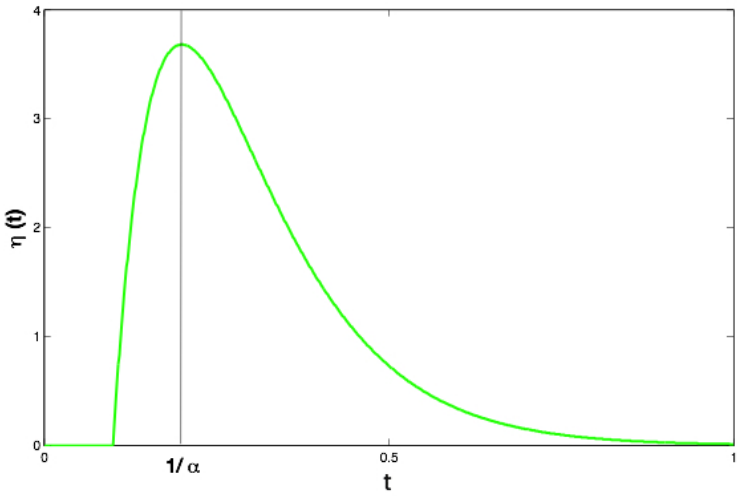

Figure 1.9: A representation of a α-synapse with $\alpha = 10ms^{-1}$, $t = 0.1ms$. The time course of the synaptic current has its peak at $\frac{1}{\alpha}$ ms as is shown here. It is used to model the conductance alteration in the postsynaptic neuron resulting from the neurotransmitter released from the presynaptic neuron.

For more than one spike with firing time labelled by T_m, $m \in Z$, we write

$$s(t) = \sum_m \eta\left(t - T_m\right). \tag{1.4.5}$$

Mathematically, η satisfies the linear differential equation

$$Q\eta = \delta, \tag{1.4.6}$$

where

$$Q = \left(1 + \frac{1}{\alpha}\frac{\mathrm{d}}{\mathrm{d}t}\right)^2.$$

The average membrane potential of a neural population is commonly transformed to an average firing rate by gain functions which are often taken as sigmoidal functions of presynaptic activity [41]. The sigmoidal functions describe the proportion of neurons in a given neuronal population that are active at a given time for a given mean soma membrane potential [25]. They refer to the special case of logistic function bounded differentiable and defined for all real input and positive derivative at each point. The activity of a population is modelled by using its mean firing activity. A common choice for the firing rate function is

$$f(z) = \frac{1}{1 + e^{-\beta(z-\theta)}}, \tag{1.4.7}$$

where $\beta > 0$ is the slope of sigmoid (steepness parameter), and the firing threshold or excitability is described by θ.

1.4.2 A Digression - from Spike to Rate

In many neural population models it is assumed that the interactions are mediated by firing rates rather than action potentials (spikes) per se. To see how this might arise we rewrite (1.4.5) in the equivalent form

$$Qg = \overline{g} \sum_m \delta(t - T_m). \tag{1.4.8}$$

If we perform a short-time average of (1.4.8) over some time-scale Δ, $\langle Qg \rangle_t$ is approximately constant, where

$$\langle x \rangle_t = \frac{1}{\Delta} \int_{t-\Delta}^{t} x(s) \mathrm{d}s, \tag{1.4.9}$$

then we have that $Qg = f$, where f is the instantaneous firing rate (number of spikes per time Δ). For a single neuron (real or synthetic) experiencing a constant drive it is natural to assume that this firing rate is a function of the drive alone. If for the moment

we assume that a neuron spends most of its time close to rest such that $V_s - V \approx V_s$, and absorb a factor V_s into g, then for synaptically interacting neurons this drive is directly proportional to the conductance state of the presynaptic neuron.

Thus for a single population with self-feedback we are led naturally to equations like:

$$Qg = w_0 f(g), \tag{1.4.10}$$

for some strength of coupling w_0. A common choice for the population firing rate function is the sigmoid and it has the same functional form in equation (1.4.7). This functional form is not derived from a biophysical model, rather it is seen as a physiologically consistent choice.

The Jansen-Rit Model

The Jansen-Rit model is one of the most popular NMM which is linked to the studies of Lopes Da Silva *et al.* [24] and Van Rotterdam *et al.* [96]. For the first time it has been described by Jansen and his colleagues [60, 61]. The model has three neural populations: pyramidal neurons, inhibitory interneurons and excitatory interneurons. The Jansen-Rit model describes the neural dynamics in cortical area by a population of excitatory pyramidal cells, receiving inhibitory and excitatory feedback from local interneuron and receiving excitatory inputs from remote areas [105, 26].

Figure 1.10 is modelled as:

$$\begin{aligned} Q_{PP} s_P &= f_P(\alpha E + \beta I), \\ Q_{EE} s_E &= f_E(P), \\ Q_{II} s_I &= f_I(P), \end{aligned} \tag{1.4.11}$$

where

$$Q_{ab} = \left(1 + \frac{1}{\alpha_{ab}} \frac{\mathrm{d}}{\mathrm{d}t}\right)^2,$$

$a, b \in \{E, I, P\}$ and f is given by equation (1.4.7).

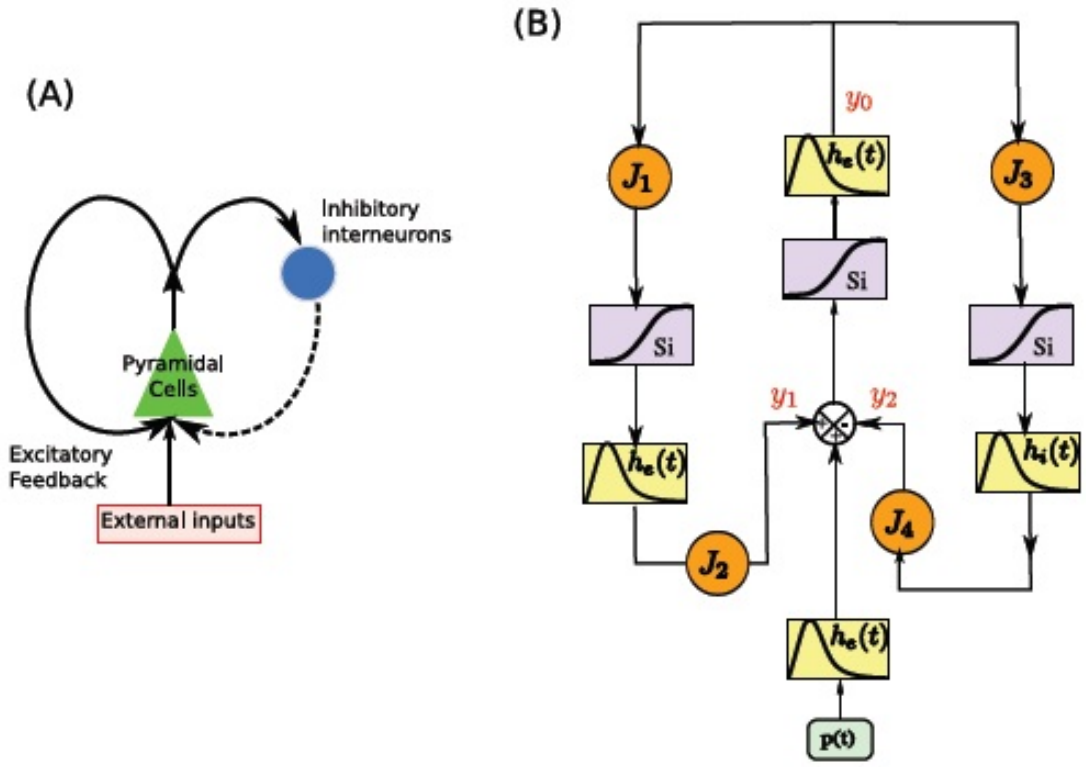

Figure 1.10: Schematic and block diagram of Jansen-Rit model A) There is an interaction between a population of pyramidal cells and two populations of interneurons, one excitatory (left part), one inhibitory (right part) B) The boxes labelled h represent synapses betweeen the neuron populations. S boxes represent the somas of neurons and J symbolises the synaptic connections between populations [117]. This is a nonlinear transformation.

Consequently, as seen in figure 1.10, three second-order differential equations can be rewritten as six first-order equations which is common for the Jansen-Rit model:

$$\dot{y}_{0(t)} = y_3(t), \qquad \dot{y}_{3(t)} = AaS_i(y_1(t) - y_2(t)) - 2ay_3(t) - a^2y_0(t),$$

$$\dot{y}_{1(t)} = y_4(t), \qquad \dot{y}_{4(t)} = Aa[p(t) + J_2S_i(J_1y_0(t))] - 2ay_4(t) - a^2y_1(t), \tag{1.4.12}$$

$$\dot{y}_{2(t)} = y_5(t), \qquad \dot{y}_{5(t)} = BbJ_4S_i(J_3y_0(t)) - 2by_5(t) - b^2y_2(t).$$

E and I is the mean membrane potential in the excitatory and inhibitory populations respectively. J_1, J_2, J_3 and J_4 are the connectivity constants and the number of synapses

between two neuron populations. The constants A, a, B and b are different in the excitatory and inhibitory cases. The units of A and B are millivolts and they indicate the maximal amplitude of the post-synaptic potentials. The average firing rate is represented by $p(t)$. On the other hand, the units of a and b are s^{-1} and they state the characteristic delays of the synaptic transmission [61].

Three main variables in the model are $y_0 = s_P, y_1 = s_E, y_2 = s_I$ which are the outputs of the three postsynaptic boxes [117]. The output firing rate of the pyramidal population is shown by y_0, the excitatory incoming firing rate to the pyramidal population is performed with y_1, and the inhibitory firing rate incoming to the pyramidal population is shown by y_2 [117]. The outputs of the postsynaptic boxes, their derivatives are determined by y_3, y_4 and y_5 respectively. Therefore, excitatory (feedback loop) and inhibitory (interneuron) synapses make a connection between the neural populations. The Jansen-Rit model includes evoked potentials in two connected cortical units [46].

Liley Model

Unlike the Jansen-Rit model, the Liley model [71] has a representation of reversal potentials known to be very important in generating EEG. The mean soma membrane potentials of an interacting excitatory and inhibitory populations describes the cortical activity in this mesoscropic EEG model. The Liley model is used to model human EEG alpha rhythm. There are ten coupled ODEs. Inside a cortical macrocolumn, they show the point of connection between excitatory and inhibitory neural populations. This interaction covers all the potential mixture of feed-forward and feed-back synaptic connections [25].

Referring to the model of synapse, the Liley equations can be written:

$$\begin{aligned}
\tau_E \dot{E} &= E_R - E - W_{EE} g EE(h_E - E) + W_{EI} g_{EI}(h_I - E), \\
\tau_I \dot{I} &= I_R - I - W_{II} g_{II}(h_I - I) + W_{IE} g_{IE}(h_E - I), \\
\dot{x}_{EE} &= a_{EE}(-x_{EE} + f_E + P_{EE}), \qquad \dot{g}_{EE} = a_{EE}(-g_{EE} + x_{EE}), \\
\dot{x}_{II} &= \alpha(-x_{II} + f_I + P_{II}), \qquad \dot{g}_{II} = \alpha(-g_{II} + x_{II}),
\end{aligned} \tag{1.4.13}$$

$$\dot{x}_{IE} = a_{IE}(-x_{IE} + f_E + P_{IE}), \qquad \dot{g}_{IE} = a_{IE}(-g_{IE} + x_{IE}),$$

$$\dot{x}_{EI} = \alpha(-x_{EI} + f_I + P_{EI}), \qquad \dot{g}_{EI} = \alpha(-g_{EI} + x_{EI})$$

where $f_E = 1/[1 + e^{(-\beta_E(E-\theta_E))}]$ and $f_I = 1/[1 + e^{(-\beta_I(I-\theta_I))}]$.

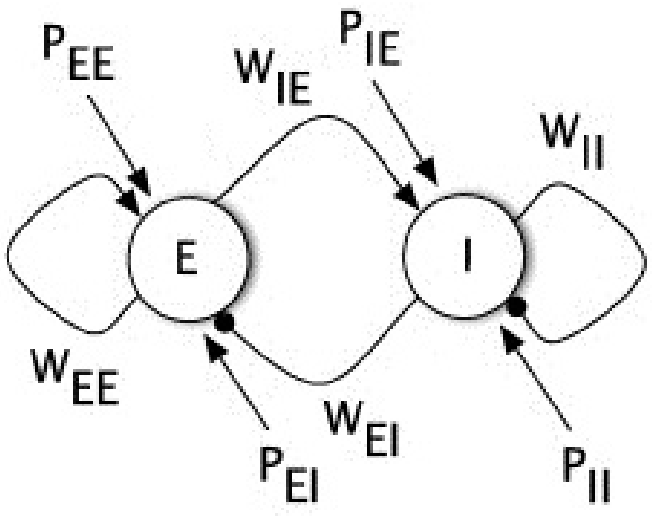

Figure 1.11: The relationship between excitatory (E) and inhibitory (I) neuron populations. W_{ab} is the weight and P_{ab} is constant where $a, b \in \{E, I\}$ [22].

The variables, E and I symbolise the mean soma membrane potential for excitatory and inhibitory populations, respectively. Furthermore, the constants E_R and I_R represent leak reversal potential, and the reversal potentials for the ionic species mediating synaptic activity is shown by the constants h_E and h_I in figure 1.11. Furthermore, τ_E and τ_I are the membrane time constants and τ_I is typically less than τ_E. P_{EE}, P_{EI} are subcortical spike input to excitatory population, and P_{II}, P_{IE} are subcortical spike input to inhibitory population. They are all constant. The weights W_{ab} are the product of a static factor and a dynamic conductance where $a, b \in \{E, I\}$.

The model was simulated in Matlab and the results are shown in figure 1.12, for $P_{EE} = 0.006216$. Observe that although the voltages for inhibitory and excitatory populations are different at the beginning of spikes, they have almost the same value at the end of the spike. Also, the frequencies of oscillations are identical for these two neuron populations.

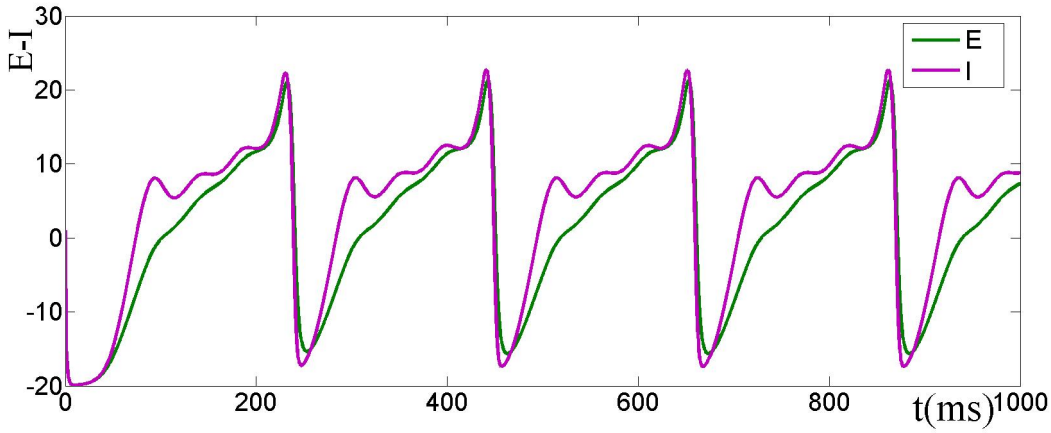

Figure 1.12: An example of an oscillation in the Liley model. Revised parameters from [25] are $P_{EE} = 0.006216ms^{-1}$, $P_{IE} = 0.005763ms^{-1}$, $P_{EI} = P_{II} = 0$, $\alpha_{EE} = \alpha_{IE} = 1.01ms^{-1}$, $\alpha_{II} = \alpha_{EI} = 0.142ms^{-1}$, $W_{EE} = W_{IE} = 43.31$, $W_{II} = W_{EI} = 925.80$, $\beta_E = 0.3mV^{-1}$, $\beta_I = 0.27mV^{-1}$, $\theta_E = 21mV$, $\theta_I = 29mV$, $h_E = 115mV$, $h_I = -20mV$ [22].

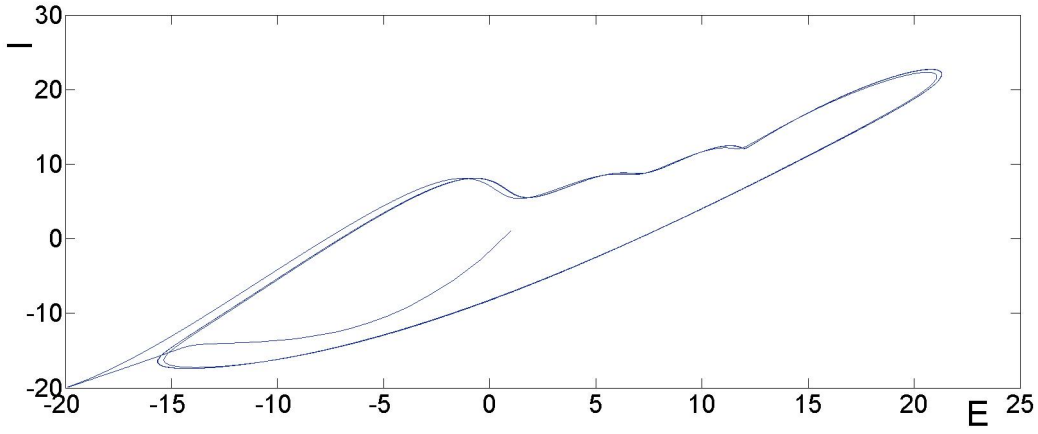

Figure 1.13: The trajectory of $E - I$ phase plane for Liley model with the parameter $P_{EE} = 0.006216$.

Figure 1.13 demonstrates the phase plane in $E - I$ space. The trajectories converge to the limit cycle.

The model switches between different behaviours as shown in the bifurcation diagram 1.14. The bifurcation diagram demonstrates the coexistence of a large and small amplitude periodic orbit with time series in figure 1.12. The large amplitude orbit, which has $\sim$5 Hz rhythm, fits a form of epileptic dynamics. On the other hand, the small amplitude orbit, which has $\sim$10 Hz rhythm, corresponds to the alpha rhythm of the EEG spectrum. It can be seen from the bifurcation diagram that there is a periodic coupling

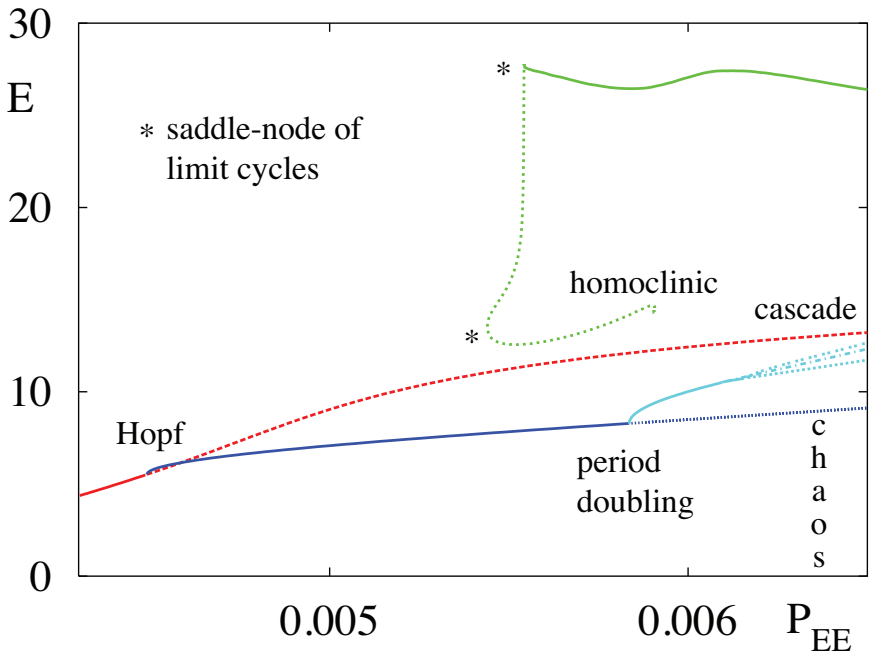

Figure 1.14: Bifurcation diagram for Liley model which shows the absolute maximum of E in terms of P_{EE} for steady state shown red line, small amplitude periodic orbits shown blue line, and large amplitude periodic orbits shown green line. Stable branches are represented by solid lines, unstable branches are represented by dashed lines. After the periodic doubling cascade, chaotic solutions are found. Revised parameters from [25] are $P_{IE} = 0.005763ms^{-1}$, $P_{EI} = P_{II} = 0$, $\alpha_{EE} = \alpha_{IE} = 1.01ms^{-1}$, $\alpha_{II} = \alpha_{EI} = 0.142ms^{-1}$, $W_{EE} = W_{IE} = 43.31$, $W_{II} = W_{EI} = 925.80$, $\beta_E = 0.3mV^{-1}$, $\beta_I = 0.27mV^{-1}$, $\theta_E = 21mV$, $\theta_I = 29mV$, $h_E = 115mV$, $h_I = -20mV$ [15, 22].

cascade. Consequently, the model has chaotic behaviour.

1.4.3 Neural Mass and Metabolic Haemodynamic Models

Metabolic haemodynamic models aim to represent the mechanisms of neurovascular coupling in different studies [10, 105]. The dynamics of cerebral blood volume and deoxyhemoglobin level during the neural activity and how it affects the formation of the BOLD response in fMRI imaging were determined in the Balloon model by Buxton and his colleagues [11]. In other words, the Balloon model, which is a metabolic model, describes the relationship between the current energetic model, blood volume and deoxyhemoglobin content [105]. The input of the system is blood flow and the output is the BOLD signal, it has two state variables: volume and deoxyhaemoglobin [11].

The Liley model was coupled with a metabolic hemodynamic model (MHM) that was introduced in [105] and Chapter 3. Voges *et al.* chose the Jansen-Rit model instead of the Liley model in their recent study[118]. One of the main limitation in Jansen-Rit model is that it is unable to generate certain types of cortical activities such as epileptic activity. Moreover, there is no self interaction for inhibitory and excitatory neuron population, however the Liley model has self interaction for both of them through the introduction of the W_{EE}, W_{EI}, W_{II}, W_{IE} terms. The graphical representation coupling of the MHM with the NMM is shown in figure 1.15.

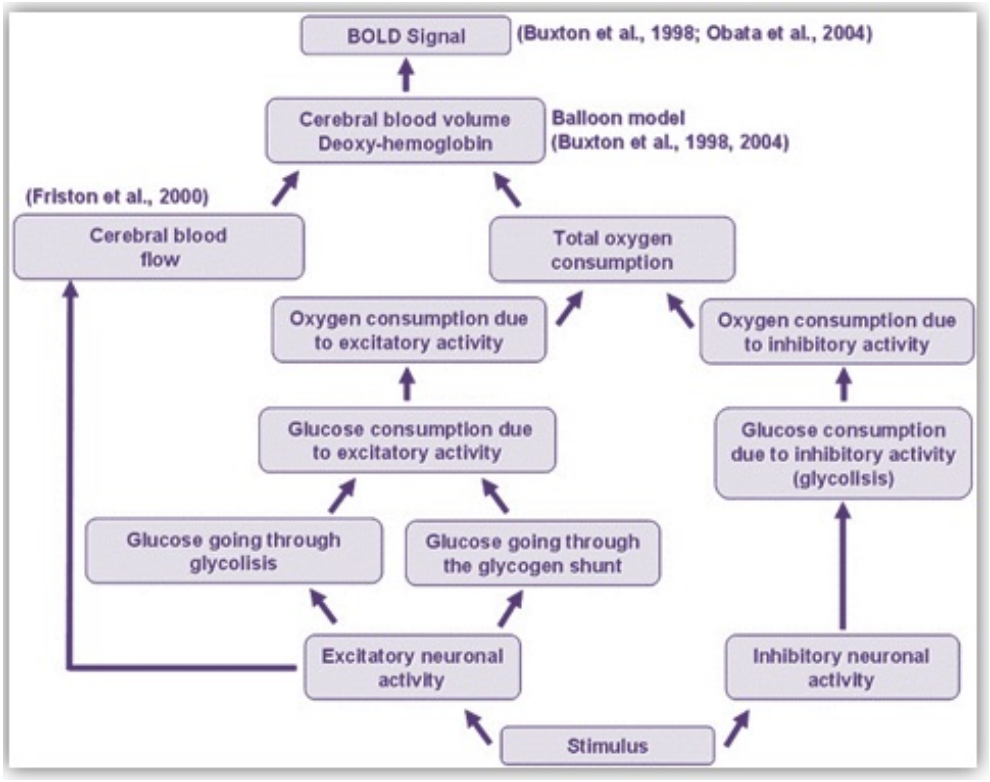

Figure 1.15: Diagram of the model coupled MHM within NMM. In addition to MHM, it shows the relation between the changes in excitation and inhibition to variations in oxygen and glucose consumption [105].

The diagram 1.15 indicates the parallel arrangement of cerebral blood flow and metabolic processes. It can be clearly seen from the diagram that glucose consumption, oxygen consumption and cerebral blood volume and deoxyhemoglobin level depend on the inhibitory neuronal activity, only the cerebral blood flow depends on excitatory neuronal activity. The Liley model is used as input for MHM in order to couple these two model. Values of parameters are taken from [105] and [25]. We examined the output

of the new model as BOLD signal.

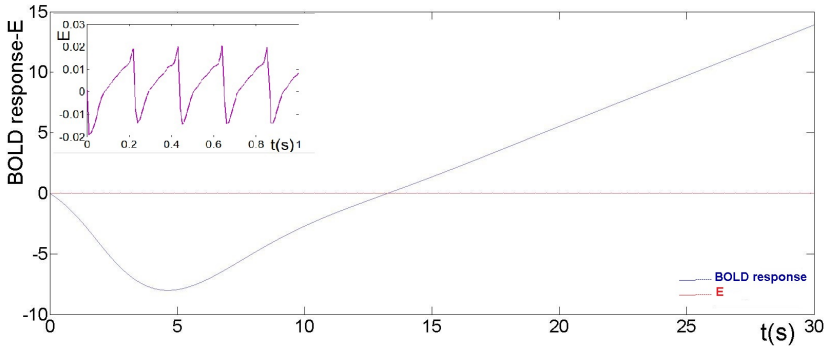

Figure 1.16: A BOLD response as a function of time from the model in diagram 1.15.

Figure 1.16 is a representation of the BOLD response. It does not reflect the underlining oscillations.

1.5 Discussion and Conclusion

This chapter contained a literature review covering some aspects of the background material featured in the thesis. The project analyses mathematical models that combine descriptions of neuronal activity with details of nutrient supply via the blood, and metabolism in the cells of the brain. One question of interest is the relationship between epileptic discharges as measured by EEG and the haemodynamic response as measured by fMRI. To understand this link, biophysical models are useful. The purpose of our research is to make a new prediction about spatiotemporal dynamics from a biophysical model which is coupled to blood flow, volume, pressure and the level of oxygenation, and control empirically these with a high resolution fMRI of the cortex [2].

fMRI data is characterised and haemodynamic waves are observed from these data which provide the prediction of wave interval, damping rates, and speed. A neural mass model (capable of supporting epileptic discharges) is coupled to a metabolic-haemodynamic model and analysed the resulting BOLD signal numerically. The neural mass model worked with is that of the Liley model (which models excitatory and inhibitory activity in a cortical macro-column), whilst the neurovascular model is adapted from the study of Voges and his colleagues [118] (which tracks changes in glucose and

oxygen concentration).

The focus is on the mathematical analysis of the model dynamics in the absence of spatial effects, together with waves in 2+1 dimensional models of neural media. There is further scope for applications to fMRI modelling and the development of virtual brain tissue models which utilises realistic anatomical and physiological information available from databases such as the Human Connectome.

Chapter 2

Functional and Structural Connectivity

This chapter is concerned with the relationship between functional and structural brain connectivity via computational models. Computational models use mathematical language to understand the complex behaviour of a real system. Generally analysis of a model is easier than understanding the theory of a system, therefore simulation of a model has more advantages than solving a real problem. A set of popular models is neural mass models (NMM). These are used to understand the macroscopic electrical activity of the brain [105, 106] and studies the neural population activity of a large number of neurons in a cortical area [26]. Several popular NMMs are Wilson-Cowan (1972) [119], Jansen & Rit (1995) [60], and Liley (1999) [71]. These were discussed in Chapter 1.

This chapter begins by giving basic definitions such as brain connectivity, highlighting functional and structural connectivity. The chosen mathematical model, a Wilson-Cowan model is described in section 2.3.1. We proceed by conducting bifurcation analysis, defining the conditions for both Hopf and Saddle nodes. Then, section 2.3.2 explains how to define structural connectivity (SC) which is produced by the realistic scenarios from the CoComac database. CoComac is a systematic record of the known wiring of the primate macaque brain, and measures functional connectivity (FC) with statistical dependence like correlation and mean phase coherence. The correlation between SC and FC is shown for the various parameters of the model. Moreover, communication between brain areas is reflected in patterns of synchronisation and desynchronisation of neuronal activity. In this case, synchrony allows us to define the similarities between FC and SC. Finally, the stability of synchronous solution is determined by the help of the

phase interaction function in section 2.4.

2.1 Brain Connectivity

Brain connectivity is an important concept in modern cognitive neuroscience, it is a very controversial idea. By brain connectivity, we mean the patterns of connections in the brain. It includes different types, such as: anatomical or structural connectivity (the pattern of anatomical links), functional connectivity (the pattern of statistical dependencies) and effective connectivity (the pattern of causal interactions). These occur between specific units in a nervous system [37, 55]. By units we typically mean neural populations or brain regions. By connectivity we mean the structural connections such as synapses or fiber pathways, or statistical or causal relation which are measured by cross-correlations, coherence or information flow. Furthermore, brain connectivity plays a crucial role in determining how neurons and the neuronal systems process information [109].

2.1.1 Functional Connectivity

Functional connectivity refers to the patterns of statistical dependencies as a result of the temporal synchronisation of neural activity in spatially remote areas of the brain in order to achieve a complex cognitive task or perceptual process. In the other words, FC of the observed data defines the undirected statistical dependencies of inter-regional neural interaction [86]. This is significant for the distributed processes in brain function [36, 39]. FC relies on statistical measurements taken during a particular task to get reliable information about the large-scale brain networks. It can also be assessed using brain activity data obtained during a relaxed resting condition which poses minimal demands on experimental preparation [102, 104].

Functional connectivity is the most challenging of the three types of brain connectivity, especially considering neural interaction and analysing neural imaging data [34]. In neuroimaging, the effects of stimulus-evoked responses are displaced by the more general problem of common inputs from other brain regions that are shown as functional

connectivity [36].

A range of statistical techniques such as correlation, coherence, and covariance can be used in practice for the measurement of FC [69]. Correlation represents the statistical relationship between two random variables or two sets of data [107]. Additionally, coherence measures the phase stability between two different time series [115]. Moreover, how much two random variables change together is measured by covariance [107]. If the smaller values of one variable correspond to the smaller values of the other variable, the variables lean to show similar dynamic, so the value of covariance becomes positive. The same also holds for the greater values, however for the opposite case, the value of covariance becomes negative. The sign of covariance symbolises the tendency in a linear relationship between the variables. Therefore, determining the relationship quantitatively is equivalent to a direct prediction of the existence of a relationship between various brain regions only in the case of a high significance of correlation and coherence [34] .

These statistical techniques can be written mathematically: X and Y are real-valued random variables for the experiment with means $E(X)$, $E(Y)$ and variances $\mathrm{var}(X)$, $\mathrm{var}(Y)$ respectively. The covariance of (X, Y) is formulated by

$$\mathrm{cov}(X, Y) = E\left([X - E(X)][Y - E(Y)]\right) \tag{2.1.1}$$

and assuming the variances are positive, the correlation of (X,Y) is formulated by

$$\mathrm{cor}(X, Y) = \frac{\mathrm{cov}(X, Y)}{\mathrm{sd}(X)\mathrm{sd}(Y)} \tag{2.1.2}$$

where *sd* refers standard deviation which measures the spread of the numbers in a set of data from its mean.

In fact, these statistical techniques are suitable for the specific measurement modality including high spatial resolution techniques such as functional magnetic resonance imaging. fMRI measures neural activity using the metabolic changes in blood flow [2]. It describes the brain anatomy. Therefore, it allows to indicate which parts of the brain

have important tasks and can show the effects of diseases such as epilepsy, tumours and Alzemier's. High temporal resolution techniques such as electroencehalography, which measures the voltage alterations generated by the neural electrical activity at the surface of scalp [5], and magnetoencephalography, which measures magnetic fields in the brain through magnetometers on the surface of scalp [5], are also used in which more time-resolved, data modality and elaborate methods of synchronisation assessment such as quantifying the phase synchronisation is common compared to high spatial resolution techniques. In addition to this, synchrony based on wavelet [68] and Hilbert transforms [113] to measure of functional connectivity between cortical areas have been published recently.

2.1.2 Structural Connectivity

Structural connectivity, also called anatomical connectivity, refers to the structure of the anatomical connections, or the presence of neural pathways between remote brain regions [109, 21]. SC relies on the description and subsequent evaluation of fiber tracks called white matter which connects neuron pools within the brain. These fiber pathways, composed of the neuronal axons, transmit neural signals across brain areas allowing the link between different brain regions. Structural connectivity was traditionally explored using animal experiments, resulting in a greater scope of information available. In time, this has been changed because of the growth in vivo imaging techniques such as MRI that is used to view parts of the brain with the use of a magnetic field and radio waves [15], and fMRI which indirectly measures neural activity by tracking metabolism changes [15]. These are used to visualise the white matter [97].

2.2 The Link between Functional and Structural Connectivity

Investigations on the relationship between functional and structural connectivity using imaging methods have recently received great attention in the clinical and experimental neuroscience communities. Modern imaging methods allow a noninvasive evaluation of the functional and structural brain connectivity. This can help to identify changes to functional connectivity caused by disease. Furthermore, functional and

structural connectivity are thought to be integrated into different brain areas which allow us to understand the information process of the neurons and neuronal systems.

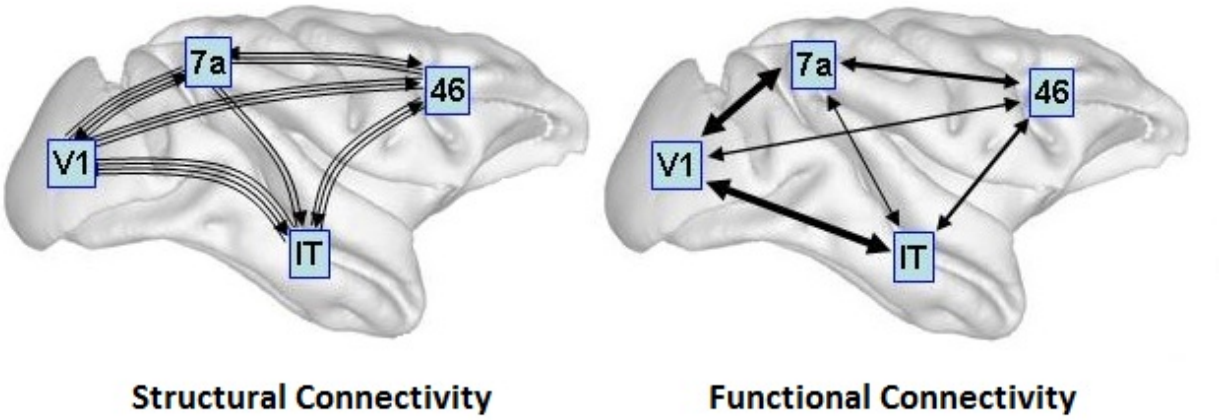

Figure 2.1: The figure which is taken from [108] shows the structure of FC and SC. Brain has two kinds of tissues. Grey matter which has a pinkish grey colour in the living brain and contains the cell bodies, dendrites, and axon terminals of neurons. This is where all the synapses are. White matter is made of axons connecting different parts of grey matter to each other. The arrows represent real white matters. Furthermore, FC is the statistical association, that may be estimated by measuring correlation or covariance, spectral coherence or phase-locking, among the neural activation patterns of anatomically separated brain regions such as $V1$, 46, $7a$ and IT. $V1$ the primary visual cortex is responsible for processing visual information. 46 is the part of the frontal cortex and have a role in attention and working memory. $7a$ is crucial for language, mathematical operations and body image. IT is inferior temporal cortex which plays a significant role in visual object recognition.

In order to build brain connectivity in models, we need to have functional and structural connectivity data. As seen in figure 2.1, for structural connectivity, data is related to white matter and provides estimates of the level of interregional connectivity. For functional connectivity, relevant data is based on interregional interactions in measurement of synchronisation and communication between the brain regions.

The functional connectivity analysis is an effective data processing method in the detection of consistently synchronised networks of brain areas. However, the precise relationship between the functional connectivity and the structural connectivity is still not known in detail. To understand this more, more complicated models can be used.

To summarise, the primary goal of this study is the investigation of the relationship between the functional connectivity and the structural connectivity using neural mass models by expressing the role of mutual synchronisability of brain subunits.

2.3 Mathematical Structure

2.3.1 Model Description and Bifurcation Analysis

A neural mass model is used to explain the interaction between FC and SC in brain network. We choose the Wilson-Cowan (1972) [119] model because of its simplicity. It describes the dynamics of a network of synaptically interacting excitatory and inhibitory neuronal populations. This influential model was proposed by Hugh Wilson and Jack D. Cowan in the early 1970s [119], and it has been popular in the neural network literature. Ever since Wilson-Cowan model allows to use phase plane methods, and numerically indicate the responses of neural populations to stimuli.

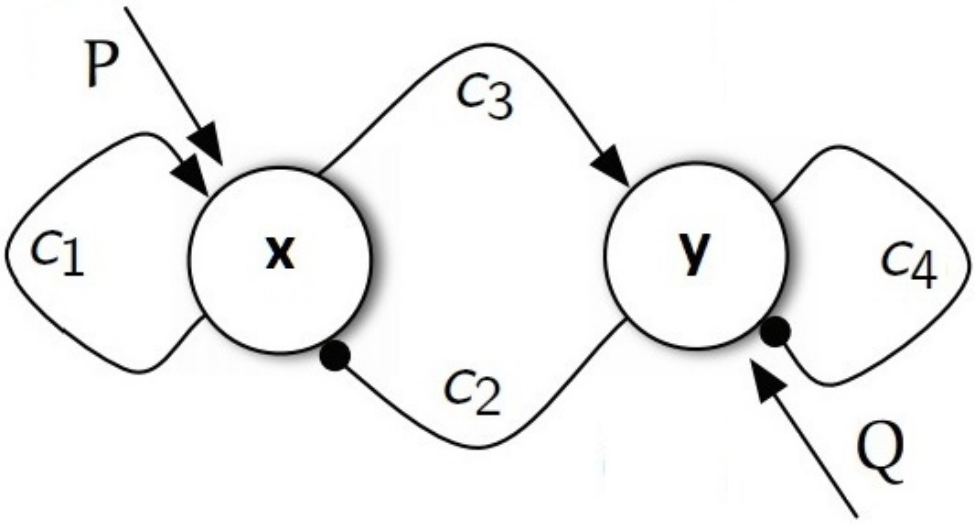

Figure 2.2: The dynamics of interactions between populations of excitatory and inhibitory neurons of Wilson-Cowan model.

The variable x represents the activity of the local excitatory population, whereas the variable y represents the activity of the inhibitory population in figure 2.2. These evolve according to the equations:

$$\begin{aligned} \dot{x_i} &= -x_i + f(c_1 x_i - c_2 y_i + P + \epsilon \sum_j w_{ij} x_j), \\ \dot{y_i} &= -y_i + f(c_3 x_i - c_4 y_i + Q) \end{aligned} \tag{2.3.1}$$

where the function f is the firing rate function. It is chosen as the sigmoidal function:

$$f(x) = \frac{1}{1 + e^{-\beta x}} \quad \text{with} \quad \text{constant} \quad \beta > 0. \tag{2.3.2}$$

In the equation, w_{ij} reflects the connection from neuron i to neuron j [each described by the pair (x_i, y_i)] [52]. It is nonnegative function since it describes the distance between two brain areas. In other words, it represents the structural connectivity pattern in a system of N nodes. This connectivity is determined by b_{ij} matrix which has components, 0 and 1 and we set $w_{ij} = b_{ij} / \sum_k b_{ik}$. The normalised form of input for each node is used. Additionally, the constant $\epsilon \in R$ is the coupling strength. The constants $c_a,\ a \in \{1, 2, 3, 4\}$, are the interaction states within a module. The positive coefficients c_2 and c_3 are synaptic, because they indicate interactions between excitatory and inhibitory neurons. In contrast, c_1 and c_4 are the feedback parameters. They can be negative or positive. P and Q are the external inputs from the brain regions to the excitatory and inhibitory neurons. This is depicted in figure 2.2.

Borisyuk and Kirillov (1992) produced an analysis when $f(x) = \frac{1}{1+e^{-\beta x}}$ [8]. Moreover, Hoppensteadt and Izhikevich (1997) produced a similar analysis [54]. The steady state of this system (x^*, y^*) can be found by setting the temporal dependence equal to zero.

Two populations of $x - y$ network is written as the equations below when $\epsilon = 0$:

$$\begin{aligned} \dot{x} &= -x + f(c_1 x - c_2 y + P), \\ \dot{y} &= -y + f(c_3 x - c_4 y + Q). \end{aligned} \tag{2.3.3}$$

In order to find the equilibrium,

$$\begin{aligned} x^* &= f(c_1 x^* - c_2 y^* + P), \\ y^* &= f(c_3 x^* - c_4 y^* + Q) \end{aligned} \tag{2.3.4}$$

where f is same as the equation (2.3.2) when $\beta = 1$.

The function f is continuous, monotonic increasing and satisfied $f(-\infty) = 0$, and $f(\infty) = 1$, we can therefore find the inverse. When f is chosen to be sigmoidal, the inverse become $f^{-1} = \ln(v/(1-v))$. At the equilibrium point, the solutions of P and Q becomes

$$\begin{aligned} \mathrm{P} &= f^{-1}(x^*) - c_1 x^* + c_2 y^*, \\ \mathrm{Q} &= f^{-1}(y^*) - c_3 x^* + c_4 y^*. \end{aligned} \tag{2.3.5}$$

The Jacobian matrix evaluated at the steady state can be used to investigate stability. In this case, it is given by

$$J = \begin{bmatrix} -1 + c_1 f(c_1 x^* - c_2 y^* + P) & -c_2 f(c_1 x^* - c_2 y^* + P) \\ c_3 f(c_3 x^* - c_4 y^* + Q) & -1 - c_4 f(c_3 x^* - c_4 y^* + Q) \end{bmatrix}. \tag{2.3.6}$$

Using the fact that $\dot{f} = f(1-f)$, we describe the Jacobian matrix in a more convenient form:

$$J = \begin{bmatrix} -1 + c_1 x^*(1-x^*) & -c_2 x^*(1-x^*) \\ c_3 y^*(1-y^*) & -1 - c_4 y^*(1-y^*) \end{bmatrix}. \tag{2.3.7}$$

If either one real eigenvalue crosses or a pair of complex eigenvalues crosses the imaginary axis, stable steady states are usually destabilised. There are two types of bifurcations for this model: Hopf and saddle node bifurcations. Saddle node arises when one real eigenvalue crosses the imaginary axis. Saddle nodes can be shown by examining the intersections of the nullclines. On the other hand, Hopf bifurcation is formed when a pair of two complex eigenvalues crosses the imaginary axis. The conditions of the Andronov-Hopf bifurcation are

$$\text{Tr J} = -1 + c_1 x(1-x) - 1 - c_4 y^*(1-y^*) = 0 \quad \text{and} \quad \det \mathrm{J} > 0. \tag{2.3.8}$$

Since $0 < x < 1$ and $0 < y < 1$, the trace is always negative unless $c_1 > 4$.

When x is described as a curve parameter, y can be eliminated from the equation above. This is given as the black curve plotted on the (P, Q) phase portraits in figure

2.3. The saddle-node bifurcation set (the red curve) is given by $det\ J = 0$. Moreover, the Bogdanov-Takens bifurcation, that is the intersection of the Hopf and saddle node bifurcation curves, is described when $det\ J = 0$ and $Tr\ J = 0$. These curves refer to local bifurcations and are determined by local analysis at equilibria. The bifurcation can be supercritical or subcritical, resulting in a stable or unstable (within a invariant two-dimensional manifold) limit cycle, respectively.

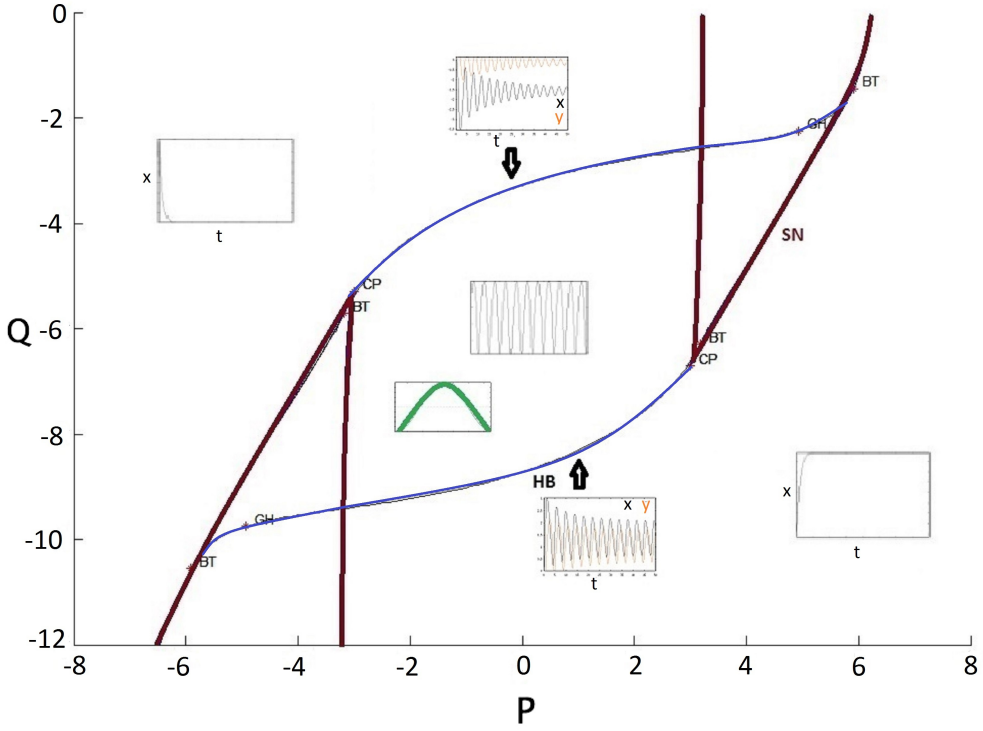

Figure 2.3: The figure shows the bifurcation sets in isolated Wilson-Cowan model with the mixture of excitatory and inhibitory connections in the parameter (P, Q) plane. The parameters are choosen $c_1 = 10$, $c_2 = 10$, $c_3 = 10$, and $c_4 = -2$ [52]. HB symbolizes the Hopf bifurcation and SN is a saddle-node of fixed points. GH denotes the generalized Hopf point, where the first Lyapunov coefficient disappears, and determines local bistability. Moreover, CP represents Cusp point where two branches of saddle node bifurcation curve cross tangentially. BT shows Bogdanov-Takens point at which a Hopf and saddle loop bifurcation meet at a saddle node point where the oscillation disappears and the node changes its stability. $H(\theta)$ is drawn by green lines at point $b((P, Q)) = (-1.5, -6)$ and $H'(0) > 0$. The loss of synchrony is not expected at that point.

According to the Stability theory, if the eigenvalues, λ, of J have negative parts, the equilibrium will be stable and supercritical.

$$\lambda_{\mp} = \frac{1}{2}(\text{Tr J} \mp \sqrt{(\text{Tr J})^2 - 4\text{det J}}). \tag{2.3.9}$$

In order to construct a phase diagram in $x - y$ plane for a fixed weight matrix c_1, c_2, c_3, and c_4, we describe y^* as a function of x^* by imposing a constraint on the eigenvalues λ , then substitute the resulting function into equations (2.3.5). This yields bifurcation curves in the (P, Q) space that are parametrised by x and $0 < x^* < 1$.

On the other hand, it is easy to compute bifurcation diagrams numerically via numerical tools. It can be seen by linear stability analysis of the node dynamics that the oscillations appear via a Hopf bifurcation. Figure 2.3 shows the locus of Hopf bifurcations and saddle-node bifurcations of fixed points in parameter (P, Q) plane. A linear stability analysis of the node dynamics shows that oscillations may arise via Hopf bifurcation. If inhibition is dominant, there is a low level of the activity. Conversely, if excitation is dominant, there will be high level of activity.

The main part of the bifurcation system is shown in the two-parameter diagram as a function of the inputs P and Q. The neural oscillators exhibit periodic activity when the values of parameters P and Q are inside the Hopf area. However, the activity converges to an equilibrium for the rest of the parameters. Additionally, an upper point at $(P, Q) = (1.4, -2.8)$ and a bottom point at $(P, Q) = (0.9, -8.3)$ are chosen along the Hopf border in figure 2.3. While y, which is the orange oscillators, has higher activity than x, which is shown with black, at the upper point, y is less than x at the below point.

2.3.2 Functional and Structural Connectivity

Three types of structural connectivity matrices were examined in figure 2.4 to explain the relationship between FC and SC. The first figure is modular connectivity where the network includes several modules. Although they have internal connectivity, that is connectivity within each node, they do not have any connection between each node. The second one is a part of realistic example which is taken from the 47 areas of macaque cortex with a structural connectivity matrix. These are collected from CoComac database

which has the examples of realistic scenario [64]. The random binary matrix is depicted as the third connectivity matrix in the light of Maslov-Sneppen algorithm. It is a numerical algorithm that construct a randomized network with a given degree of each of the macaque matrix [77].

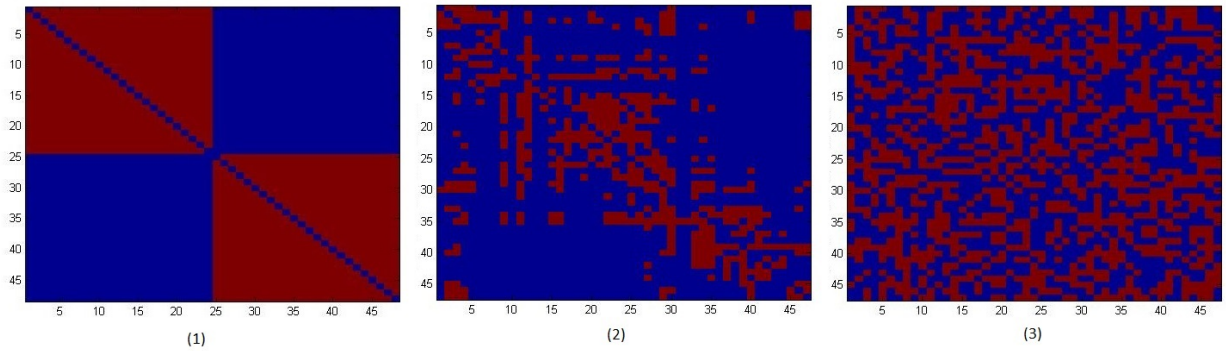

Figure 2.4: SC matrices for modular connectivity (1), brain anatomical connectivity (2) produced by CoComac database, and random connectivity (3). The blue parts denotes no connectivity, conversely the red parts show the anatomical connection between the network nodes.

Structural connectivity forms a sparse and directed graph with binary elements indicating the presence or absence of a connection. If there is a connection, the element of matrix will be 1, otherwise it becomes 0. In figure 2.4, the red parts show the connections, blue colour represents no connection for 47×47 matrix. Data were obtained from CoComac database to build the SC matrix. CoComac gives online access to structural connectivity data on the macaque-monkey brain.

Furthermore, the FC with observed data defines the undirected statistical dependencies of inter regional neural interaction [86]. To calculate functional connectivity, we used a measurement method known as the mean phase coherence which is a statistical measure for phase synchronisation [66, 79].

First, we need to calculate the instantaneous phase of each signal at every time point in order to quantify the mean phase coherence.The phases for each signal are determined by a Hilbert transform, and give by the angle of the complex output. David Hilbert in 1953 defined the Hilbert transform. It is a linear operator which takes a function, $u(t)$,

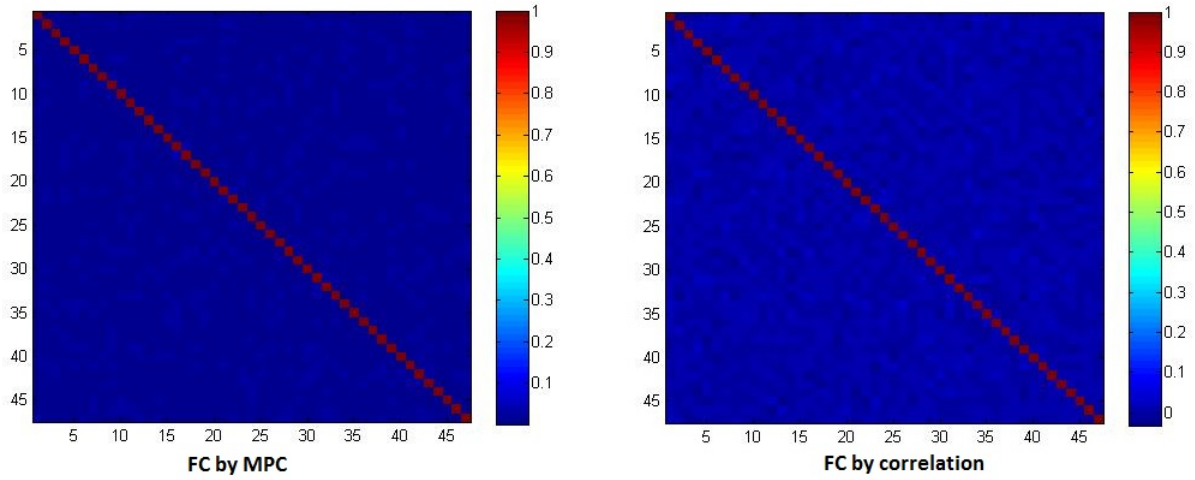

Figure 2.5: FC matrices produced from Wilson-Cowan model by mean phase coherence and correlation in the (P, Q) plane. Here, the values of parameters are $c_1 = c_2 = c_3 = 10$, $c_4 = -2$, $P = -2.5$ and $Q = -8.5$.

and gives a function, $H(u(t))$, with the same domain. The phase coherence of two signals is measured as the temporal stability of phase difference. The mean phase coherence is formulated by Mormann *et al.* [79] :

$$R = |\frac{1}{N}\sum_{j=0}^{N-1} e^{i(\varphi_1(t)-\varphi_2(t))(j\Delta t)}|. \tag{2.3.10}$$

where φ_1 and φ_2 are phases of oscillators and $\frac{1}{\Delta t}$ is the sampling rate of the discrete time series.

On the other hand, functional connectivity is derived by correlation. We used not only Pearson correlation but also Spearman correlation to produce FC, however no differences between these methods were seen. In figure 2.5, FC is calculated by MPC and Pearson correlation, and the both figures are quite similar. Therefore, correlation or MPC does not have a great effect on the calculation of FC.

2.3.3 Simulations of the Model

The simulation of the dynamics of the Wilson-Cowan model is produced in Matlab. We added a small amount of white Gaussian noise with variance $\sigma = 0.01$ to the x variable of each node. This noise allows to detect of stable solutions easily. The Euler-Maruyama [76] method was used to integrate the model with a time step $dt = 0.1$. This method finds the approximate numerical solution of a stochastic differential equation (SDE).

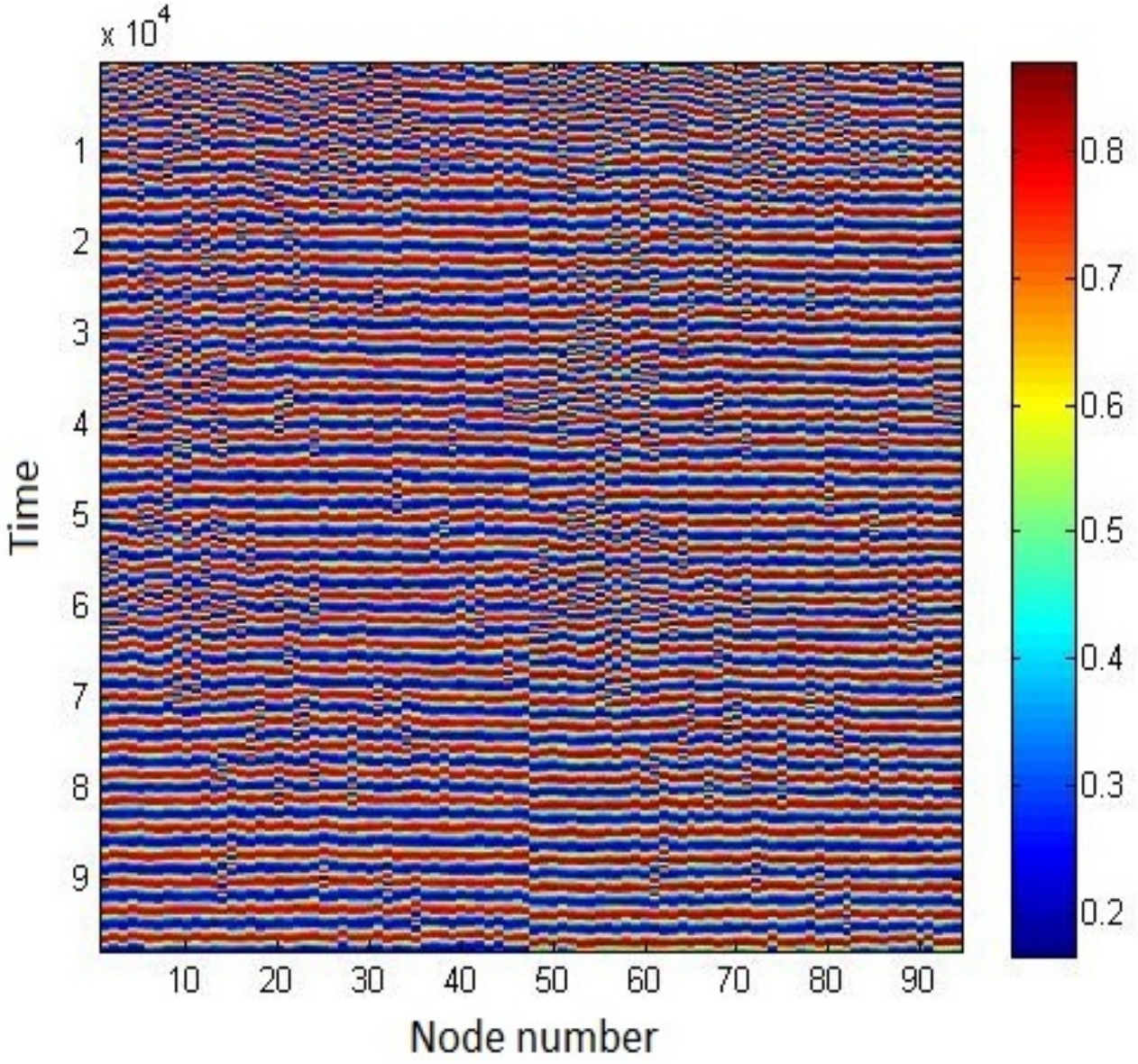

Figure 2.6: A part of time series of the model for a network of 47 population nodes taken from CoComac database, x variable is shown for each node.

The coupling strength was chosen as $\epsilon = 1$. In addition to this, parameter P was altered in the interval $(-6, 6)$ and parameter Q was varied in $(-12, 0)$ with the increments of 0.25.

An example of the system simulation is shown in figure 2.6. The simulation of the model was continued for $T = 10000$ for each parameter setting. The initial values of x and y were chosen in the interval $(0, 1)$ randomly. The first 1000 steps of the functional connectivity analysis were ignored due to initial transients. It can be seen from the data in the figure 2.6 that neural signal synchrony is measured as the synchrony between two or sometimes more continuous time series of brain activity which yield low values for independent time series and high values for correlated time series [65].

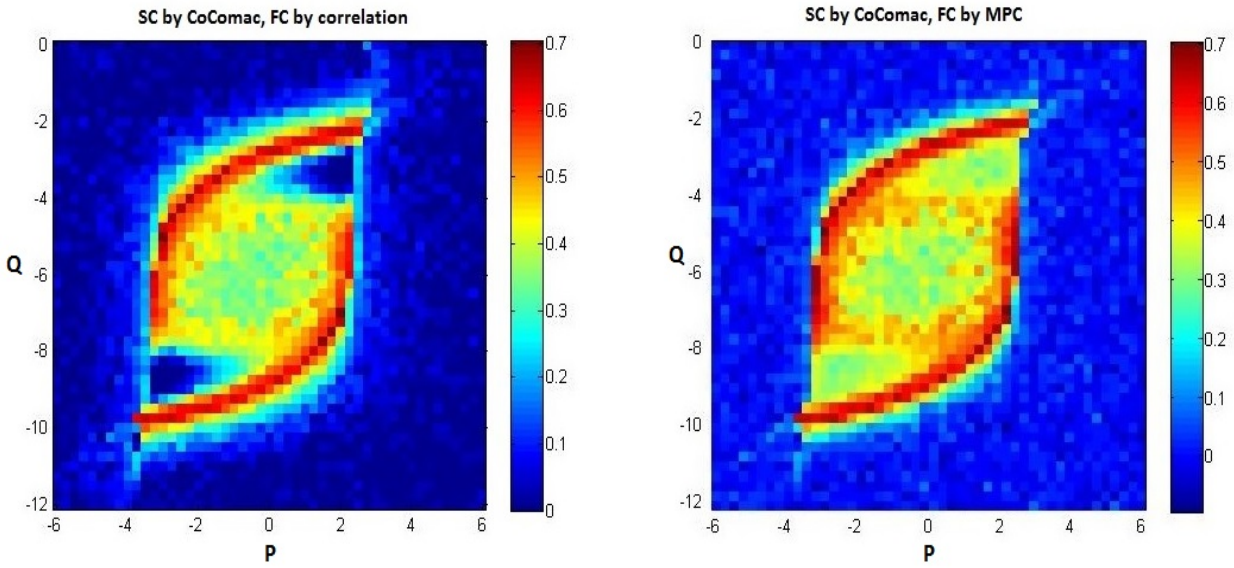

Figure 2.7: The aggrement between FC and SC. Although in both figures, SC is taken from CoComac databes, in left figure FC is measured by correlation, and in right figure by mean phase coherence. To measure the similarity, the Pearson correlation is used.

The interaction of FC and SC is shown in (P, Q) parameter space for the structural connectivity which is taken from the CoComac database. To measure FC, we used correlation and mean phase coherence. The similarities between FC and SC are measured by Pearson correlation in figure 2.7 and Spearman correlation in figure 2.8. While Pearson correlation evaluates the linear relationship between two sets of data, Spearman corre-

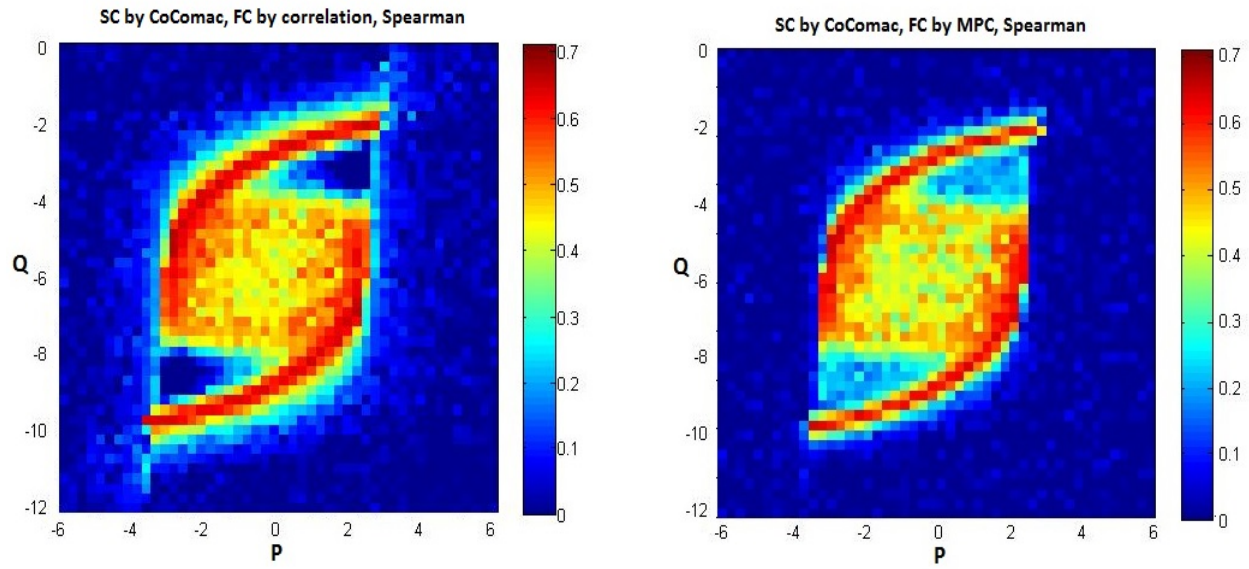

Figure 2.8: The aggrement between FC and SC. Although in both figures, SC is taken from CoComac databes, in left figure FC is measured by correlation, and in right figure by mean phase coherence. To measure the similarity, the Spearman correlation is used.

lation evaluates the monotonic relationship between two sets of data.

In figures 2.7 and 2.8, the colour bars refer the level of synchrony. The red colour indicate greater synchrony, while blue colour indicate less synchrony between FC and SC. FC and SC is more similar along the border of Hopf bifurcation, which is the red border of the eye-shaped figure, rather than other regions of the diagram. Thus, there is no significant difference between Pearson and Spearman correlation, so either the Pearson method or the Spearman method can be used.

2.3.4 Transformation of the Model

The equations (2.3.1) can be written in matrix form:

$$\dot{X} = -X + f(W_c X + R) \tag{2.3.11}$$

where $X = (x_1, \ldots, x_M, y_1, \ldots, y_M)$, $R = (P, \ldots, P, Q, \ldots, Q)$.

Moreover, W_ϵ is defined

$$W_\epsilon = \begin{bmatrix} c_1 I_M + \epsilon w & -c_2 I_M \\ c_3 I_M & -c_4 I_M \end{bmatrix} \tag{2.3.12}$$

where W includes w_{ij} components and I_M is the identity matrix with M dimension. When the linear transformation is used, we gain a suitable form of the model in order to apply the phase reduction method (see later).

$$\dot{Y} = -Y + R + W_0 f(Y) + \epsilon \begin{bmatrix} W & 0 \\ 0 & 0 \end{bmatrix}. \tag{2.3.13}$$

2.3.5 Phase Oscillation Reduction

Standard phase reduction techniques may be used on the model with the equations (2.3.1)

$$\begin{aligned} \dot{x}_i &= -x_i + P + c_1 f(x_i) - c_2 f(y_i) + \epsilon \sum_j w_{ij} f(x_j), \\ \dot{y}_i &= -y_i + Q + c_3 f(x_i) - c_4 f(y_i). \end{aligned} \tag{2.3.14}$$

We choose $\epsilon = 0$ and check for oscillatory solutions with a common trajectory $(x(t + \theta_i T), y(t + \theta_i T))$ and phase shifts $\theta_i \in [0, 1)$. This gives

$$\begin{aligned} \dot{x} &= -x + P + c_1 f(x) - c_2 f(y), \\ \dot{y} &= -y + Q + c_3 f(x) - c_4 f(y). \end{aligned} \tag{2.3.15}$$

The theory of weakly coupled oscillators $(\epsilon \to 0)$ is applied to define the network dynamics with the set of phase variables for $i = 1, \ldots, M$ [54, 59]. The theory of weakly

coupled oscillators is a standard tool of dynamical systems theory. The advantage of the theory of weakly coupled is to reduce the dynamics of each neuronal oscillator in a network to single phase equation which describes the rate of change of its relative phase θ.

2.4 Isochrons

The equation represents a system of the form

$$\frac{\mathrm{d}}{\mathrm{d}t}X = f(x), \quad X \in \mathbb{R}^n, \tag{2.4.1}$$

such that there is a periodic orbit in the system

$$\Gamma = \{u(t) \ : \ t \in \mathbb{R}\},$$

with minimal period $T > 0$ (such that $u(t) = u(t+T)$ for all $t \in \mathbb{R}$, however $u(t) \neq u(s)$ for $0 < s < T$). The asymptotic phase of a point X_0 in the basin of attraction of the limit cycle Γ of period T is the value of $\theta(X_0)$ such that

$$\lim_{t\to\infty} |X(t) - u(t + \theta(X_0))| = 0$$

where $X(t)$ is a trajectory starting at X_0. Thus if $u(t)$ and $X(t)$ are trajectories on and off the limit cycle respectively, they have the same asymptotic phase if the distance between $u(t)$ and $X(t)$ vanishes as $t \to \infty$. An isochron is the locus of all points with the same asymptotic phase. Hence an isochron extends the knowledge of phase off the cycle within its basin of attraction. Furthermore, isochrons can be explained as the leaves of the stable manifold of a hyperbolic limit cycle. They determine the dynamics in the non-existence of perturbations [47].

There are few examples where the isochrons can be computed in closed form. The examples can be found in [121] for plane-polar models where the radial variable decouples from the angular one. Computing the isochron foliation of the basin of attraction of a limit cycle is a considerable challenge as it needs notion of the limit cycle. For this reason, it can be computed only in particular cases or numerically.

2.5 Phase Response Curves

Isochrons help to understand the phase response curves. The phase shifts in response to stimuli delivered at altered times on its cycle period are measured as the phase response curve (PRC) [121]. PRC illustrates the phase shift of the oscillation induced by a perturbation at each phase of the oscillation [83, 14, 103]. The PRC was first introduced by Hasting and Sweeney in 1958 to explain resetting the circadian rhythms [50]. After that study, this has been implemented to other oscillatory systems. PRC is used to predict the behaviour of the oscillator when any small external stimuli or signals from other oscillations are applied.

The PRC is significant in neuroscience. They are crucial in understanding collective dynamical characteristics such as coherent oscillations, travelling waves, and pattern structure. Phase reduced models are used to make simpler the complex models in neuroscience and the interactions induced to neural synchrony [31, 58, 83]. PRCs are also useful for understanding synchronisation of weakly coupled oscillators and for understanding the real biological oscillators.

PRC is measured experimentally or assessed theoretically and used to obtain a set of differential equations for the phases of each neuron in the network [100]. PRCs can be obtained analytically by performing the phase reduction method to the models. They are implemented in a popular package XPPAUT or MatCont [99].

Our model is described by the equations below.

$$\frac{\mathrm{d}}{\mathrm{dt}}\begin{bmatrix} x \\ y \end{bmatrix} = \begin{bmatrix} -x + P + c_1 f(x) - c_2 f(y) \\ -y + Q + c_3 f(x) - c_4 f(y) \end{bmatrix} + \begin{bmatrix} \epsilon w f(x) \\ 0 \end{bmatrix} \tag{2.5.1}$$

The orbit and phase response curve of model for the given parameters are shown in figure 2.9.

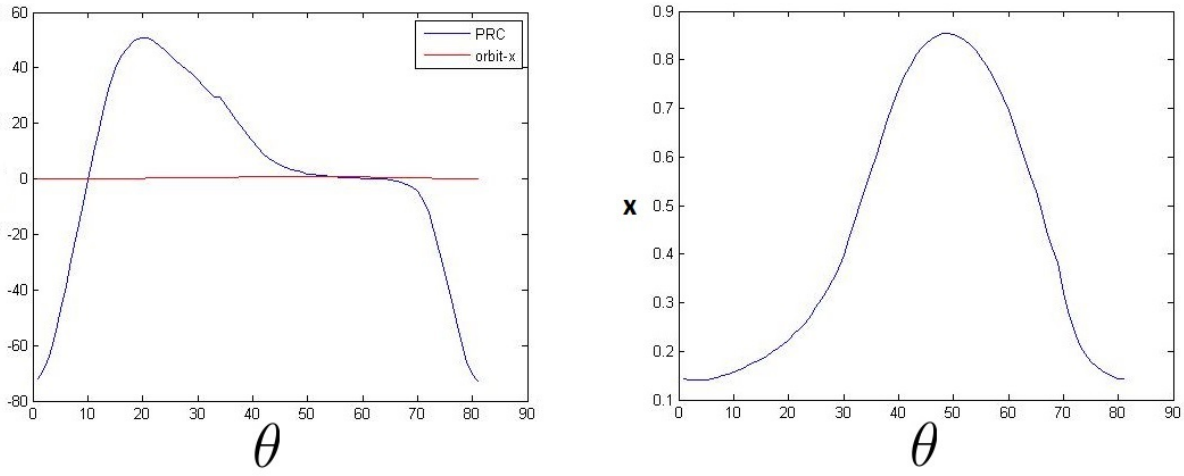

Figure 2.9: Both orbit and phase response curves of Wilson-Cowan model for same phase via CIMatCont in the first figure. The second figure presents only orbit of Wilson-Cowan model. The values of parameters are $c_1 = 10$, $c_2 = 10$, $c_3 = 10$, $c_4 = -2$, $P = -3.5$ and $Q = -8.5$.

When PRCs are computed in MatCont and XPP, they do not tend to be totally same. So, we checked the orbits for a specific parameter values of points in both programme to understand why they are different. The reason for different PRCs in MatCont and XPP is that PRC has many components in the model. While XPP calculates all of them, only one of the components can be produced in MatCont. Therefore, changing order of the equations helps to calculate PRC for different components.

XPP gives us both the x and y components of the PRC for both the xy order of equations which is (2.5.1) and yx order of equations which are (2.5.2), so we can compare x from each case in XPP. Then, we find that they are the same. On the other hand, MatCont only gives you the first component of the PRC, so from the xy order you can get x and from the yx order you can get y, but you cannot get x from each case and check they are the same. When the order is changed, the coupling term is added at the other equation and we do not expect any difference on the behaviour of the model.

The new ordered system becomes

$$\begin{aligned} y' &= -y + Q + c_3 f(x) - c_4 f(y), \\ x' &= -x + P + c_1 f(x) - c_2 f(y). \end{aligned} \tag{2.5.2}$$

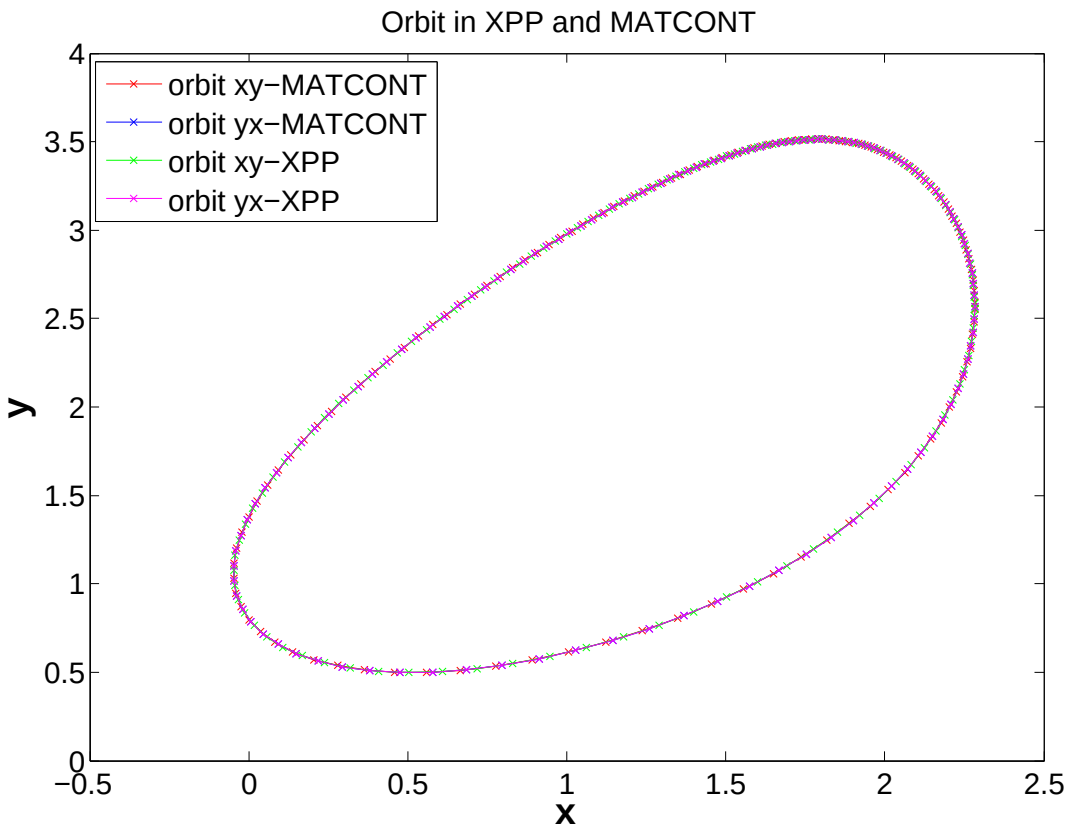

Figure 2.10: Orbits of Wilson-Cowan model for same parameters via CIMatCont and XPP. The parameters are $c_1 = 10$, $c_2 = 10$, $c_3 = 10$, $c_4 = -2$, $P = 2.5$ and $Q = -7$.

In the figure 2.10, the orbits produced via MatCont and XPP for the xy and yx order of equations are quite similar to each other. So, it is expected to obtain similar PRCs.

The model has the same orbits for both orders, but not on the same time scale. In the figure 2.11 on the right that the period of the orbit has been scaled to 1 while on the left figure the period of the orbit has been scaled to $[0, \theta]$. After performing a time-shift, we expect to produce the same orbits. Indeed, when we shift PRC which is produced from the yx order of equations, we get a broadly similar PRC to that produced with the xy order in XPP. We shift them, since the orbits do not start at the same point of the cycle, so they have different initial values. We would like to have a wide range of PRCs, MatCont can only produce one at once, however XPP is useful to produce many of them. Figure 2.11 shows PRCs and orbits together with shifted versions in both programme.

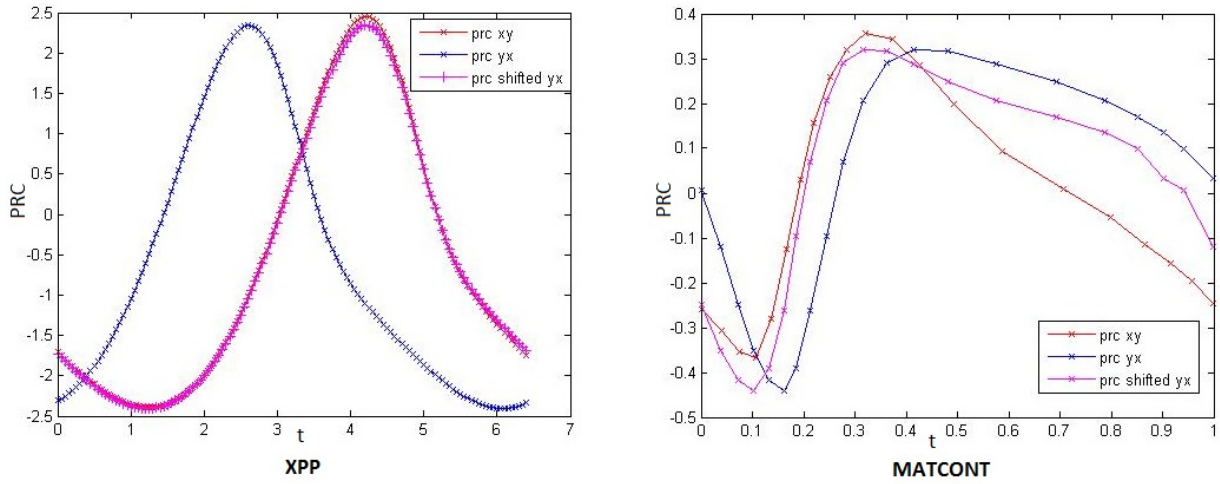

Figure 2.11: PRCs of Wilson-Cowan model for same parameters via CIMatCont and XPP. The parameters are $c_1 = 10$, $c_2 = 10$, $c_3 = 10$, $c_4 = -2$, $P = 2.5$ and $Q = -7$. prc xy means PRC of x component, prc yx denotes PRC of y component. We do not expect to get same PRC for the 1st (x) and 2nd (y) components. In the figure on the right that the period of the orbit has been scaled to 1 while on the left figure the period of the orbit has been scaled to $[0, \theta]$.

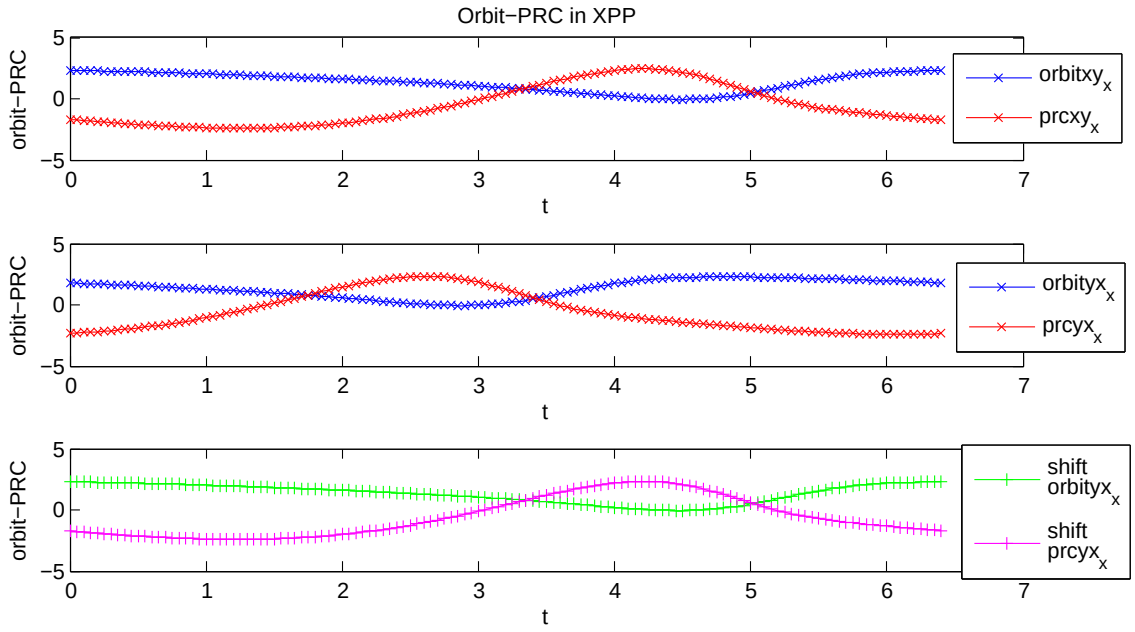

Figure 2.12: Orbits and PRCs with their shifted version of Wilson-Cowan model via XPP. In the figure the period of the orbit has been scaled to $[0, \theta]$. The parameters are $c_1 = 10$, $c_2 = 10$, $c_3 = 10$, $c_4 = -2$, $P = 2.5$ and $Q = -7$.

It can be seen that the first figure (xy order) and last figure (shifted yx order) are quite similar in both figure 2.12 and 2.13.

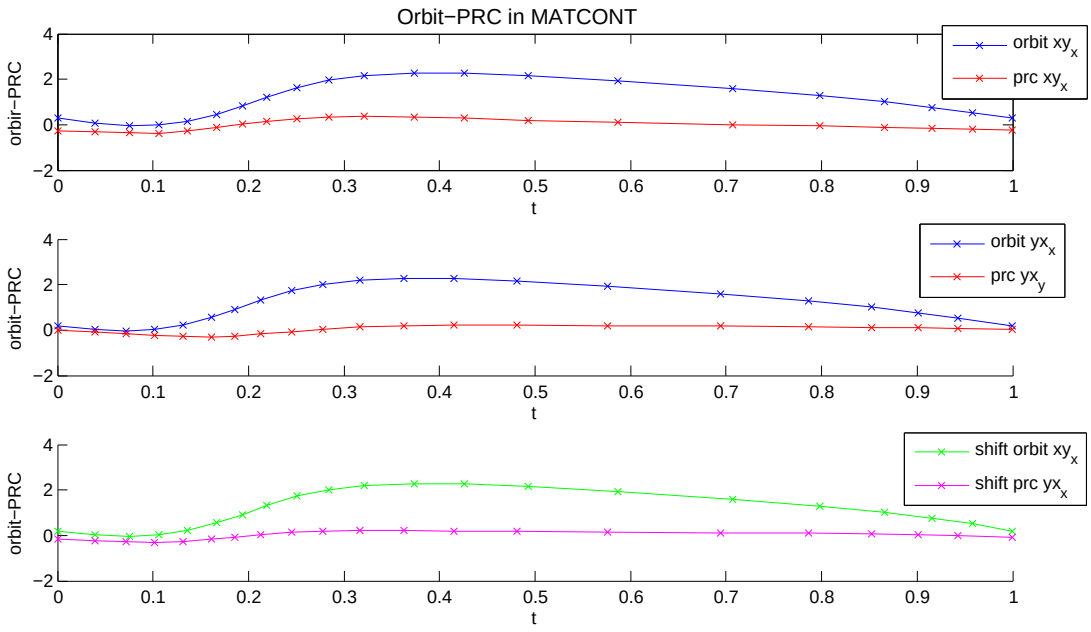

Figure 2.13: Orbits and PRCs with their shifted version of Wilson-Cowan model via MatCont. In the figure the period of the orbit has been scaled to 1. The parameters are $c_1 = 10$, $c_2 = 10$, $c_3 = 10$, $c_4 = -2$, $P = 2.5$ and $Q = -7$.

XPP is a package programme, so it is more effective way to calculate PRCs. MatCont is a black box and that of the two results we trust those from XPP, as this is a tried and tested software tool that is used widely in the coupled oscillator community. Therefore, we check the calculation of PRCs in MatCont for the changing value of some parameters, such as number of mesh points (ntst) to be used in discretisation. When the number of mesh points is increased, smoother PRCs are obtained in the figure 2.14. Furthermore, the default integration method in MatCont is ODE45 which is based on Runge-Kutta (4, 5) method. However, XPP uses 4th order Runge-Kutta method.

We get similar PRCs from XPP and MatCont. The accuracy of the system in MatCont should be increased in order to produce same PRCs. When the number of mesh points are increased, smoother PRCs can be calculated. Therefore, the mesh points of the system affects the PRCs. Furthermore, simulation are produced through only a graphical user interface (GUI) in XPP while MatCont produces simulations via GUI and manual. We used the command line continuation toolbox ClMatCont to calculate PRCs. Therefore, we can save data and produce a great number of PRCs.

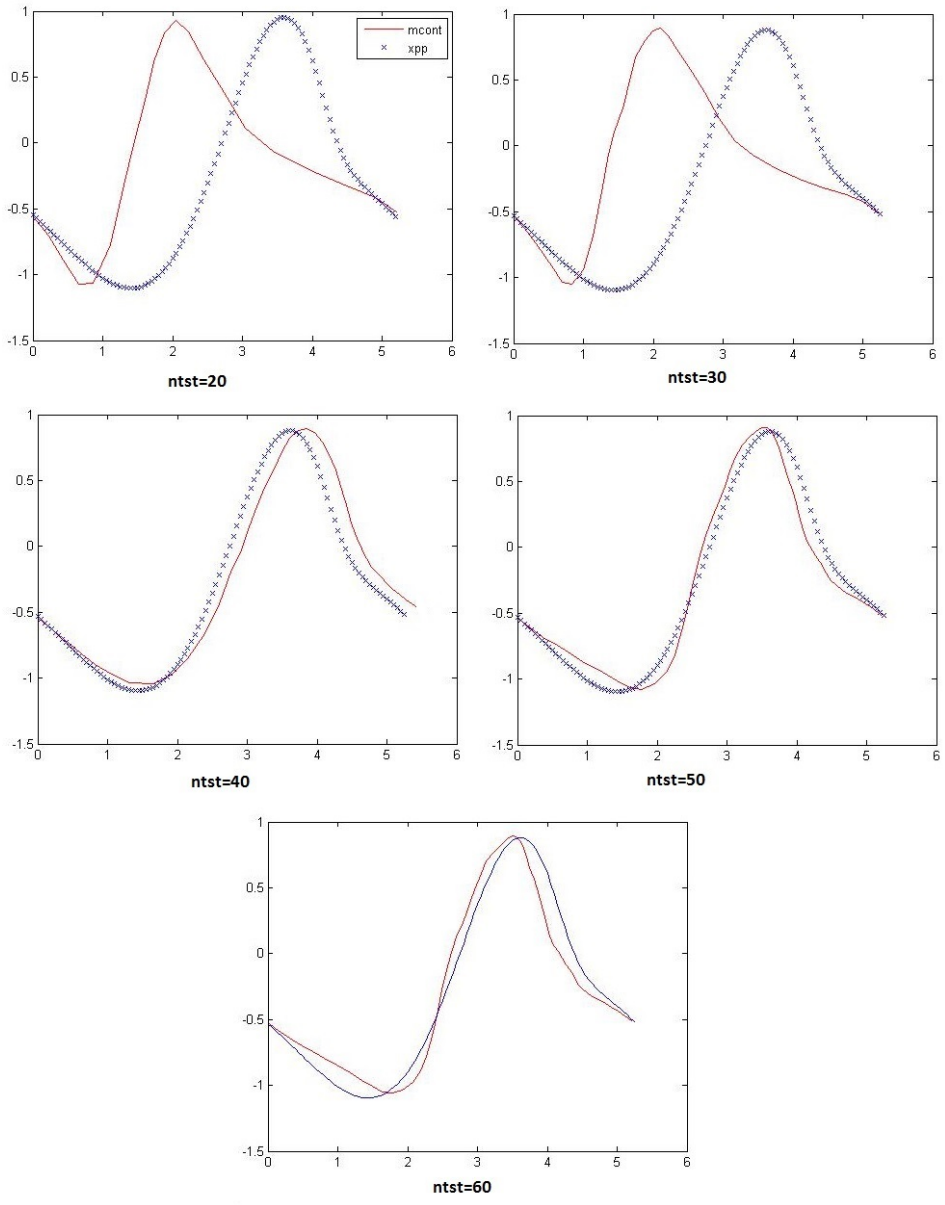

Figure 2.14: x component of PRCs for the altered value of number of mesh points. The blue curves are produced in XPP, while the red curves are obtained from MatCont. Smoother PRCs are produced when the number of mesh points is increased. The parameters are $c_1 = 10$, $c_2 = 10$, $c_3 = 10$, $c_4 = -2$, $P = 2.5$ and $Q = -7$.

2.6 Adjoint Method : PRC Calculation

It is common practice in neuroscience to characterise a neuronal oscillator in terms of its phase response to a perturbation [94]. This gives an increase to the notion of a so-called phase response curve, which for a real neuron can be determined experi-

mentally [40, 114, 81]. PRCs can also be related to the post stimulus time histogram [48]. Following [9], a dynamical system $\dot{Z} = F(Z)$, $Z \in \mathbb{R}^N$ with a T-periodic solution $u(t) = u(t+T)$ and an infinitesimal perturbation ΔZ_0 to the trajectory $u(t)$ at time $t = 0$ are considered. This perturbation evolves according to the linearised equation of motion:

$$t\Delta Z = DF(u(t))\Delta Z, \qquad \Delta Z(0) = \Delta Z_0.$$

Here $DF(u)$ denotes the Jacobian of F evaluated along u. Introducing a time-independent *isochronal* phase shift $\Delta\theta$ as $\theta(u(t) + \Delta u(t)) - \theta(u(t))$, we have to first order in ΔZ that

$$\Delta\theta = \langle Q(t), \Delta Z(t)\rangle, \tag{2.6.1}$$

where $\langle\cdot,\cdot\rangle$ defines the standard inner product, and $Q = \nabla_u\theta$ is the gradient of θ evaluated at $u(t)$. Taking the time-derivative of (2.6.1) gives

$$\langle tQ, \Delta Z\rangle = -\langle Q, t\Delta Z\rangle = -\langle Q, DF(u)\Delta Z\rangle = -\left\langle DF^T(u)Q, \Delta Z\right\rangle.$$

Since the above equation must hold for arbitrary perturbations, we see that the gradient $Q = \nabla_u\theta$ satisfies the linear equation

$$tQ = D(t)Q, \qquad D(t) = -DF^T(u(t)), \tag{2.6.2}$$

subject to the boundary conditions

$$\langle \nabla_{u(0)}\theta, F(u(0))\rangle = 1 \text{ and } Q(t) = Q(t+T).$$

The first condition simply guarantees that $\theta = 1$ (at any point on the periodic orbit), and the second enforces periodicity.

T-periodic vector function Z satisfies the linear adjoint equation which is denoted as

$$\frac{\mathrm{dZ(t)}}{\mathrm{dt}} = -DF^T(u(t))Z(t) \tag{2.6.3}$$

where $DF^T(u(t))$ is the transposed Jacobian matrix of F function at point $u(t)$. The normalisation form is $Z(t)F(u(t)) = 1$ for any t, as denoting $\frac{\mathrm{d}}{\mathrm{dt}}(Z(t)F(u(t))) = 0$ is easy [83, 99, 31]. A vector of components in the N differential equations along the limit cycle

is represented by $Z(t)$ [99]. Each component of the equations reflects the phase shift [63, 84].

The phase response curve is described through the timespan of one cycle in the spike train of a firing neuron with no extra input. Its starting point is the peak of a spike, then it continues until the peak of the following spike. The PRC is positive if it advances the timing of the following spike. However, it is negative if it delays the timing of the following spike [58].

In general, equation (2.6.2) must be solved numerically to obtain the PRC, for example using the *adjoint* routine in XPPAUT [32] or MatCont [45]. The adjoint method gives a different approach derivation of the phase reduced equation [83]. This method is based on the backward integration of the adjoint linear equation of the dynamical system. This is a general and mathematically defined method which does not use spikes. The adjoint method uses differential equations rather than perturbations.

The adjoint system has the opposite stability situation to the original system. Although the original system is asymptotically stable, the adjoint is unstable, so a direct indirect integration is not possible. Ermentrout used the backward integration in time [31], and which allowed him to find the periodic solution of equation (2.6.3) corresponding to the PRC.

PRCs of the Wilson-Cowan model are calculated by using the adjoint method.

$$\dot{x} = -x + f(c_1 x - c_2 y + P), \tag{2.6.4}$$

$$\dot{y} = -y + f(c_3 x - c_4 y + Q) \tag{2.6.5}$$

where $f(x) = \frac{1}{1+e^{-x}}$.

$$\frac{dZ}{dt} = \begin{bmatrix} \frac{\partial}{\partial x}\dot{x} & \frac{\partial}{\partial x}\dot{y}, \\ \frac{\partial}{\partial y}\dot{x} & \frac{\partial}{\partial y}\dot{y} \end{bmatrix}^T \begin{bmatrix} x \\ y \end{bmatrix} \tag{2.6.6}$$

where $Z = (x, y)'$.

The system with the adjoint method becomes

$$\dot{x} = -1 + c_1 x\dot{f}(x) + c_3 y\dot{f}(y), \tag{2.6.7}$$

$$\dot{y} = -1 - c_2 x\dot{f}(x) - c_4 y\dot{f}(y) \tag{2.6.8}$$

In figure 2.15 and 2.16, the orbit and PRC are plotted in MATLAB by using the adjoint method, as XPP uses the adjoint method for calculation of them. Therefore, the orbit and PRC plotted in MATLAB are comparable with the orbit and PRC plotted in XPP.

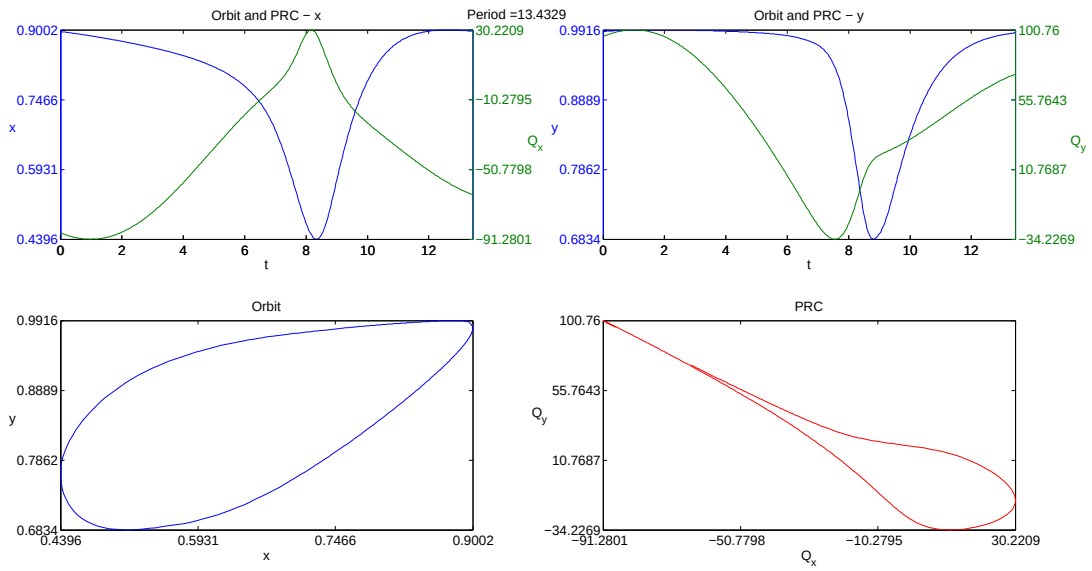

Figure 2.15: The figure shows the blue curves for the orbits and green curves for x and y component of PRCs via adjoint method. The parameters are $c_1 = 10$, $c_2 = 10$, $c_3 = 10$, $c_4 = -2$, $P = 3$ and $Q = -6$.

The top left figure 2.15 shows the orbit with blue curve and x components of PRC with green curve via adjoint method in MATLAB. The top right represents the orbit with blue curve and y components of PRC with green curve. While the bottom left figure produces the orbit in $x - y$ plane, the bottom right figure shows the PRC in x and y components of PRC plane.

The top left figure 2.16 denotes the orbit with blue curve and x components of PRC with green curve via adjoint method in XPP. The top right shows the orbit with blue

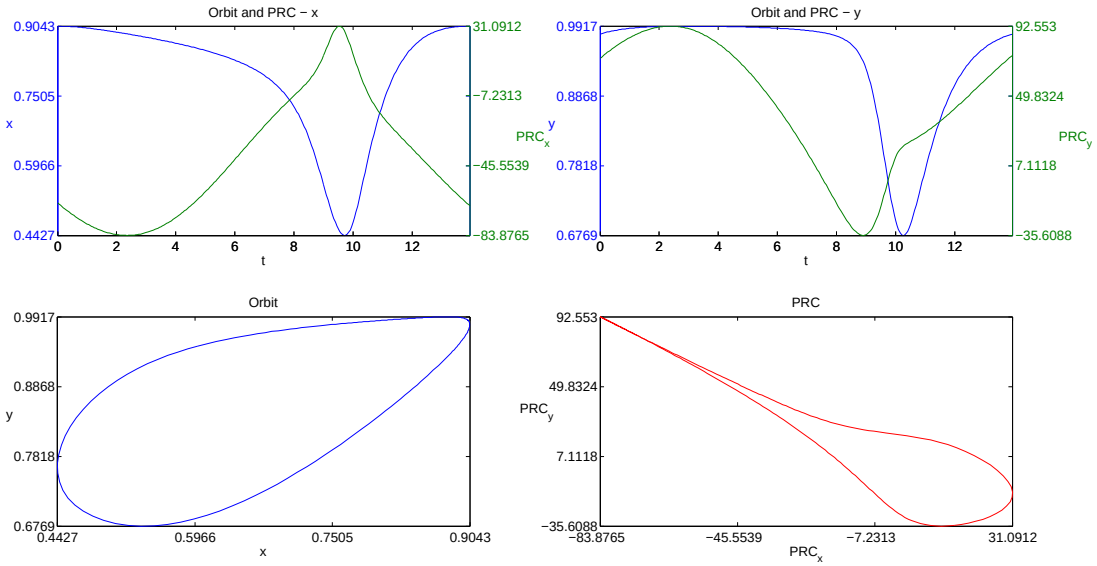

Figure 2.16: The figure shows the blue curves for the orbits and green curves for x and y component of PRCs via XPP. The parameters are $c_1 = 10$, $c_2 = 10$, $c_3 = 10$, $c_4 = -2$, $P = 3$ and $Q = -6$.

curve and y components of PRC with green curve. The bottom left figure presents the orbit in $x - y$ plane, and the bottom right figure shows the PRC in x and y components of PRC plane. Therefore it is seen from figures 2.16 and 2.15 the both methods produce the same orbits and so PRCs for the same values of parameters.

2.7 Phase Interaction Functions

Calculation of the PRC has an important role: it can be used to obtain the phase interaction function (PIF). The PIF can be obtained from the phase response curve and the sigmoid function of the periodic orbit. In the light of the theory of weakly coupled oscillators, phase-locked network states are defined via the PIF [21, 103].

Consider a dynamical system $\dot{X} = F(X)$ with a $T-$periodic solution: $X(t) = X(t+T)$ and $X \in \mathbb{R}^M$. There is a continuous transformation that maps solutions of the weakly coupled network of M oscillators [88] in figure 2.17.

$$\dot{X}_i = F(X_i) + \epsilon G_i(X_1, X_2, ..., X_M), \quad \epsilon \ll 1. \tag{2.7.1}$$

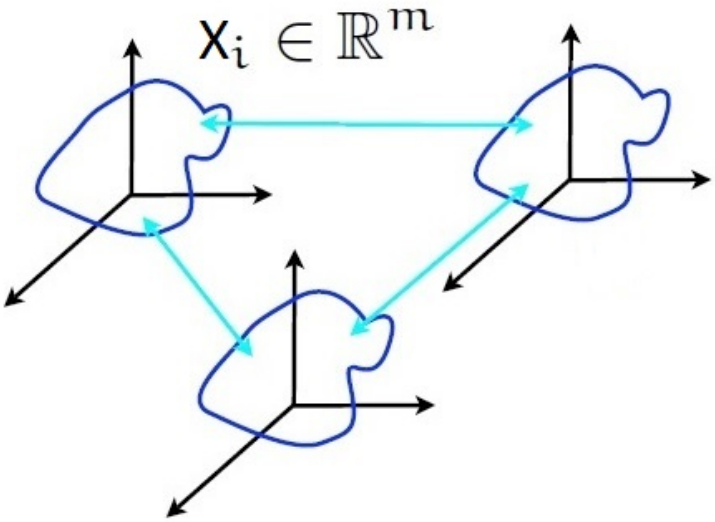

Figure 2.17: The figure represents a set of interacting high dimension oscillators and the weakly connected network.

where X_i is the activity of the ith neuron, F_i governs its dynamics, G_i represents connections converging from the entire system to the ith neuron. The weakly connected system is transformed into the phase model θ in figure 2.18.

The gradient of isochrons is given by

$$K = \nabla_x \theta \tag{2.7.2}$$

where $\dot{\theta} = 1/T$ over the limit cycle. $\dot{\theta} = K \cdot F = 1/T$ if $\epsilon = 0$.

$$\frac{d\theta}{dt} = \nabla_x \theta . \frac{dX}{dt} = \nabla_x \theta (F + \epsilon G) = \langle K, F \rangle = \frac{1}{T} + \epsilon KG \tag{2.7.3}$$

where $< ., . >$ indicates the standard inner product.

$$\dot{\theta}_i = \frac{1}{T} + \epsilon \langle K_i, G_i(\theta_1, ..., \theta_M) \rangle \quad \theta_i \in S^1 \tag{2.7.4}$$

We can define $G_i = \epsilon \sum_j \widehat{G_j} w_{ij}$ where w_{ij} refers to the structural connectivity, and

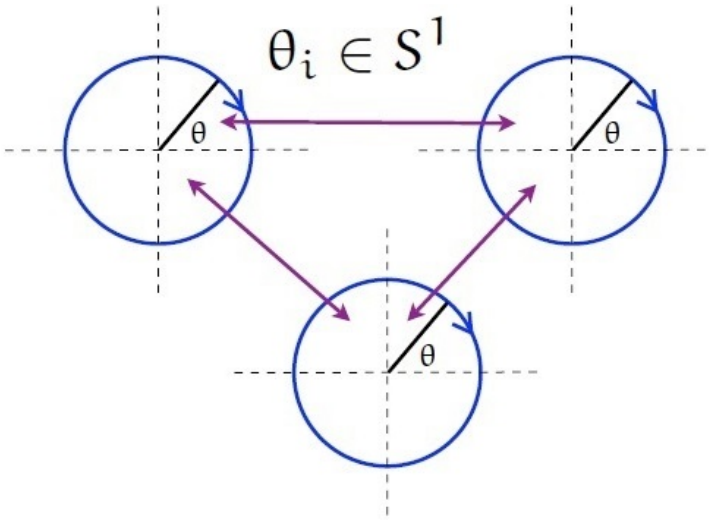

Figure 2.18: The figure denotes transformation of the phase model. The oscillatory weakly connected system in figure 2.17 can be reduced to a phase model.

$K_i \in \mathbb{R}^M$, and $G_i \in \mathbb{R}^M$. ϵG_i denotes a weak time dependent input from other oscillators in a network. Also, K_i is the phase response vector of ith neuron.

This has the form with $h = K_i \sum G_{ij}$ and can be written

$$\dot{\theta}_i = \frac{1}{T} + \epsilon \sum_{j=1}^{N} h(\theta_i, \theta_j) \tag{2.7.5}$$

where $h = K_i G_{ij}$ and G_{ij} indicates the time course of the synaptic input. This form is challenging to work with these equations, so the system is transformed to simplifier averaging form. The natural way to obtain a phase-difference model from (2.7.4) is, as in the section on periodically forced oscillators, to average over one period of oscillation. Then, this is averaged to the phase model. For simplicity, let us assume that all the oscillators are identical with a common periodic orbit and the new phase becomes $\theta_i \rightarrow \theta_i - t/T$, so its derivative becomes $\dot{\theta}_i \rightarrow \dot{\theta}_i - 1/\mathrm{T}$. Equation ((2.7.5)) is written as

$$\dot{\theta}_i = \epsilon h \left(\theta_1 + \frac{t}{T}, \theta_2 + \frac{t}{T}, ..., \theta_N + \frac{t}{T} \right) \tag{2.7.6}$$

Here, ϵ is small, so θ_i is slow and does not really change, then $1/T \int_t^{t+T} ... \, dt$ is applied to both sides and averaged to

$$\dot{\theta}_i = \epsilon \frac{1}{T} \int_{-\theta_i T}^{T-\theta_i T} h\left(\theta_1 + \frac{t'}{T}, \theta_2 + \frac{t'}{T}, ...\right) dt' \tag{2.7.7}$$

$$\dot{\theta}_i = \epsilon \frac{1}{T} \int_{0}^{T-\theta_i T} h\left(\theta_1 - \theta_i + \frac{t}{T}, \theta_2 - \theta_i + \frac{t}{T}, ...\right) dt' \tag{2.7.8}$$

$$\dot{\theta}_i = \frac{1}{T} + \epsilon \sum_{j=1}^{N} H(\theta_j - \theta_i) \tag{2.7.9}$$

where $\theta \in [0, 1)$. The periodic function H is referred to as the *phase interaction function* where

$$H = \lim_{x \to \infty} \frac{1}{T} \int_0^T h(\theta_i t, \theta_j t) \mathrm{d}t \tag{2.7.10}$$

In the light of weak coupling, the relative phase of the oscillators changes slowly with respect to their motion around the limit cycle. This causes the slow convergence to a steady state phase locking.

The phase interaction function is defined with the equation

$$H(\theta) = \frac{1}{T} \int_0^T K(\psi) f(x(\psi + \theta T)) \, \mathrm{d}\psi. \tag{2.7.11}$$

K represents the PRC and f is the sigmoid function of the orbit. PRC can be defined by using Fourier series.

$$K(\psi) = \sum_{n \in \mathbb{Z}} K_n e^{2\pi i n \frac{\psi}{T}} \tag{2.7.12}$$

$$f(x(\psi)) = \sum_{n\in\mathbb{Z}} f_n e^{2\pi i n\frac{\psi}{T}} \tag{2.7.13}$$

$$H(\theta) = \frac{1}{T}\int_0^T \sum_n K_n e^{2\pi i n\frac{\psi}{T}} \sum_m f_m e^{2\pi i m\frac{\psi+\theta T}{T}}\, \mathrm{d}\psi \tag{2.7.14}$$

$$H(\theta) = \sum_{n,m} K_n f_m e^{2\pi i m\theta}\frac{1}{T}\int_0^T e^{2\pi i(n+m)\frac{\psi}{T}}\, \mathrm{d}\psi = \sum_n K_n f_{-n} e^{-2\pi i n\theta} \tag{2.7.15}$$

$$H'(0) = -\sum_{n\in\mathbb{Z}} K_n f_{-n}(2\pi i n) \tag{2.7.16}$$

Note that certain caution has to be exercised in applying averaging theory. In general, one can only establish that a solution of the unaveraged equations is ϵ-close to a corresponding solution of the averaged system for times of $O(\epsilon^{-1})$. No such problem arises in the case of hyperbolic fixed points corresponding to phase-locked states.

We used the numerical tool to calculate the Fourier coefficients, then the phase response curve and sigmoidal function generated by the phase. In addition to this, f_{-n} can be calculate using the same steps. Then, PIF was calculated by using the PRC and the periodic orbit function. We obtained different H function, and hence different $H'(0)$, because of having not totally same PRC in XPP. The difference between the PRCs from XPP and MatCont is a question of accuracy.

It can be seen in figures 2.19 and 2.20 that the orbits and the phase response curves for different points were produces in XPP and MatCont. On the other hand, the phase interaction functions and the derivative of phase interaction functions were just produced via XPP. The orbits are quite similar for the given parameters, so phase response curves look like each other in both figures.

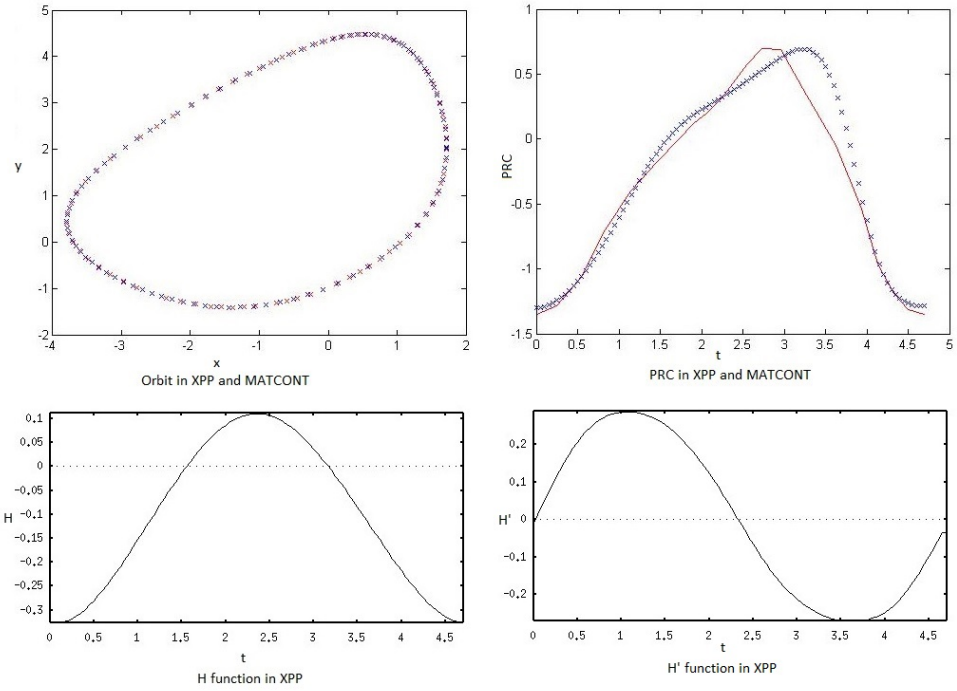

Figure 2.19: The PRC, PIF and its derivative via XPP. Red indicates MATCONT,and blue is from XPP. The parameters are $c_1 = 10$, $c_2 = 10$, $c_3 = 10$, $c_4 = -2$, $P = 2.1$ and $Q = -3.8$.

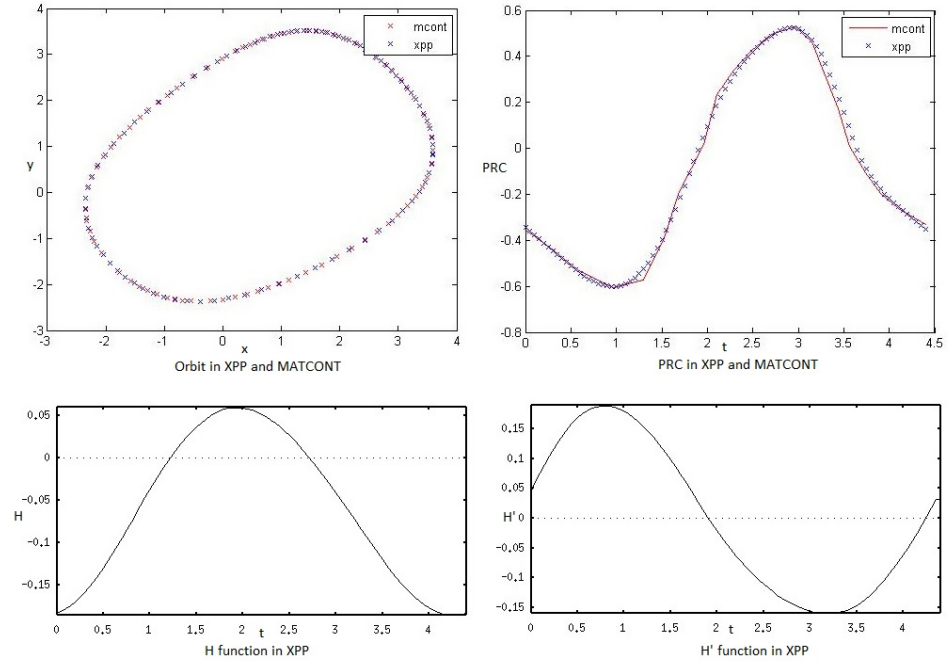

Figure 2.20: The PRC, PIF and its derivative via XPP. While red denotes MATCONT, blue shows XPP. The parameters are $c_1 = 10$, $c_2 = 10$, $c_3 = 10$, $c_4 = -2$, $P = 1$ and $Q = -6.5$.

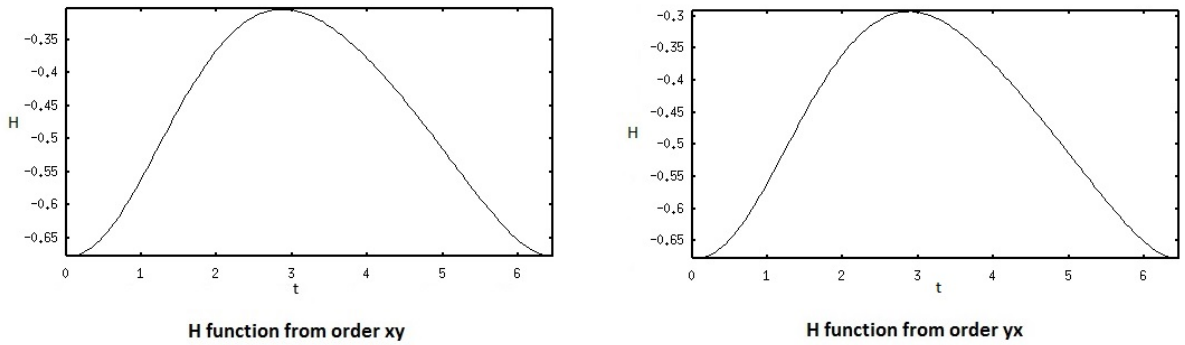

Figure 2.21: The phase interaction function of Wilson-Cowan model via XPP. The parameters are $c_1 = 10$, $c_2 = 10$, $c_3 = 10$, $c_4 = -2$, $P = 2.5$ and $Q = -7$.

As mentioned in Section 2.5, when the order of equations is changed, the orbits stay same. However, PRCs are not exactly same to each other, so the phase interaction functions produced in XPP are quite similar but not the same. Since when the order of equation is altered, the different components of the model (x or y components) are used to produce PRC. Therefore, the PIFs are not totally same in changed order of equations. They are shown in figure 2.21.

2.8 Phase Locked States

We define a 1:1 phase-locked solution to be of the form $\theta_i(t) = \phi_i + \Omega t$, where ϕ_i is a constant phase and Ω is the collective frequency of the coupled oscillators. Each oscillator approximately fires at its natural frequency Ω in the weakly coupled systems. Substitution into the averaged system (2.7.9) gives

$$\Omega = \epsilon \sum_j w_{ij} H(\phi_j - \phi_i). \tag{2.8.1}$$

After choosing some reference oscillator, N phase-locked solutions of (2.7.9) determine the collective frequency Ω and $N - 1$, relative phases with the latter being independent of ϵ.

In order to analyse the local stability of a phase-locked solution $\Phi = (\phi_1, \ldots, \phi_N)$, we linearise the system by setting $\theta_i(t) = \phi_i + \Omega t + \widetilde{\theta}_i(t)$ and expanding to first-order in $\widetilde{\theta}_i$:

$$\frac{\mathrm{d}\widetilde{\theta}_i}{\mathrm{d}t} = \epsilon \sum_j \widehat{\mathcal{H}}_{ij}(\Phi)\widetilde{\theta}_j, \tag{2.8.2}$$

where

$$\widehat{\mathcal{H}}_{ij}(\Phi) = \epsilon \left[w_{ij} H'(\phi_j - \phi_i) - \delta_{ij} \sum_k^N w_{ik} H'(\phi_k - \phi_i) \right], \tag{2.8.3}$$

and $H'(\phi) = \mathrm{d}H(\phi)/\mathrm{d}\phi$.

One of the eigenvalues of the Jacobian $\widehat{\mathcal{H}}$ is always zero, and the corresponding eigenvector points in the direction of the flow, that is $(1, 1, \ldots, 1)$. The phase-locked solution will be stable provided that all other eigenvalues have a negative real part.

2.9 Stability of Synchronised Solution

2.9.1 Synchrony

Synchrony is an alteration of rhythms of self sustaining oscillators because of their weak interactions [90]. Meanwhile, the phase synchrony is the period of time where there is a stable near zero first derivative of the instantaneous phase difference [90].

Computation of the phase interaction function helps us to determine the stability of the fully synchronised solution [52]. Although stability is identified by the positive sign of $H'(0)$, instability is characterised by the negative sign of $H'(0)$.

The phase interaction function is described by the product of the phase response vector of oscillator i and the interaction from oscillator j. It can be constructed via XPPAUT which is a convenient tool to simulate and solve numerically the equations in the dynamical systems [32]. However, this tool is not suitable to obtain many PRCs for the

various values of parameters. So, CIMatCont, which is the command line continuation toolbox, is used to calculate PRC, then obtain PIF.

The set of ordinary differential equations (2.3.1) allow us to define the stability of the synchronous state ($\theta_i = \theta \ \ \forall \ \ i$) which is important to construct FC. $\hat{H}$, which is $N \times N$ matrix, is determined by rotating the form of equation (2.7.9):

$$\dot{\theta}_i = \frac{1}{T} + \sum_j w_{ij} H(\theta_j - \theta_i) \tag{2.9.1}$$

A synchronous solution of this equation is

$$\dot{\theta}_i(t) = \Omega \quad \text{for} \quad \forall i \tag{2.9.2}$$

$$\theta_i(t) = \Omega t \quad \text{for} \quad \forall i \tag{2.9.3}$$

with the perturbation

$$\theta_i(t) = \Omega t + \widetilde{\theta}_i \quad \text{for} \quad \forall i \tag{2.9.4}$$

where $\Omega = \frac{1}{T} + \sum_j w_{ij} H(0)$. Ω is the frequency of synchronous solutions and $\frac{1}{T}$ is the frequency of single neuron. The sum is too small due to the weakly coupling theory. That equation must be true for all value of i:

i) If $H(0) = 0$, then $\Omega = \frac{1}{T}$, so independent of i. In other words, one way for this to be true for all j is if $H(0) = 0$, which is true say for $H(\theta) = \sin(2\pi\theta/\Delta)$ or for *diffusive coupling*, which is linear in the difference between two state variables so that $H(0) = 0$. The existence of synchronous solutions is also guaranteed if $\sum_{j=1}^{N} w_{ij}$ is independent of i. This would be the case for *global coupling* where $w_{ij} = 1/N$, so that the system has permutation symmetry.

ii) If $\sum_j w_{ij} = \Gamma = constant$, then $\Omega = \frac{1}{T} + H(0)\Gamma$.

For instance, let us consider $\sum_j w_{ij} = \Gamma$ for $w_{ij} = \frac{1}{N}$, and it yields $\Gamma = \sum_{j=1}^{N} = 1$.

Substitution of the equation (2.9.4) into equation (2.9.1) yields

$$\frac{d}{dt}(\Omega t + \widetilde{\theta}_i) = \frac{1}{T} + \sum_j w_{ij} H(\widetilde{\theta}_j - \widetilde{\theta}_i) = \frac{1}{T} + \sum_j w_{ij} H(\Omega t - \widetilde{\theta}_j - (\Omega t - \widetilde{\theta}_i)) \tag{2.9.5}$$

$$\Omega + \frac{d}{dt}(\widetilde{\theta}_i) = \frac{1}{T} + \sum_j w_{ij}(H(0) - H'(0)[\widetilde{\theta}_j - \widetilde{\theta}_i]) \tag{2.9.6}$$

$$\frac{d}{dt}(\widetilde{\theta}_i) = H'(0) \sum_j w_{ij}(\widetilde{\theta}_j - \widetilde{\theta}_i) = H'(0)(\sum_j w_{ij} - \sum_k w_{ik}\delta_{ij})\widetilde{\theta}_j \tag{2.9.7}$$

$$\widehat{H_{ij}} = H'(0) \left[w_{ij} - \delta_{ij} \sum_k w_{ik} \right] \tag{2.9.8}$$

where $H' = dH(\theta)/d\theta$.

If the synchronous solution exists then the Jacobian is given by $\epsilon H'(0)\mathcal{L}$ where $\mathcal{L}$ is the *graph Laplacian* with components:

$$\mathcal{L}_{ij} = w_{ij} - \delta_{ij} \sum_k w_{ik}.$$

The stability of synchronised solution depends on the eigenspectra of the Jacobian $\widehat{H_{ij}}$ of the linearised perturbation equation as seen in figure 2.22. This matrix is related to the phase interaction function $H'(0)$ and the structural connectivity w_{ij}.

We note that $\mathcal{L}$ has one zero eigenvalue, with eigenvector $(1, 1, \ldots, 1, 1)$. Hence, if all other eigenvalues of $\mathcal{L}$ lie on one side of the imaginary axis, then stability is solely determined by the sign of $\epsilon H'(0)$. For global coupling, we have that $\mathcal{L}_{ij} = N^{-1} - \delta_{ij}$, and the ($N - 1$ degenerate) eigenvalue is -1 where N is number of the nodes. Hence, the synchronous solution will be stable provided $\lambda = -\epsilon H'(0) < 0$.

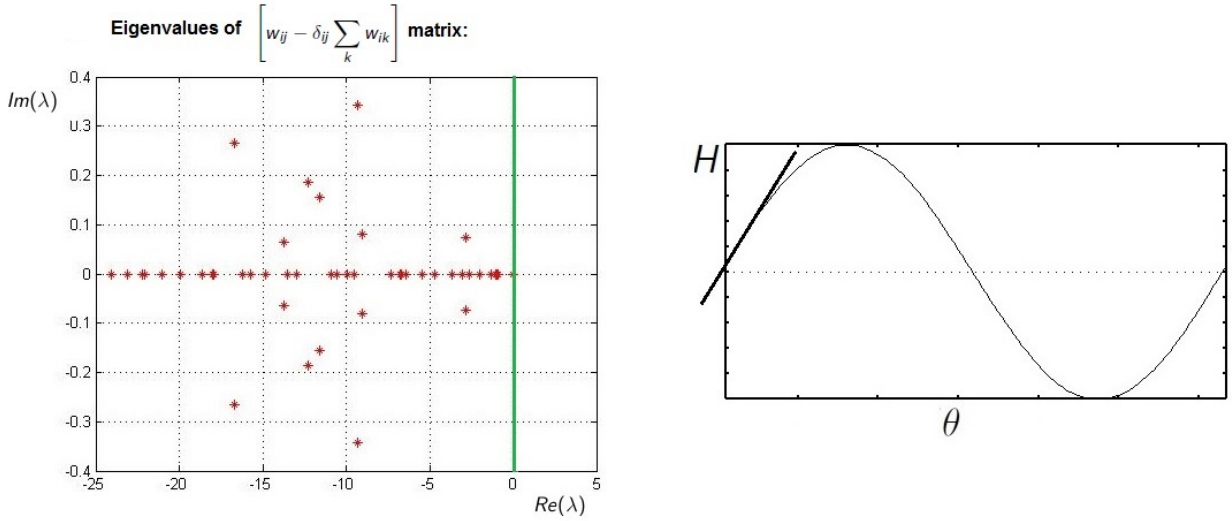

Figure 2.22: The eigenvalues of the graph Laplacian for the anatomical network structure of the Macaque monkey brain - generated from CoCoMac database. The left figure indicates the sign of the gradient of phase interaction function at origin.

If one eigenvalue is always zero and all the remaining ones have negative real parts, the solution becomes stable. If phase differences are all zero, we reach a synchronous solution. Moreover, if at least one eigenvalue has positive real parts, $Tr\widehat{H} > 0$, we have the instability of the synchronous state. Thus, if $H'(0) > 0$, the solution is stable, and if $H'(0) < 0$, the solution is unstable.

Global synchrony is the synchrony of all neural oscillators. However, we pay attention to the complex patterns of partial synchrony. If $H'(0) > 0$, the nodes which are connected by a structural link become synchronised, and the agreement between SC and FC is seen. If $H'(0) < 0$, the nodes which are connected by a structural link become unsynchronised, and disagreement between SC and FC is found.

While $H'(0)$ is produced from the Fourier series in figure 2.22, the equations below are used to compute $H'(0)$ in figure 2.23. H is defined as in equation (2.7.11), and K is calculated using Adjoint method. K and f are periodic, so they can be written

$$H(\theta) = \frac{1}{T}\int_0^T K(\psi - \theta) f(x(\psi))\,\mathrm{d}\psi \tag{2.9.9}$$

$$H'(\theta) = -\frac{1}{T}\int_0^T K'(\psi - \theta) f(x(\psi))\,\mathrm{d}\psi \tag{2.9.10}$$

$$H'(0) = \frac{1}{T}\int_0^T K'(\psi) f(x(\psi))\,\mathrm{d}\psi. \tag{2.9.11}$$

Therefore, $H'(0)$ is formulised by the inner product of K' and f.

$$H'(0) = -\frac{1}{T} < K', f > . \tag{2.9.12}$$

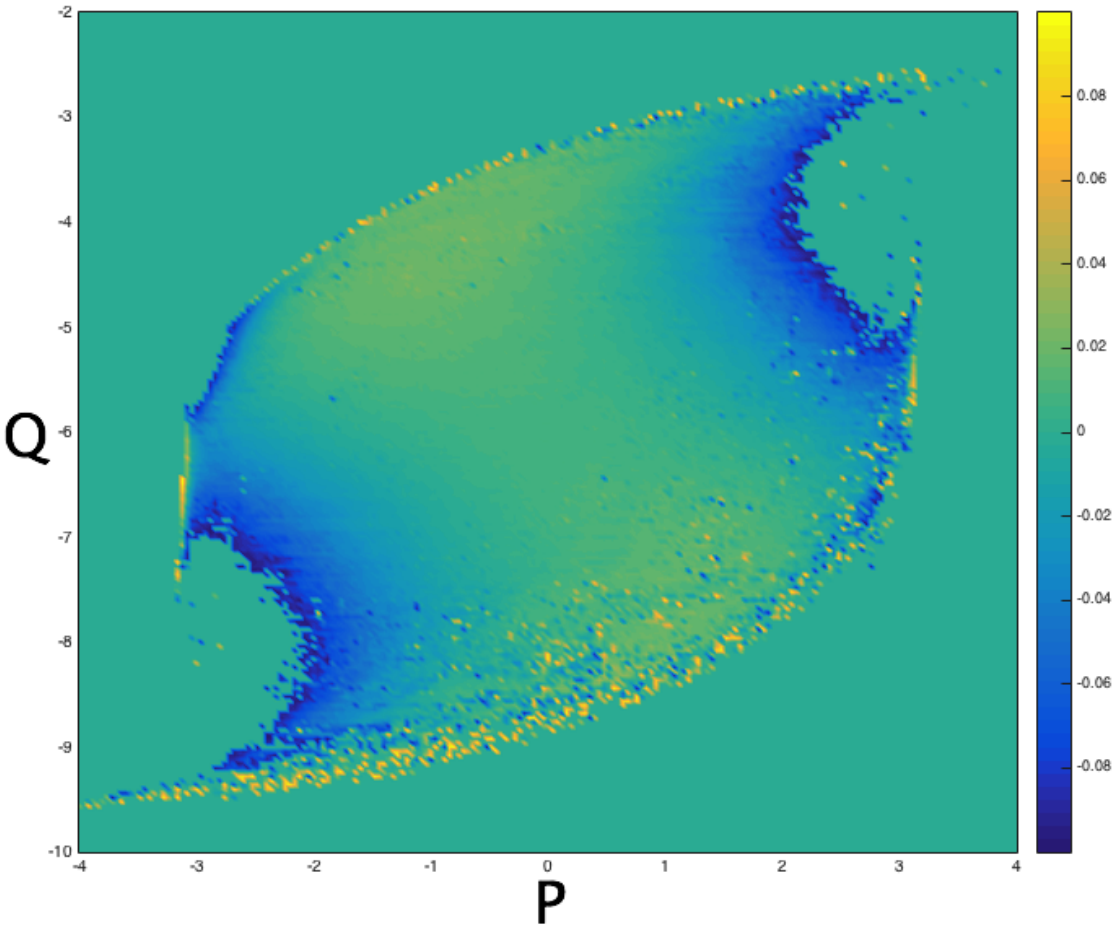

Figure 2.23: A stability of synchronous solution for weakly coupled network of WilsonCowan oscillators by using $H'(0)$. Positive value of $H'(0)$ corresponds to stability while the negative value of $H'(0)$ represents instability.

Furthermore, the values of $H'(0)$, computed by the equations above, can be seen in $P-Q$ parameter regions in figure 2.23. Synchrony instability is in the overall large central area of eye-shaped region. The border along the eye-shape bifurcation is dedicated to the limit cycle region. The network has more patterns of activity in the areas of instability of synchronous solutions. In contrast, when the synchronous solution is stable in $P-Q$ space, the functional connectivity resembles the underlying structural connectivity.

2.10 Discussion and Conclusion

This study indicates that the measurement of FC depends on the parameters of the model. In addition to this, they affect the agreement between the FC and SC. In this report the weakly coupled oscillators are studied. It can be seen from figures 2.7 and 2.8 that in the region of stability of the synchronous solution, the network shows less pattern of activity and the FC tends to be similar to SC. Conversely, if synchronous solution trends to be stable in the parameter space, the FC does not resemble the underlying SC. In figure 2.23 high values of the similarity were determined in the analytically derived parameter regions that correspond to pairwise synchronisability of local dynamics. On the other hand, low values of the similarity were determined in parameter regions that correspond to instability of pairwise synchrony.

A small amount of noise was added to the model. When the level of noise was increased slightly and decreased, noise had minimal effect on the results. Otherwise, when the amount of noise was too high, the level of synchrony fell. Furthermore, longer time series should be simulated in order to obtain successful statistical results of the process. The disadvantage of this approach is that it takes too much time and memory in the computational simulation.

This study has found that there are two types of measurement of FC: correlation and mean phase coherence. In general, the similarities between FC and SC can be studied using both measures. When correlation is used, the similarity measured by Pearson correlation is less than the similarity measured by the mean phase correlation in figure 2.7,

especially the eye-shaped region. Mean phase coherence is an effective method for the calculation of FC since the output of the Wilson-Cowan model is usually closer to local field potential. In addition to this, we can measure similarity by using the Spearman correlation which is a measure of the strength of association between two variables [51].

The model choice is important in this study. However, to extend this study, more complicated and realistic models e.g. the Liley *et al*. model would allow us to investigate more extensively the FC patterns and find how they change in brain diseases such as migraine and epilepsy.

Chapter 3

Neuroimaging and The Haemodynamic Response Model

3.1 The Haemodynamic Model

A model is necessary to see how the changes in blood affect the signal measured in fMRI. The haemodynamic response model presents the conncection between the blood flow, the volume, the oxygenation level and the neural activity in the localised area. Buxton *et al*. introduced the Balloon model for the first time in 1998 [11]. In 2000, Friston et al. developed the Balloon model to include the BOLD signal [38]. It is a input-state-output model that defines blood vessels in the brain as elastic balloons which can be pumped. In the brain the oxygen consumption increases because of a rise in neuronal activity. Then, the organism increases the blood inflow to brain vessels in order to get more oxygen. If the rate of inflow is larger than outflow, the balloon is pumped.

The haemodynamic model comprises of nonlinear differential equations. The equations of model are from [38]

$$\dot{s} = \epsilon u - \frac{s}{\tau_s} - \frac{f_{in} - 1}{\tau_f}$$

$$\dot{f}_{in} = s$$

$$\tau_0 \dot{v} = f_{in} - f_{out} \tag{3.1.1}$$

$$\tau_0 \dot{q} = f_{in} \frac{1 - (1 - E_0)^{\frac{1}{f_{in}}}}{E_0} - f_{out} \frac{q}{v}$$

where $f_{out} = v^{\frac{1}{\alpha}}$.

This model describes the relation between synaptic activity and BOLD signal. This model is the combination of the Balloon model [11] and a linear dynamical model of the alteration in regional cerebral blood blow generated by neural activity [38]. A diagram of the model is shown in figure 3.1. The state variables of the haemodynamic models indicate the change in normalised flow signal s, the change in normalised blood flow f, the change in volume v, and the change in deoxyhaemoglobin q. The constant E_0 denotes the resting oxygen extraction fraction, the constant τ_0 illustrates the mean transit time, and α represents the stiffness exponent. Furthermore, ϵ denotes the efficacy, τ_s is the time constant for signal decay, and τ_f is the time constant for autoregulatory feedback from blood flow [38].

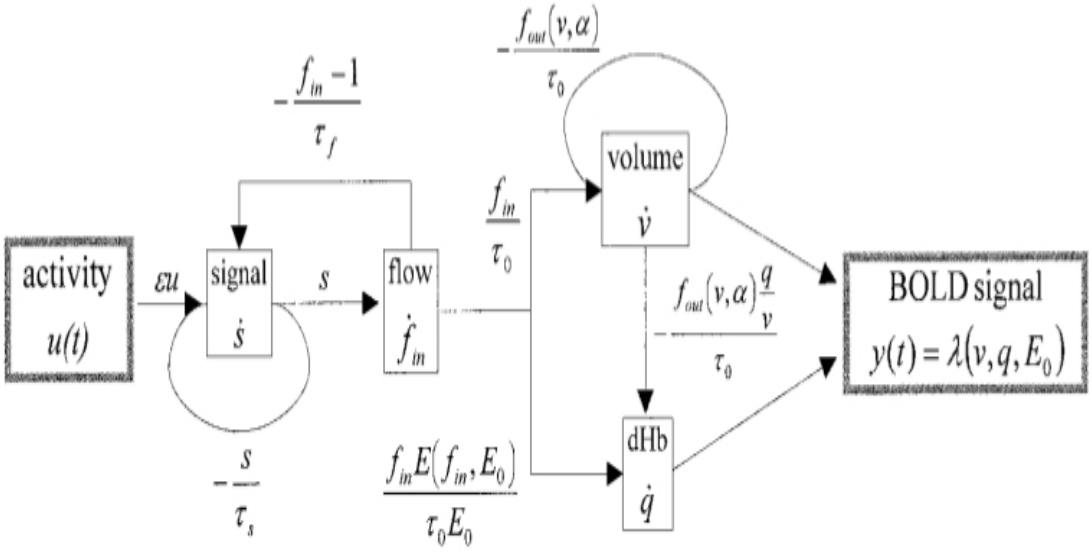

Figure 3.1: The architecture of the haemodynamic model. Input of the model is activity *u(t)*, and output is BOLD signal *y(t)*. State variables are s, f_{in}, v, q. This figure is taken from [38].

Moreover, the model of haemodynamic response function is extended by Rosa *et al* [95]. The equations of the model are taken from [95]. While the haemodynamics response model equations [95] are the same as the model in [38], the value of parameters

are different.

$$\dot{s} = \epsilon u - k_s s - k_f f(b_f - 1)$$

$$\dot{b_f} = s$$

$$\dot{v} = \frac{1}{\tau}\left(b_f - v^{\frac{1}{\alpha}}\right) \tag{3.1.2}$$

$$\dot{q} = \frac{1}{\tau}\left(b_f \frac{1-(1-E_0)^{\frac{1}{b_f}}}{E_0} - v^{\left(\frac{1}{\alpha}-1\right)q}\right)$$

All variables are described in normalised form with their resting values. The non-linear dynamic system is denoted by s, b_f, v and q. The variable s is the vasodilatatory and activity dependent signal which rises the normalised blood flow b_f. The non-linear function of normalised blood venous volume is denoted by v, the normalised veins deoxyhaemoglobin voxel content is shown by q. The constant E_0 defines the resting net oxygen extraction fraction by capillary bed. The constant ϵ is the efficacy, $\frac{1}{k_s}$ and $\frac{1}{k_f}$ are time constants. The mean transit time is denoted by τ, and a stiffness exponent is symbolised by α [95].

3.2 BOLD Signal

The Blood Oxygen Level Dependent signal is based on the variations of deoxyhemoglobin concentration and blood volume. Changes in neural activity results in changes in metabolism and cerebral blood flow. These cause alterations in deoxyhemoglobin which affects the BOLD signal [118]. BOLD represents the changes of the magnetic susceptibility of the blood and the generation of magnetic field gradients around the vessels, so magnetic field gradients make changes in the MR signal [85]. When neural activity increases, it leads to a rise in metabolic demand for oxygen and nutrients. Oxygen is taken from the blood. Haemoglobin in the oxygen is paramagnetic. It is detected by

MRI methods.

Functional Magnetic Resonance Imaging is an important method to measure the activity of the brain. It gives information about brain functions. The level of oxygen consumption in the brain through the BOLD signal modifies the contrast agent in fMRI. BOLD indirectly measures the stimulus which is required not only to describe a region of the brain but also to check similarities and dissimilarities in different regions [124].

The BOLD signal, that is dependant on v, q and E_0, is given by the equations

$$BOLD = V_0[k_1(1-q) + k_2\left(1 - \frac{q}{v}\right) + k_3(1-v)] \tag{3.2.1}$$

where the constants $k_1 = 7E_0$, $k_2 = 2$, $k_3 = 2E_0 - 0.2$. Moreover, V_0 describes the blood volume fraction at rest [35, 95].

The BOLD signal from Rosa *et al.*$'s$ paper is shown in figure 3.2.

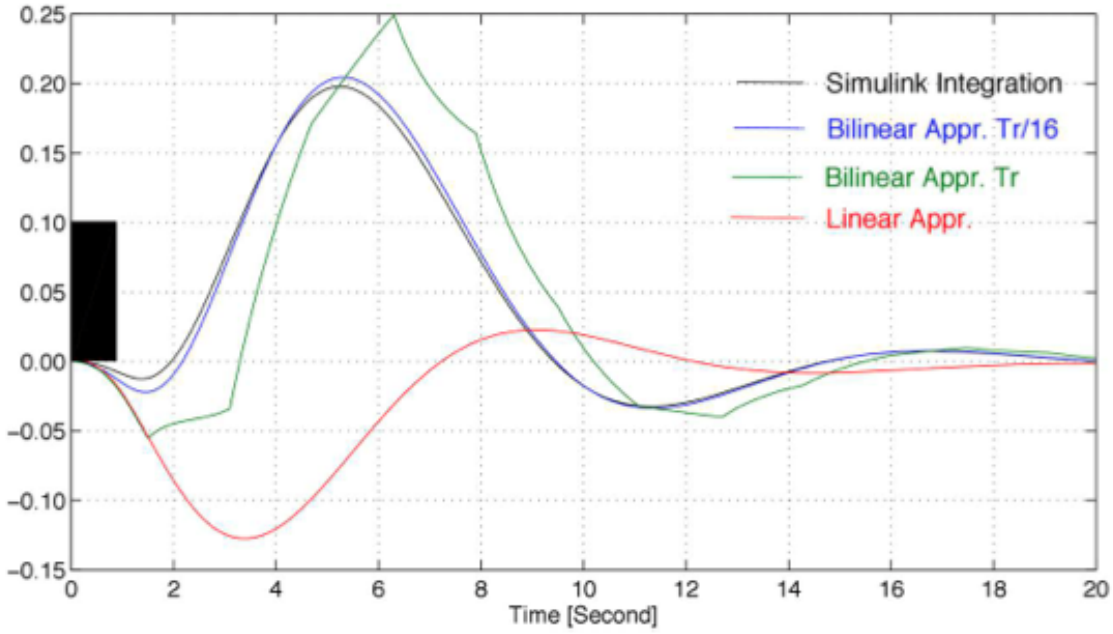

Figure 3.2: The responses of the haemodynamic response model to a rectangular input signal. It is taken from [95].

Parameters of the haemodynamic response function model are $\epsilon = 0.065$, $k_s = 0.550$, $k_f = 0.410$, $\tau = 1.280$, $\alpha = 0.880$, $E_0 = 0.920$, and $V_0 = 4.88$ [95]. We used the same parameters as the Rosa *et al.*'s paper and found a different response to the same input signal as illustrated in figure 3.3.

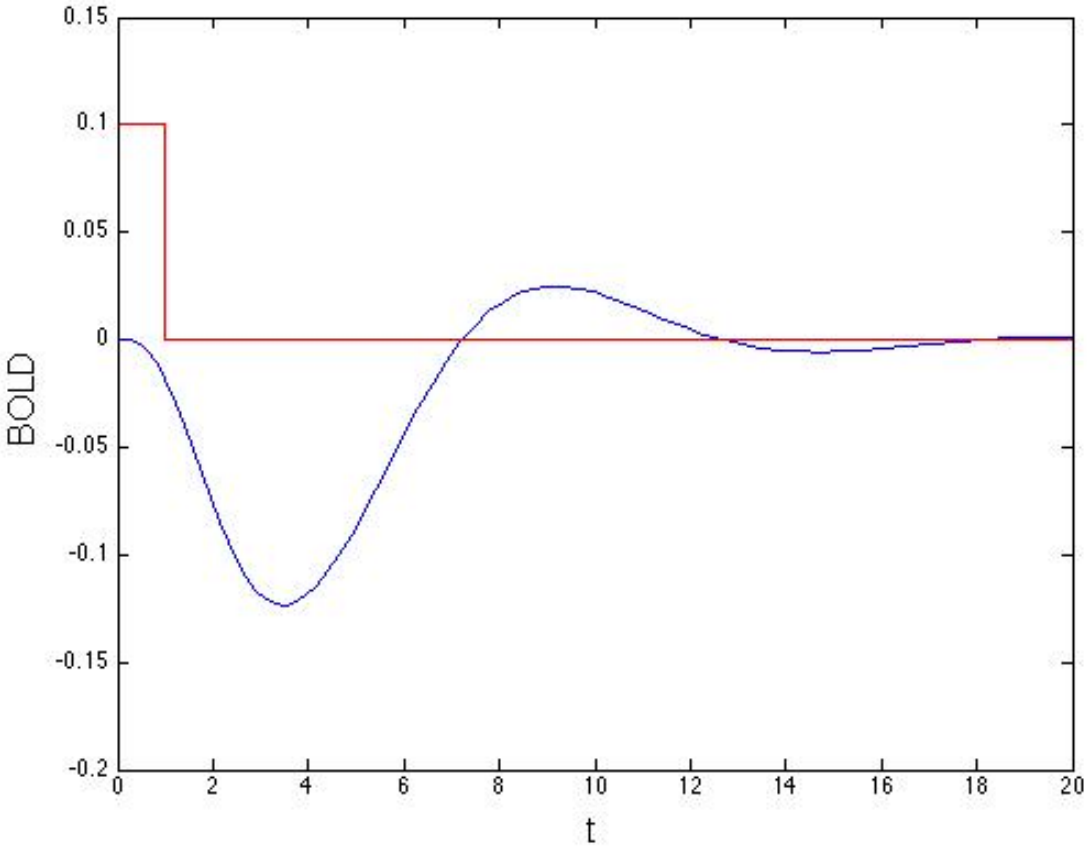

Figure 3.3: Our result as BOLD signal and model taken from [95].

Although we used the same values of parameters, the BOLD response from our result and the Rosa *et al.*'s result were not identical. The simulink integration which is black line in Rosa *et al.*'s paper is produced by using nonlinear dynamic system shown in equation (3.1.2). The BOLD signal in our result and simulink integration should be same, however this is not the case. Paulo Rosa mentioned in our personal communication via e-mail that there is a mistake in the generation of figure 3.2. We therefore decided to use Friston's extended Balloon model [38] and parameters in their paper. The parameters of haemodynamic model [38] are $\epsilon = 0.5$, $\tau_s = 0.8$, $\tau_f = 0.4$, $\tau = 1$,

$\alpha = 0.2$, $E_0 = 0.8$, and $V_0 = 0.02$.

The BOLD signal produced from [38] is shown in figure 3.4.

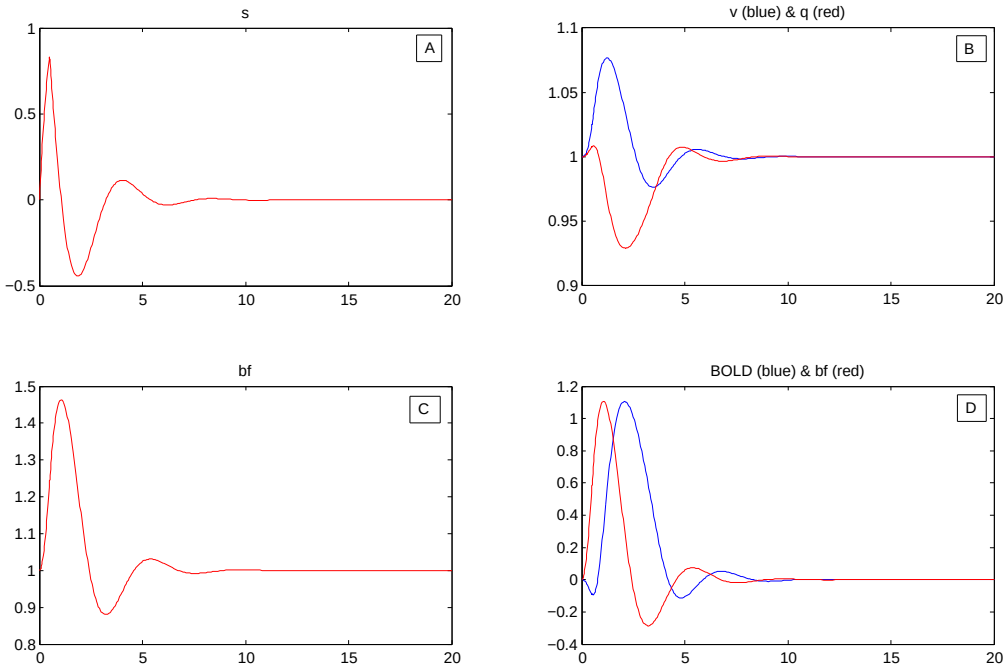

Figure 3.4: The behaviours of the haemodynamic model. Figure A denotes the flow signal which induces a rise in blood flow. Figure B shows the alteration in normalised volume and normalised deoxyhemoglobin concentration. Figure C shows the changes in normalised blood flow. The BOLD signal (blue line) and blood flow that normalised to the same maximum value as the BOLD signal (red line) are plotted on figure D.

The upper left figure with solid trapezoidal line in figure 3.4 shows the volume. The blood level rises to the maximum value, and there are some changes in volume like a balloon. The deoxyhemoglobin concentration increases moderately, then drops sharply, and finally returns to the resting level as it is seen in figure B with red line. There is an increase in the level of deoxyhemoglobin and a decrease the volume level in the first seconds, this causes an early dip in BOLD signal. Then, while there is a decrease in the level of deoxyhemoglobin, the volume level reaches a certain value. Therefore, it is followed by a positive peak in BOLD signal. As it is shown in the figure 3.4 the BOLD signal seems as the inverted version of deoxyhemoglobin concentration. Moreover, the

BOLD signal lags the blood flow by about a second [38].

The typical dynamics of BOLD signals include a signal reduction (initial dip), a positive response after a haemodynamic delay and then a signal reduction (poststimulus undershoot) [11]. It is assumed that the initial phase results from an increase in deoxyhemoglobin. A rise in metabolism leads to this increase before the hemodynamic response kicks in. Moreover, the initial dip directly corresponds to the metabolic response and then neural activity demonstrates immediate interest in MR bands, since the increase in deoxyhemoglobin could cause a decrease in the MR signals. Thus, the initial phase in fMRI signal is called the initial dip [56]. The initial dip has lower attitude than BOLD signal. The positive response arises from the vasodilation of the arterioles. It causes an increase in cerebral blood flow. Then, increased blood volume with baseline flow decreases the MR signal. This results in undershoot. Moreover, the changes in peak signal depend on the brain area, the parameters of task, the voxel size and field strength [67].

The determinants of the BOLD signal are the neural response to a stimulus. The relationship between neural activity and haemodynamic response that called neurovascular coupling, the haemodynamic response, and the response determined by a fMRI. The haemodynamic response model can be coupled to the neural activity to derive the spatiotemporal haemodynamic response [29]. The coupling between neural activity and the neurovascular response has an important role in order to detect the amplitude and spatial resolution of the BOLD signal [74]. Overall, determination of neural signals form the BOLD signal is a realistic possibility if there a linear relationship between neural activity and BOLD signal [74].

3.3 The Haemodynamic Response Model Coupled to The Wilson-Cowan Model

The Wilson-Cowan model [119, 120] shows excitatory and inhibitory features of the neural populations connected to each other. The variables x and y symbolise the mean firing rates.

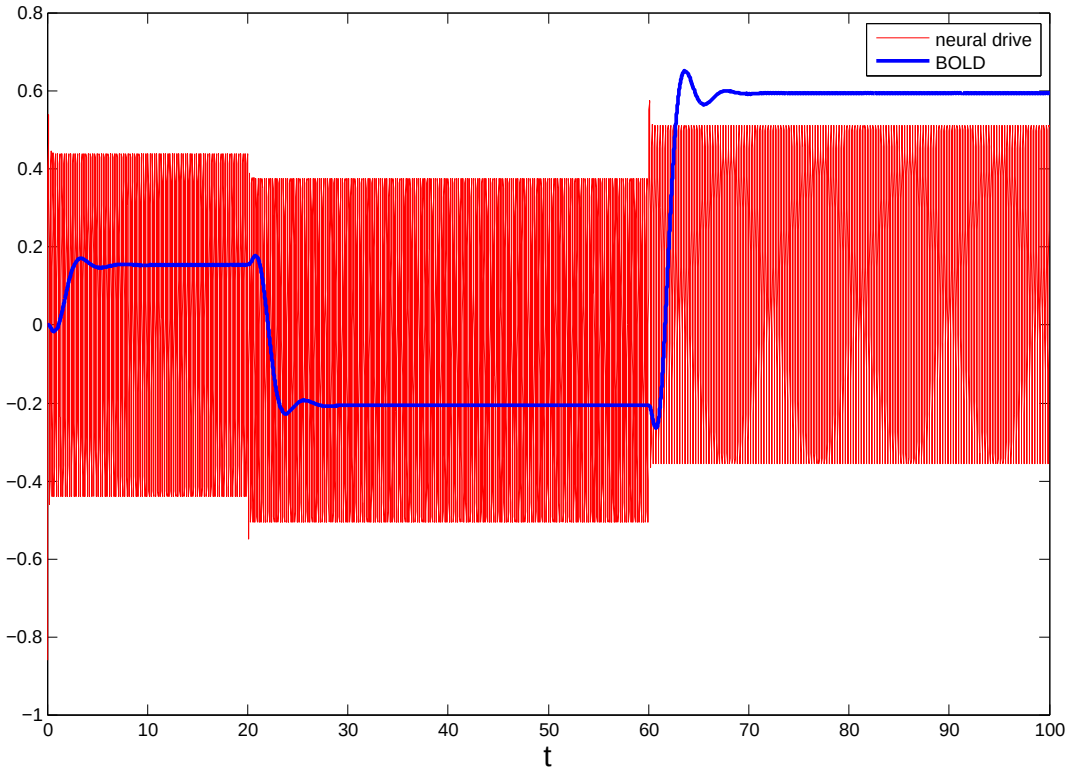

Figure 3.5: The BOLD signal which is produced from the haemodynamic model coupled to the Wilson-Cowan model. Parameters of the Wilson-Cowan model are $c_1 = 10$, $c_2 = 10$, $c_3 = 10$, $c_4 = -2$, $P = 1$ and $Q = -6$.

Normally after the neural activity increases, blood flow increases, so deoxyhemoglobin concentration decreases. As is typical for the BOLD signal, first there is a signal reduction, then a signal increase, and finally a signal decrease known as the post-stimulus undershoot.

It can be predicted from figure 3.5 that the BOLD signal does not reflect perfectly the neural activity since it is slow, however it measures a combination of membrane potentials and action potentials [74]. Blue line represents BOLD signal and red line is the neural drive from excitatory.

Neural activity was chosen as the first component (excitatory neuron) of the Wilson-Cowan model. When neural activity was increased, in a few seconds there was a decrease in BOLD signal until it reached to the early initial dip, then it started to increase

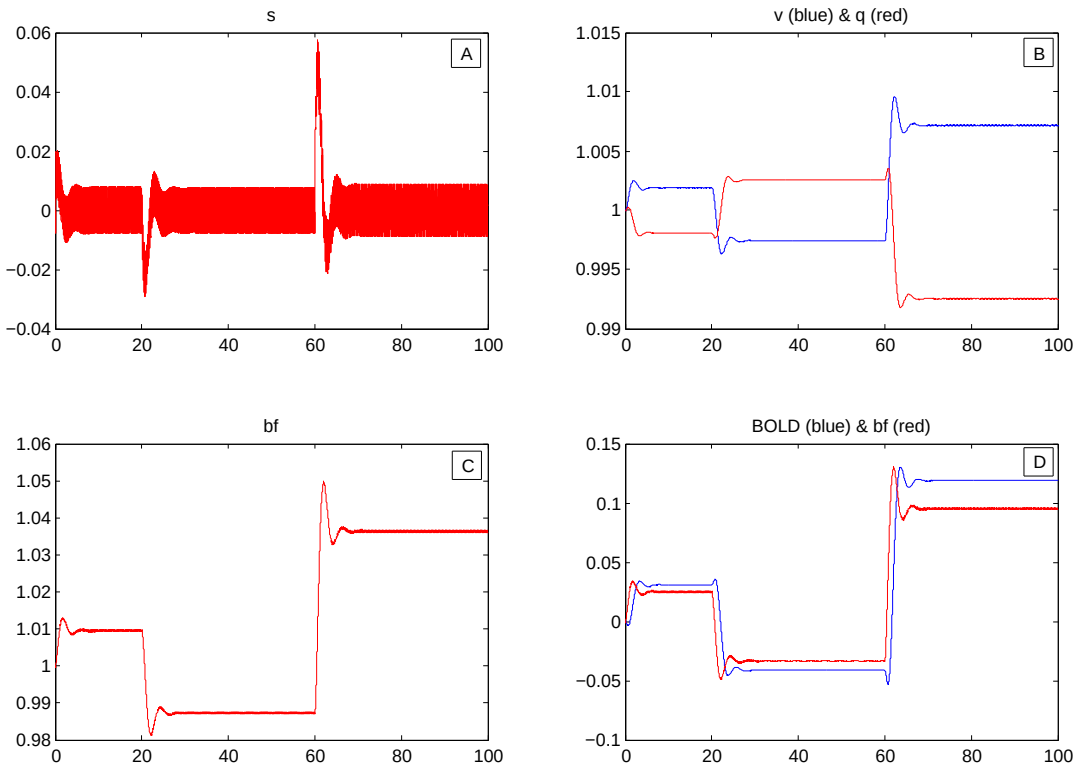

Figure 3.6: The figure shows the dynamics of the haemodynamic model coupling with the Wilson-Cowan model. Parameters of the Wilson-Cowan model are $c_1 = 10$, $c_2 = 10$, $c_3 = 10$, $c_4 = -2$, $P = 1$ and $Q = -6$. Figure A shows the flow and figure B denotes the changes in normalised volume and normalised deoxyhemoglobin concentration. Figure C shows the changes in normalised blood flow. The BOLD signal (blue line) and blood flow that normalised to the same maximum value as the BOLD signal (red line) are plotted on figure D.

and then had the poststimulus undershoot. On the contrary, when there was a decrease in neural activity, BOLD signal had an increase for a few seconds, then it decreased.

3.4 The Haemodynamic Response Model Coupled to The Liley Model

The Liley model, as a macroscopic model, denotes the mean field dynamics of large neuron populations by using two-dimensional nonlinear ordinary differential equations. The Liley model is able to reproduce the major properties of sponteneous human EEG spectrum with admissible parameters. As we mentioned earlier, the potential difference between the electrodes, which rested on the scalp, is measured by the EEG.

The frequency range of the measured activity changes between 1-40 Hz. This activity is split into parts. Each part has a specific spatial distribution over the scalp. Also, each is essential to a particular brain region. One part is known as the alpha band with a frequency of 8-13 Hz and arises by closing the eyes and relaxing. The production of an autonomous limit cycle and chaotic oscillatory activity in this band, is relatively straightforward [101].

The Liley model is spatially coarse-grained over roughly the extent of a cortical macrocoloum because it is convenient because of the structure of EEG data [72]. The cortical activity occurs within and between two different macrocolums which contain excitatory and inhibitory neural populations. The equations of the Liley model are

$$\dot{E} = (E_R - E + W_{EE} * g_{EE} * (E_{Eeq} - E) + W_{EI} * g_{EI} * (E_{Ieq} - E)/\tau_E \tag{3.4.1}$$

$$\dot{I} = (I_R - I + W_{II} * g_{II} * (I_{Ieq} - I) + W_{IE} * g_{IE} * (I_{Eeq} - I))/\tau_I \tag{3.4.2}$$

$$\dot{x}_{EE} = a_{EE} * (-x_{EE} + f(E) + P_{EE}) \tag{3.4.3}$$

$$\dot{g}_{EE} = a_{EE} * (-g_{EE} + x_{EE}) \tag{3.4.4}$$

$$\dot{x}_{II} = a_{II} * (-x_{II} + r * (k * f(I) + P_{II})) \tag{3.4.5}$$

$$\dot{g}_{II} = a_{II} * (-g_{II} + x_{II}) \tag{3.4.6}$$

$$\dot{x}_{IE} = a_{IE} * (-x_{IE} + (f(E) + P_{IE})) \tag{3.4.7}$$

$$\dot{g}_{IE} = a_{IE} * (-g_{IE} + x_{IE}) \tag{3.4.8}$$

$$\dot{x}_{EI} = a_{EI} * (-x_{EI} + r * (f(I) + P_{EI})) \tag{3.4.9}$$

$$\dot{g}_{EI} = a_{EI} * (-g_{EI} + x_{EI}) \tag{3.4.10}$$

The functions $f(E)$ and $f(I)$ convert the mean membrane potential of the neuron populations to an equivalent mean firing rate, and can be written

$$f(x) = 1/(1 + e^{-\beta_x * (x - \mu_x)}) \tag{3.4.11}$$

where $x = E, I$.

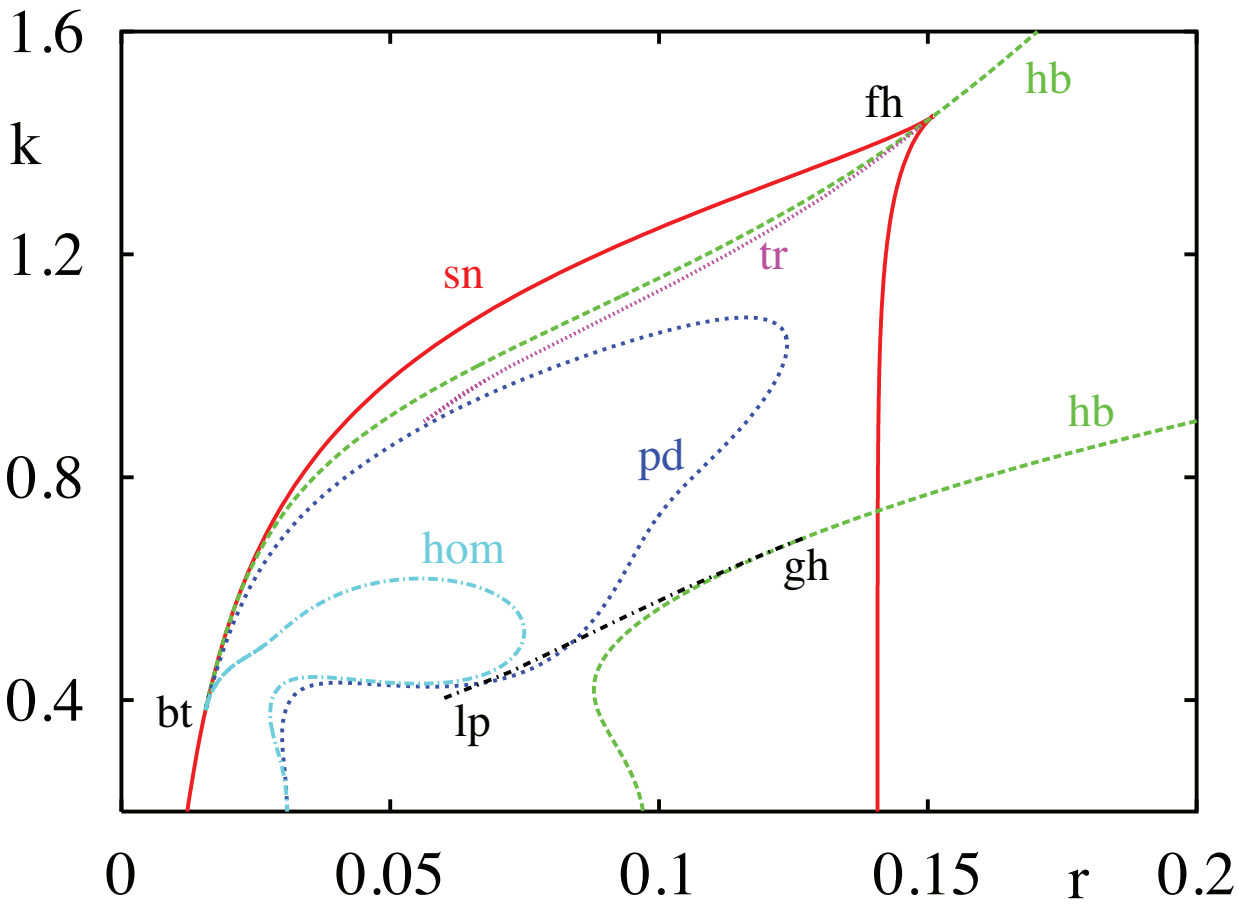

Figure 3.7: Bifurcations of the stationary state in the (r, k) plane. Parameters as in Table 3.1. Solid (red) lines correspond to a saddle-node bifurcation and dashed (green) to a Hopf bifurcation. *bt* denotes a Bogdanov-Takes point, *gh* denotes a generalised Hopf where the bifurcation switches from supercritical to subcritical. A fold of limit-cycles is denoted by *lp*, and a fold-Hopf point and a homoclinic orbit is represented by *fh*.

Two new scale parameters, r and k are introduced $\overline{W}_{aI} \to rW_{aI}$ and $\overline{W}_{II} \to kW_{II}$ where $a \in E, I$. We produce bifurcation points for the stationary states which are shown in figure 3.7.

Table 3.1: Parameters of the Liley Model

Description	Symbol	Value	Unit
excitatory input to excitatory neuron	P_{EE}	0.0045	ms^{-1}
excitatory input to inhibitory neuron	P_{EI}	0	ms^{-1}
inhibitory input to inhibitory neuron	P_{II}	0	ms^{-1}
inhibitory input to excitatory neuron	P_{IE}	0.01	ms^{-1}
postsynaptic potential peak amplitudes	a_{EE}	0.1226	ms^{-1}
	a_{EI}	0.2931	ms^{-1}
	a_{II}	0.1114	ms^{-1}
	a_{IE}	0.9825	ms^{-1}
weights	W_{EE}	41.0199	
	W_{EI}	242.9361	
	W_{II}	79.3577	
	W_{IE}	17.9295	
leak reversal potentials	E_R	-72.293	mV
	I_R	-67.261	mV
reversal potentials	E_{Eeq}	7.2583	mV
	E_{Ieq}	-80.697	mV
	I_{Ieq}	-76.674	mV
	I_{Eeq}	9.8357	mV
firing rate threshold	μ_E	-44.522	
	μ_I	-43.086	
firing rate steepness	β_E	0.3005	
	β_I	0.4771	
relaxation time constants	τ_E	32.209	
	τ_I	92.260	
scale parameters	r	1	
	k	1	

Table 3.1 shows the definitions of the symbols and model constants for the Liley model.

The mean membrane potentials in the excitatory and inhibitory population are $E(0) = -61.194$, $I(0) = -55.572$ respectively. Moreover, initial conditions of remained parameters are assumed to be 1.

The haemodynamic model is coupled to the Liley model and the BOLD signal is plotted as:

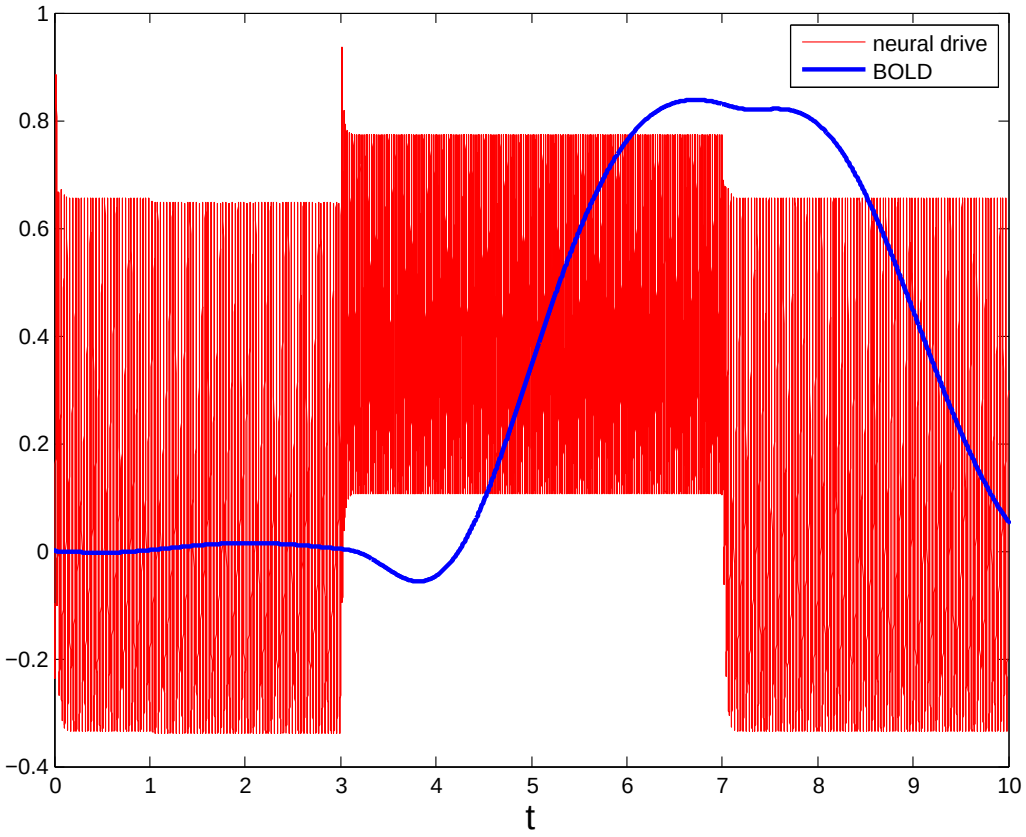

Figure 3.8: The BOLD signal which is produced from the haemodynamic model coupled to the Liley model with given parameters. The Liley model tends to have the EEG alpha rhythm which is time series as red lines and fMRI-BOLD response which is blue line with given additional stimulus excitatory input.

It can be seen from the data in figure 3.8 that an increase in neural activity causes an increases in signal, blood flow and therefore volume. When neural activity does not change, there is no great effect on BOLD signal. When neural activity increases, the BOLD signal has a slightly decrease for few seconds, then overshoots. Hence, the Liley model is too fast in comparison to the BOLD signal.

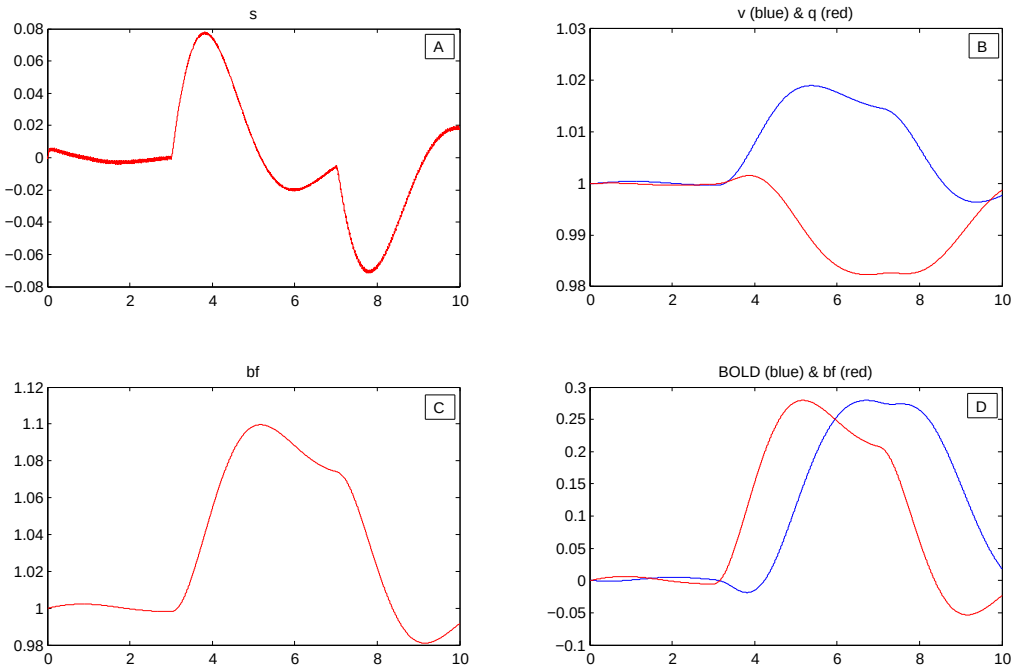

Figure 3.9: The dynamics of the haemodynamic model coupling with the Liley model with given parameters. The flow is shown in figure A and the changes in normalised volume and normalised deoxyhemoglobin concentration are denoted in figure B. Figure C shows the changes in normalised blood flow. The BOLD signal (blue line) and blood flow that normalised to the same maximum value as the BOLD signal (red line) are plotted on figure D.

3.5 Discussion and Conclusion

In present chapter, we investigate the BOLD signal from the haemodynamic model, the haemodynamic response model coupled to Wilson-Cowan model and the Liley model. The normalised neural activities were taken from the first (excitatory) components of the Wilson-Cowan and the Liley model, respectively. While the neural activity was fast, the dynamics of BOLD signal was slow as seen in figure 3.5 and 3.8.

The nature time scale of the Wilson-Cowan model is 10 oscillations per second. On the other hand, the oscillators of the Liley model has alpha rhythm and its dynamic is fast. While it uses second as a time unit, the time unit of the haemodynamic response model is miliseconds. When these two models are coupled, the same unit is requirement. Therefore, the time unit of the Liley model was transformed to miliseconds.

The dynamics of BOLD signal includes an initial dip, a positive response and a post-stimulus undershoot. The initial dip is weaker than poststimulus undershoot. In addition to this, in real BOLD signals there is no initial dip at all times [7].

The decreased neural activity leads to decrease the BOLD signal [75]. The BOLD signal does not fully reflect the neural activity because of having slow dynamic. Additionally, BOLD signal produced from coupling with the Wilson-Cowan model can be used to calculation of FC for the future work. Then, the relationship between the FC and SC can be investigated highlighting the BOLD signal.

Chapter 4

Discussion and Conclusion

In this chapter, the main findings with regard to the research questions are summarised and general conclusions are described. Furthermore, we consider the strengths and limitations of this thesis. It concludes with an exploration of possible future directions for the research.

A general introduction of the relevant neurobiology was first presented in Chapter 1. Neuroimaging has a major role in research and clinical diagnosis. The well-known neuroimaging methods are EEG, MEG, MRI and fMRI. While EEG records electrical fields in the brain, the MEG records the magnetic fields in the brain. Both methods measure neural activity and provide a picture of dynamic relationship between brain networks at rest and during tasks. The EEG and MEG signals directly reflect current flows which are generated by neurons. Moreover, MRI is used to image the structure of the brain, while fMRI is used to image the metabolic functions of the brain. MRI helps during diagnosis, but fMRI is useful for experiments and research purposes. Therefore, neuroimaging methods are important for understanding brain structure and function.

The importance of mathematical models and their very brief history were mentioned in Chapter 1. Two neural mass models, the Jansen-Rit and Liley models, were described with the equations. The oscillations and bifurcation diagram of the Liley model were shown. Furthermore, the Liley model was coupled with the haemodynamic model, and BOLD signal, as an output, is plotted using MATLAB.

The link between functional and structural connectivity was explained by using the Wilson-Cowan model which is the simplest neural mass model. After the definitions of FC and SC, FC was calculated using the Pearson and Spearman correlations, while SC was calculated with data from CoComac database. Then, the Wilson-Cowan model was analysed and its dynamics shown on the bifurcation diagram. Moreover, the similarity between FC and SC was measured by Hilbert transform and shown in figure 2.7 and 2.8. As a result, there is no significant difference between the Pearson and Spearman method for measuring the similarity of FC and SC.

In the study presented in Chapter 2, phase response curves were calculated by XPP, MATLAB GUI and the adjoint method which is equivalent to the method in XPP. They are crucial for understanding synchronisation properties of weakly coupled oscillators and for understanding a real biological oscillator. They are also used for calculation of phase interaction functions. These functions play an important role in the identification of the stability of the fully synchronised solution which is directly related to the main focus of this chapter. If the sign of $H'(0)$ is positive, it corresponds to stability of synchrony. In contrast, if the sign of $H'(0)$ is negative, it corresponds to instability of synchrony. As it is seen in figure 2.23, the synchronous solution is stable in the parameter regions, so the FC becomes similar to the SC. Conversely, pairwise connected networks present more activity in the regions of instability of synchronous solutions.

The Wilson-Cowan model was chosen because of its simplicity. If more complicated and biologically realistic models can be used, more plausible results can be obtained. These results change according to physiological variables because of brain diseases, such as Alzheimer, migraine and schizophrenia, or other factors of brain function. Based on the results of this research, it is recommended that biologically realistic levels of noise and delays should be applied in order to model real world phenomena in more detail. Furthermore, future work can be done for more realistic models with experimentally-valid variables chosen from neuroimaging methods. This model can be the Liley model, as it is used to model the human EEG alpha rhythm.

A general overview of neuroimaging techniques was given in Chapter 3. In addition

to this, the haemodynamic model and its output, known as BOLD signal were presented. Then, the haemodynamic model is coupled with the Wilson-Cowan model and the Liley model. The typical dynamics of BOLD signals contain an initial dip, a positive response after a haemodynamic delay and then a poststimulus undershoot [11].

There are several lines of research arising from this work which should be pursued. Initially, research can be done in the analysis of cluster states and the role of delays. Synchronisation in all brain subunites is not expected. Synchrony can be seen only in some part of the brain. In addition to this, in biological processes physical delays can be found. Delay equations are suitable for a better description of the plausible phenomenon. This idea is more relevant to the real world. The other challenge is to explain the role of delays in the model.

$$\dot{x_i} = -x_i + P + c_1 f(x_i) - c_2 f(y_i) + \epsilon \sum_j w_{ij} f(x_j(t - \tau_{ij}))$$

Another possibility would be to consider the weak coupling theory in a different way, so each neural oscillator must be near a bifurcation to make a nontrivial contribution to the entire network dynamics. Moreover, the strong coupling theory can be investigated and applied to our system.

Data produced in the study is from macaque monkey brain in CoComac database. This study can be extended to the human brain by the help of Allen Brain Map. It can improve our understanding of schizophrenia, Alzheimer's disease, epilepsy and other diseases in the brain. As a future work, the 47×47 BOLD signals, which are produced by coupling Wilson-Cowan model, will be used for the calculation of FC instead of the output of the Wilson-Cowan model. We expect that BOLD signal will be quite flat, and it does not have too much structure. Therefore, we can illustrate that with more sophisticated model as the Liley model. Ever after SC will be produced by using data from macaque monkey as we calculated already. Then, the relationship between FC and SC will be investigated.

Finally, the studies [116], [91] and [27] can be helpful to make a plan for future work. Moreover, the study [12] explains the role of the structural connectivity in the large-

scale dynamics of the healthy and schizophrenic brain by using a computational model. If global coupling could be reached its normal level by using medicine or deep brain stimulation, there would be similarity between FC simulated with the model with structural connectomes from patients and FC from healthy people [12]. Therefore, the study can be extended by using medicine in patients with schizophrenia, and then compared FC in healthy people and patients with schizophrenia. Also, the gender and age group can be considered when measuring the SC and the FC.

Appendices

Appendix A

Appendix: Euler-Maruyama Method

It is named by Leonhard Euler and Gisiro Maruyama. SDEs are the differential equation systems which are influenced by random noise. They include random white noise that is the derivative of Brownian motion [30] or in other words, the Wiener process.

Moreover, while Euler method is used for ODEs, Euler-Maruyama method is used for SDEs. A typical equation of SDE is

$$dX_t = a(t, X_t)dt + b(t, X_t)dW_t \tag{A.0.1}$$

with $X_0 = x_0$ and on time inverval [0, T].

Notice that SDE is given in differential form, unlike the derivative form of an ODE. Since, many stochastic processes such as Brownian motion, are continuous but not differentiable [98].

For the above stochastic differential equation the scheme has the form

$$X_{n+1} = X_n + a(t_n, Xn)\delta t + b(t_n, X_n)\Delta W_n \tag{A.0.2}$$

where $\Delta W_n = W_{t_{n+1}} - W_n$ is Brownian motion.

In order to obtain this scheme the following approximations are used

$$\int_{t_n}^{t_{n+1}} b(s, X_s)\mathrm{d}W_s \approx b(t_n, X_n)\Delta W_n \tag{A.0.3}$$

$$\int_{t_n}^{t_{n+1}} a(s, X_s)\mathrm{d}s \approx a(t_n, X_n)\delta_t \tag{A.0.4}$$

Appendix B

An example: PRC of Hopf model

This is an example of the calculating PIF analytically and PRC analitically and numerically for Hopf model which is:

$$\dot{x} = \mu x - \omega y - x(x^2 + y^2) \tag{B.0.1}$$

$$\dot{y} = \omega x + \mu y - y(x^2 + y^2) \tag{B.0.2}$$

In polar coordinates $x = r\cos\theta, y = r\sin\theta$, we can write this as:

$$\dot{x} = \dot{r}\cos\theta - r\dot{\theta}\sin\theta \tag{B.0.3}$$

$$\dot{y} = \dot{r}\sin\theta + r\dot{\theta}\cos\theta \tag{B.0.4}$$

After calculation, we reach:

$$\dot{x}\dot{y} = (r\theta)^2 \sin^2\theta\cos^2\theta \tag{B.0.5}$$

$$r\dot{r} = x\dot{x} + y\dot{y} \qquad r^2\dot{\theta} = x\dot{y} - y\dot{x} \tag{B.0.6}$$

It can be written as:

$$\dot{r} = \frac{1}{r}(x\dot{x} + y\dot{y}) \quad \dot{\theta} = \frac{1}{r^2}(x\dot{y} - y\dot{x}) \tag{B.0.7}$$

When we write the value of $\dot{x}$ and $\dot{y}$ in their place in the equations, and this becomes

$$\dot{r} = \frac{1}{r}(x(\mu x - \omega y - x(x^2 + y^2)) + y(\omega x + \mu y - y(x^2 + y^2))) \tag{B.0.8}$$

$$\dot{r} = \frac{1}{r}(x^2 + y^2)(\mu - x^2 - y^2) \tag{B.0.9}$$

$$\dot{r} = r(\mu - r^2), \qquad \dot{\theta} = \omega \tag{B.0.10}$$

It can be seen from this that there is a supercritical Hopf bifurcation for $\mu > 0$ giving rise to a stable limit cycle of radius $\sqrt{\mu}$ and frequency $\omega = 1/T$. The limit cycle can be formulated as:

$$(x, y) = \sqrt{\mu}(\cos \omega t, \sin \omega t) \tag{B.0.11}$$

Description of the normalisation condition $K.F = 1/T$ where $K = (k_1, k_2)$ and $r = \sqrt{\mu}$,

$$k_1 \dot{x} + k_2 \dot{y} = \frac{1}{T} \tag{B.0.12}$$

$$k_1(\mu x - \omega y - x r^2) + k_2(\omega x + y - y r^2) = \omega \tag{B.0.13}$$

After calculation, result will be

$$-k_1 y + k_2 x = 1 \tag{B.0.14}$$

K is orthogonal to the isochrons at the limit cycle, because it is the gradient. Therefore, the conditions are

$$(x, y)(k_1, k_2) = 1 \tag{B.0.15}$$

$$k_1 x + k_2 y = 0 \tag{B.0.16}$$

This yields

$$(k_1, k_2) = \left(\frac{-y}{(x^2 + y^2)}, \frac{x}{(x^2 + y^2)} \right). \tag{B.0.17}$$

This can be written as the function of phase $\theta \in [0, 1)$ on the limit cycle:

$$(k_1, k_2) = \left(\frac{-\sin(2\pi\theta)}{\sqrt{\mu}}, \frac{\cos(2\pi\theta)}{\sqrt{\mu}} \right) \tag{B.0.18}$$

$$\tag{B.0.19}$$

After the calculations, firstly, we must compute a response or adjoint.

$$H(\theta) = \frac{1}{T} \int_0^T K(\psi) f(\psi + \theta T) d\psi \tag{B.0.20}$$

where $f = X_1 - X_2 = X(t_1 + \theta_1 T) - X(t + \theta_2 T)$.

$$H(\theta) = \frac{1}{T} \int_0^T K(\psi) \left[X(\psi) - X(\psi - \theta T) \right] d\psi \tag{B.0.21}$$

$$H(\theta) = \frac{1}{T} \int_0^T -\sin \frac{2\pi\psi}{\mu} \mu \left[\cos \frac{2\pi\psi}{T} - \cos \frac{2\pi(\psi + \theta T)}{T} \right] d\psi \tag{B.0.22}$$

$$H(\theta) = -\frac{1}{2} \sin 2\pi\theta \tag{B.0.23}$$

After following calculation, result obtained numerically in XPP is shown in figure B.1. It provides the same PRC with the analytically calculation.

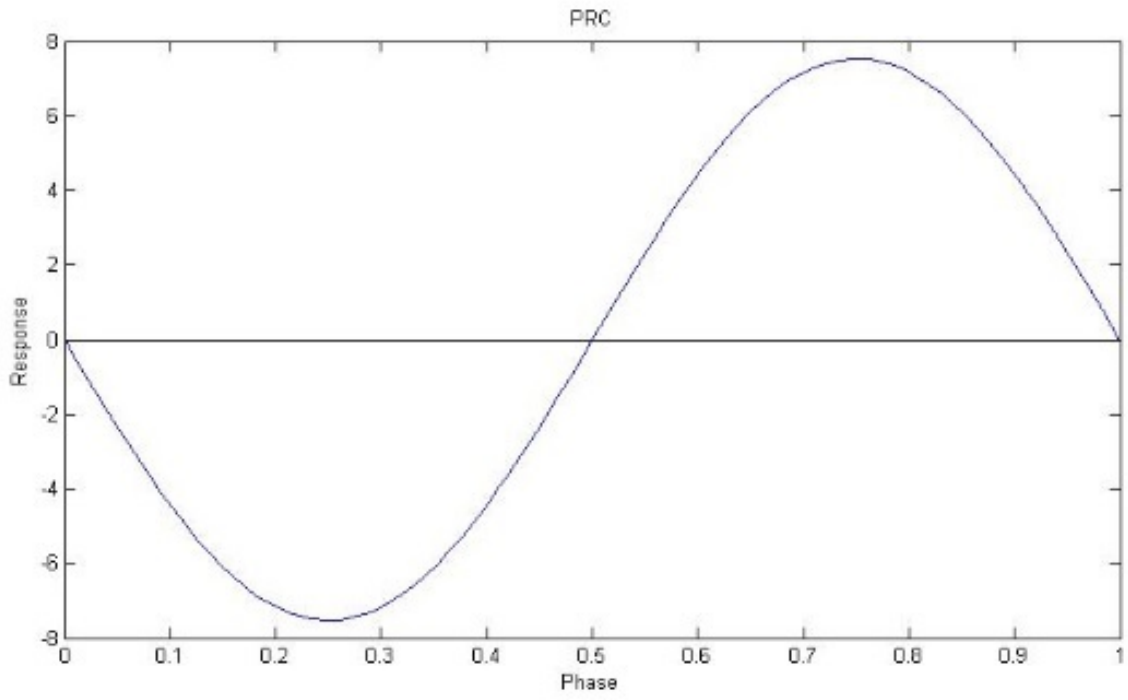

Figure B.1: The figure shows PRC of Hopf model in XPP.

Appendix C

Appendix: Codes

The codes calculate the simulation of Wilson-Cowan model, the functional connectivity, and similarity between FC and SC by using Pearson correlation.

```
function f=f(u,beta,h)
f=1.0./(1.0+exp(-beta.*(u-h)));

function WCmodel=WCmodel(X,P)
u=X(1:P.ncells);
v=X(P.ncells+1:2*P.ncells);
du=-u+f(P.c1*u-P.c2*v+P.P+P.epsilon*P.Weight*u,P.beta,P.h);
dv=-v+f(P.c3*u-P.c4*v+P.Q,P.beta,P.h);
WCmodel=[du;dv];

function [Y,T]=WCnetwork(P)
if (isfield(P,'Weight'))==1 Weight = P.Weight; else Weight=rand(50)
    >0.9; Weight(eye(50)==1)=0; end
Nnodes=size(P.Weight,1);
P.c1=10; P.c2=10; P.c3=10; P.c4=-2;
P.ncells = size(P.Weight,1); %number of the nodes
P.beta=1.0; %firing rate steepness
P.h=0.0; %firing rate threshold
P.epsilon=0.1;
P.gamma=0.1;
tmin=0;
```

```
tmax=1000;
%tmax=P.tmax;
tstep=0.1;
sigmadyn=0.001;
P.P=0;
P.Q=-6;
Nt=length(tmin:tstep:tmax);
Nvariables=2*Nnodes;
Y=zeros(Nt,Nvariables);
IC=rand(Nvariables,1);
IC=rand(Nvariables,1);
Y(1,:)=IC;
for it=1:Nt-1
dW=sigmadyn*sqrt(tstep)*rand(Nvariables,1);
Y(it+1,:)=(Y(it,:)'+tstep*WCmodel(Y(it,:)',P)+dW)';
end
T=tmin:tstep:tmax;

%Load Structural Connectivity data
load EEcorrect505;
%Normalization
P.Weight=EEcorrect505./repmat(sum(EEcorrect505,2),[1,size(EEcorrect505
    ,2)]);
N=size(P.Weight,1);
%Parameters
P.tmax=10000;
P.sigmadyn=0.01;
P.gamma=1;
P.epsilon=1;
tstep = 0.1;
tomit = 2000;
%define minimum and maximum vale of P,Q
rhoxmin = -6; % minimum P
rhoxmax = 6;
rhoymin = -12; % minimum Q
```

```
rhoymax = -0;
Nrhox = 4*12+1; % number of steps for P
Nrhoy = 4*12+1;

%define step size
rhoxstep=(rhoxmax-rhoxmin)/(Nrhox-1);
rhoystep=(rhoymax-rhoymin)/(Nrhoy-1);
%calculation of functional connectivity
FC=cell(Nrhox, Nrhoy);
for Irhoy=1:Nrhoy
    rhoy=rhoymin+(Irhoy-1)*rhoystep;
    for Irhox=1:Nrhox
    rhox=rhoxmin+(Irhox-1)*rhoxstep;
[Y,T] = WCnetwork(P);
        Y=Y(tomit+1:end,:);
        T=T(tomit+1:end);

% Hilbert transform
mts=mean(Y(:,1:size(P.Weight,1)),1);
A=Y(:,1:size(P.Weight,1))-repmat(mts,[size(Y(:,1:size(P.Weight,1)),1)
    ,1]);
hlbrt=angle(hilbert(A));
KK=size(A,2);

FC=zeros(KK,KK);
for i=1:KK
  for j=1:KK
phase=hlbrt(:,i)-hlbrt(:,j);
FC(i,j)=sqrt(mean(cos(phase)).^2 + mean(sin(phase)).^2);
  end
end

Put=P.Weight(triu(ones(size(P.Weight)),1)==1); % upper triangle
Fut=FC(triu(ones(size(FC)),1)==1);
```

```
Plt=P.Weight(tril(ones(size(P.Weight)),-1)==1); % lower triangle
Flt=FC(tril(ones(size(FC)),-1)==1);

Pnd=[Put;Plt]; % all non-diagonal entries
Fnd=[Fut;Flt];
%measure similarity between FC and SC by Pearson correlation
COR(Irhox,Irhoy)=corr(Pnd(:),Fnd(:),'type','Pearson');
Jak(Irhox,Irhoy) = sum((FC(:)==1) & (P.Weight(:)==1))/sum((FC(:)==1) |
    (P.Weight(:) ==1));
    end
end
```

These codes produce the orbits, PRCs with adjoint method and PIF by using these PRCs. Results are shown in Section 2.6. Orbits are found by running *Orbit_WC.m* code.

```
%Orbit_WC
function [Period t E I] = Orbit_WC(P,E0,I0,p,q)
total=2000;
%Evolve
options=[];
%initial data
X0=[E0;I0];
%evolve for large time
[t,X]=ode45(@WCRHS,[0 total],X0,options,P,p,q);
%use findpeaks to obtain period
[a,b] = findpeaks(X(:,1));
if ~isempty(b) & length(b) >=20      %20 crossings and then average
    Period = (t(b(end))-t(b(end-20)))/20;
else
    Period = 0;
    t=[];
    E=[];
    I=[];
    return
```

```
end
vmax=max(X(ceil(end/2):end,1));
vmin=min(X(ceil(end/2):end,1));
if Period < 0.01 | vmax-vmin < 0.01
    Period = 0;
    t=[];
    E=[];
    I=[];
    return
end
%run over one multiple of first guess for period to get better
   estimate
total=30*Period;
Y0=[X(end,1);X(end,2)];
options=['RelTol',1e-6,'AbsTol',1e-7];
N=1000;
dt=Period/N;
[t,X]=ode45(@WCRHS,[0:dt:total],X0,options,P,p,q);
[a,b] = findpeaks(X(:,1));
Period=(t(b(end))-t(b(end-5)))/5;
%one more time to get even mesh
N=1000;
dt=Period/N;
total=Period;
Y0=[X(end,1);X(end,2)];
[t,X]=ode45(@WCRHS,[0:dt:total],Y0,options,P,p,q);
E=X(:,1);
I=X(:,2);
end

function WCRHS=WCRHS(t,X,P,p,q)
E=X(1);
I=X(2);
WCRHS=[-E+f(P.c1*E-P.c2*I+p);-I+f(P.c3*E-P.c4*I+q)];
```

```
end

function fdash = fdash(z)
fdash=f(z)*(1-f(z));
end

function f = f(z)
f=1.0./(1+exp(-z));
end
```

The orbits produced from *Orbit WC . m* are used to calculate PRCs with adjoint method.

```
%PRC_WC
function [Period t E I u v] = PRC_WC(p,q,u0,v0,E0,I0)
%Wilson-Cowan parameters
P.c1=10;
P.c2=10;
P.c3=10;
P.c4=-2;

%Construct orbit - need to add a check for existence.
[Period t E I] = Orbit_WC(P,E0,I0,p,q);
if Period == 0
    u=[];
    v=[];
    return
else
%Evolve adjoint equation in backward time
total=40*Period;
dt=t(2)-t(1);
options=[];
%options=['RelTol',1e-6,'AbsTol',1e-7];
X0=[u0, v0];
[t,X]=ode45(@AdjointRHS,[0:dt:total],X0,options,P,E,I,p,q,Period);
```

```
%normalise over one period
t=t(end-length(E)+1:end);
X=X(end-length(E)+1:end,:);
u=X(:,1);
v=X(:,2);
u=flip(u);  %backward time
v=flip(v);  %backward time
%shift origin of time to zero
t=t-(total-Period);
%compute inner product of adjoint and vector field
Edot=-E+f(P.c1*E-P.c2*I+p);
Idot=-I+f(P.c3*E-P.c4*I+q);
inner=(u'*Edot+v'*Idot)*dt/Period;
u=u/inner;
v=v/inner;
end
end

function AdjointRHS=AdjointRHS(t,X,P,E,I,p,q,Period)
%backward time: t -> -t
u=X(1);
v=X(2);
%s is the vector of times for the orbit
N=length(E);
%backward time
t=mod(t,Period);
index=floor(t/Period*N)+1;
Eback=E(N+1-index);
Iback=I(N+1-index);
AdjointRHS=[(-1+P.c1*fdash(P.c1*Eback-P.c2*Iback+p))*u + P.c3*fdash(P.
    c3*Eback-P.c4*Iback+q)*v; -P.c2*fdash(P.c1*Eback-P.c2*Iback+p)*u
    +(-1-P.c4*fdash(P.c3*Eback-P.c4*Iback+q))*v];
end
```

PIFs are calculated by PRCs in *HdashPQ . m*.

```
%HdashPQ.m
function out = HdashPQ()
pmin=-4;
pmax=4;
qmin=-10;
qmax=-2;
N=200;
dp=(pmax-pmin)/N;
dq=(qmax-qmin)/N;
out=zeros(N+1,N+1);
u0=rand(1);
v0=rand(1);
E0=rand(1);
I0=rand(1);
for i=0:N
    q=qmax-i*dq;
    i
for j=0:N
    p=pmin+j*dp;
        [Period t E I u v] = PRC_WC(p,q,u0,v0,E0,I0);
        if Period ~= 0
            out(i+1,j+1)=Hdash(Period,E,u);
            u0=u(end);
            v0=v(end);
            E0=E(end);
            I0=I(end);
        end
    end
end

figure(1)
p=linspace(pmin,pmax,N+1);
```

```
q=linspace(qmin,qmax,N+1);
%cut errors
out(find(abs(out)>.1))=0
pcolor(p,q,flipud(out));shading interp;colorbar
end

function Hdash=Hdash(Period,E,u)
dt=Period/length(u);
udash=diff(u)/dt;
udash(end+1)=(u(1)-u(end))/dt;
Hdash=-udash'*f(E)*dt/Period;
end

function f = f(z)
f=1.0./(1+exp(-z));
end
```

These codes use to calculation of BOLD signal from the haemodynamic model from Rosa *et al.*'s [95] and Friston's [38] paper.

```
function dZ= BalMod(t,Z,Pb,tU,U);
%% extract s, f, v, and q from Z
s=Z(1);
f=Z(2);
v=Z(3);
q=Z(4);

%% extract current neural activity from U
Ucurrent = interp1(tU,U,t);

ds=Pb.e*Ucurrent-s*Pb.ks-(f-1)*Pb.kf; %signal generated by neuronal
    activity
df=s;  %the rate of change of normalised blood flow
```

```
dv=(1/Pb.t)*(f-(v^(1/Pb.alpha)));  %the rate of change of volume
dq=(1/Pb.t)*( (f*(1-(1-Pb.E0)^(1/f))/Pb.E0) - (v^(1/Pb.alpha-1))*q );
   %the delivery of deoxyhemoglobin

dZ=[ds; df; dv; dq];
end

%% Parameters of the Balloon model from Rosa's paper.
Pb.e=0.065;
Pb.ks=0.550;
Pb.kf=0.410;
Pb.t=1.280;
Pb.alpha=0.880;
Pb.E0=0.345; %0.920
Pb.V0=4.88;
Pb.k1=7*Pb.E0;
Pb.k2=2;
Pb.k3=2*Pb.E0-0.2;

%% Friston parameters
Pb.e=0.5;
Pb.ks=1.25;
Pb.kf=2.5;
Pb.t=1;
Pb.alpha=0.2;
Pb.E0=0.8;
Pb.V0=0.02;
Pb.k1=7*Pb.E0;
Pb.k2=2;
Pb.k3=2*Pb.E0-0.2;

%% specify tU and U, data on neural activity (e.g. from another
   simulation)
tU =linspace(0,20,2001);
%% Friston stimulus
```

```
U = 5*(tU>=0).*(tU<0.5);
%% initial values
x0=[0;1;1;1];
tint=[0,20];

%% structure for ordinary differential equation solver
options = odeset('RelTol',1e-9,'AbsTol',1e-9);
% it generates time courses for s (signal), v(blood volume), f(blood
    flow), q(deoxyhemoglobin)
b = ode45(@BalMod,tint,x0,options,Pb,tU,U);
%% extract q and v from l
v = b.y(3,:);
q = b.y(4,:);
%% calculate BOLD signal from q and v
BOLD=100*Pb.V0*(Pb.k1*(1-q)+Pb.k2*(1-q./v)+Pb.k3*(1-v));

%% plot the components and BOLD signal
figure(1)
clf
subplot(2,2,1)
plot(b.x,b.y(1,:),'r')
title('s')
subplot(2,2,2)
plot(b.x,v,'r-')
hold on
plot(b.x,q,'r:')
title('v (solid) & q (dash)')
subplot(2,2,3)
plot(b.x,b.y(2,:),'r')
title('bf')
subplot(2,2,4)
plot(b.x,BOLD,'b')
hold on
plot(b.x,(b.y(2,:)-1)*max(BOLD)/max(b.y(2,:)-1),'r')
```

```
title('BOLD (blue) & bf (red)')

figure(2)
clf
plot(b.x,BOLD*100)
%% plot the stimulus (normalised so it fits on same axis as BOLD)
hold on
plot(tU,U,'r')
xlabel('t','fontsize',16)
ylabel('BOLD','fontsize',16)
```

The codes calculate the BOLD from the haemodynamic model coupled to the Wilson-Cowan model.

```
function dy=WC(t,y,Pw);
dy=zeros(size(y));
P = (t<20)*Pw.P + (t>=60)*(t<100)*2*Pw.P;
%% extract E, I from Wilson Cowan Model
E=y(1);
I=y(2);

%% equations of the Wilson-Cowan model
dE=-E+1.0./(1+exp(-Pw.c1*E+Pw.c2*I-P));
dI=-I+1.0./(1+exp(-Pw.c3*E+Pw.c4*I-Pw.Q));
dy=20*[dE; dI]; %more oscillators
end

clear all
Pw.c1=10;
Pw.c2=10;
Pw.c3=10;
Pw.c4=-2;
Pw.P=1;
Pw.Q=-6;
```

```
tint=[0,100];

%% structure for ordinary differential equation solver
options = odeset('RelTol',1e-6,'AbsTol',1e-6);
% it generates time courses for s (signal), v(blood volume), f(blood
    flow), q(deoxyhemoglobin)
wc_sim= ode45(@WC, tint ,[0 ,0],options ,Pw);
E = wc_sim.y(1,:);
I = wc_sim.y(2,:);

figure(1)
plot(wc_sim.x,E,'b-x')
hold on
plot(wc_sim.x,I,'r')

%% Parameters of the Balloon model from Friston's paper.
Pb.e=0.5;
Pb.ks=1.25;
Pb.kf=2.5;
Pb.t=1;
Pb.alpha=0.2;
Pb.E0=0.8;
Pb.V0=0.02;
Pb.k1=7*Pb.E0;
Pb.k2=2;
Pb.k3=2*Pb.E0-0.2;
%% specify tU and U, data on neural activity (e.g. from another
    simulation)
tU = wc_sim.x;
U = wc_sim.y(1,:);
i_unstim = find(tU > 0.1 & tU < 3);
Umin_unstim = min(U(i_unstim));
Umax_unstim = max(U(i_unstim));
Umean_unstim = mean(U(i_unstim));
U=(U-Umean_unstim)/(Umax_unstim-Umin_unstim);
```

```
%% initial values
x0=[0;1;1;1];
tint=[0,max(tU)];

%% structure for ordinary differential equation solver
options = odeset('RelTol',1e-9,'AbsTol',1e-9);
% it generates time courses for s (signal), v(blood volume), f(blood
    flow), q(deoxyhemoglobin)
b = ode23(@BalMod,tint,[0,1,1,1],options,Pb,tU,U);
%% extract q and v from l
v = b.y(3,:);
q = b.y(4,:);

%% calculate BOLD signal from q and v
y=Pb.V0*(7*Pb.E0*(1-q)+2*(1-q./v)+(2*Pb.E0-0.02)*(1-v));

%% plot BOLD signal and activity
 figure(1)
 clf
plot(b.x,100*y,'b','linewidth',2)
%% plot the stimulus (normalised so it fits on same axis as BOLD)
hold on
plot(tU,U,'r')
xlabel('t','fontsize',16)
ylabel('BOLD','fontsize',16)
```

The codes calculate the BOLD from the haemodynamic model coupled to the Liley model.

```
function dy=liley(t,y,Pl);
dy=zeros(size(y));

PEE = (t<1000)*Pl.PEE + (t>=3000)*(t<7000)*200*Pl.PEE + (t>=7000)*Pl.
    PEE;
```

```
%% extract E, I, Iee, gee, Iii, gii, Iie, gie, Iei and gei from y
E=y(1);
I=y(2);
xEE=y(3);
gEE=y(4);
xII=y(5);
gII=y(6);
xIE=y(7);
gIE=y(8);
xEI=y(9);
gEI=y(10);

Pl.fE=1/(1.0+exp(-Pl.betaE*(E-Pl.mue)));
Pl.fI=1/(1.0+exp(-Pl.betaI*(I-Pl.mui)));
dE=(Pl.Er-E+Pl.WEE*gEE*(Pl.EEeq-E)+Pl.WEI*gEI*(Pl.EIeq-E))/Pl.taue;
dI=(Pl.Ir-I+Pl.WII*(Pl.IIeq-I)*gII+Pl.WIE*gIE*(Pl.IEeq-I))/Pl.taui;
dxEE=Pl.aEE*(-xEE+Pl.fE+PEE);
dgEE=Pl.aEE*(-gEE+xEE);
dxII=Pl.aII*(-xII+Pl.r*(Pl.k*Pl.fI+Pl.PII));
dgII=Pl.aII*(-gII+xII);
dxIE=Pl.aIE*(-xIE+(Pl.fE+Pl.PIE));
dgIE=Pl.aIE*(-gIE+xIE);
dxEI=Pl.aEI*(-xEI+Pl.r*(Pl.fI+Pl.PEI));
dgEI=Pl.aEI*(-gEI+xEI);

dy=[dE; dI; dxEE; dgEE; dxII; dgII; dxIE; dgIE; dxEI; dgEI];
end

Pl.r=1.0;
Pl.k=1.0;
Pl.PIE=0.01001269;
Pl.PEE=0.004559343;
Pl.PII=0;
Pl.PEI=0;
```

```
Pl.aEE=122.68/1000.0;
Pl.aEI=293.10/1000.0;
Pl.aII=111.40/1000.0;
Pl.aIE=982.51/1000.0;
Pl.WEE=41.0199;
Pl.WEI=242.9361;
Pl.WII=79.35771;
Pl.WIE=17.92958;
Pl.Er=-72.293;
Pl.Ir=-67.261;
Pl.EEeq=7.2583;
Pl.EIeq=-80.697;
Pl.IIeq=-76.674;
Pl.IEeq=9.8357;
Pl.mue=-44.522;
Pl.mui=-43.086;
Pl.betaE=0.3004618;
Pl.betaI=0.4770657;
Pl.taue=32.209;
Pl.taui=92.260;

x0=[-61.194;-55.572;1;1;1;1;1;1;1;1];
tint=[0,10000];

%% structure for ordinary differential equation solver
options = odeset('RelTol',1e-7,'AbsTol',1e-7);

% it generates time courses for s (signal), v(blood volume), f(blood
    flow), q(deoxyhemoglobin)
liley_sim = ode45(@liley,tint,x0,options,Pl);

E=liley_sim.y(1,:);
I=liley_sim.y(2,:);
xEE=liley_sim.y(3,:);
```

```
gEE=liley_sim.y(4,:);
xII=liley_sim.y(5,:);
gII=liley_sim.y(6,:);
xIE=liley_sim.y(7,:);
gIE=liley_sim.y(8,:);
xEI=liley_sim.y(9,:);
gEI=liley_sim.y(10,:);

%% Parameters of the Balloon model from Friston's paper.
Pb.e=0.5;
Pb.ks=1.25;
Pb.kf=2.5;
Pb.t=1;
Pb.alpha=0.2;
Pb.E0=0.8;
Pb.V0=0.02;
Pb.k1=7*Pb.E0;
Pb.k2=2;
Pb.k3=2*Pb.E0-0.2;
%% specify tU and U, data on neural activity (e.g. from another
   simulation)
tU = liley_sim.x/1000; %scale to the same unit
U = liley_sim.y(1,:);
i_unstim = find(tU > 0.1 & tU < 3);
Umin_unstim = min(U(i_unstim));
Umax_unstim = max(U(i_unstim));
Umean_unstim = mean(U(i_unstim));
U=(U-Umean_unstim)/(Umax_unstim-Umin_unstim);
%% initial values
x0=[0;1;1;1];
tint=[0,max(tU)];

%% structure for ordinary differential equation solver
options = odeset('RelTol',1e-9,'AbsTol',1e-9);
% it generates time courses for s (signal), v(blood volume), f(blood
```

```
    flow), q(deoxyhemoglobin)
l = ode23(@BalMod,tint,[0,1,1,1],options,Pb,tU,U);
%% extract q and v from l
v = l.y(3,:);
q = l.y(4,:);

%% calculate BOLD signal from q and v
y=Pb.V0*(7*Pb.E0*(1-q)+2*(1-q./v)+(2*Pb.E0-0.02)*(1-v));

%% plot BOLD signal
 figure(1)
 clf
plot(l.x,y)
%% plot the stimulus (normalised so it fits on same axis as BOLD)
hold on
plot(tU,U,'r')
xlabel('t','fontsize',16)
ylabel('BOLD','fontsize',16)
```

References

[1] LF Abbott. Lapicque's introduction of the integrate-and-fire model neuron (1907). *Brain Research Bulletin*, 50(5):303–304, 1999.

[2] Kevin M Aquino, Mark M Schira, Peter A Robinson, Peter M Drysdale, and Michael Breakspear. Hemodynamic traveling waves in human visual cortex. *PLoS Computational Biology*, 8(3):e1002435, 2012.

[3] Alfonso Araque, Vladimir Parpura, Rita P Sanzgiri, and Philip G Haydon. Tripartite synapses: Glia, the unacknowledged partner. *Trends in neurosciences*, 22(5):208–215, 1999.

[4] Owen J Arthurs and Simon Boniface. How well do we understand the neural origins of the fMRI BOLD signal? *Trends in Neurosciences*, 25(1):27–31, 2002.

[5] Sylvain Baillet, John C Mosher, and Richard M Leahy. Electromagnetic brain mapping. *Signal Processing Magazine*, 18(6):14–30, 2001.

[6] Jackson Beatty. *Principles of behavioral neuroscience*. Brown & Benchmark Publishers, 1995.

[7] Solenna Blanchard, Théo Papadopoulo, Christian-George Bénar, Nicole Voges, Maureen Clerc, Habib Benali, Jan Warnking, Olivier David, and Fabrice Wendling. Relationship between flow and metabolism in BOLD signals: Insights from biophysical models. *Brain Topography*, 24(1):40–53, 2011.

[8] Roman M Borisyuk and Alexandr B Kirillov. Bifurcation analysis of a neural network model. *Biological Cybernetics*, 66(4):319–325, 1992.

[9] E Brown, J Moehlis, and P Holmes. On the phase reduction and response dynamics of neural oscillator populations. *Neural Computation*, 16:673–71, 2004.

[10] Richard B Buxton, Kâmil Uludağ, David J Dubowitz, and Thomas T Liu. Modeling the hemodynamic response to brain activation. *Neuroimage*, 23:S220–S233, 2004.

[11] Richard B Buxton, Eric C Wong, and Lawrence R Frank. Dynamics of blood flow and oxygenation changes during brain activation: The Balloon model. *Magnetic Resonance in Medicine*, 39(6):855–864, 1998.

[12] Joana Cabral, Henrique M Fernandes, Tim J Van Hartevelt, Anthony C James, Morten L Kringelbach, and Gustavo Deco. Structural connectivity in schizophrenia and its impact on the dynamics of spontaneous functional networks. *Chaos: An Interdisciplinary Journal of Nonlinear Science*, 23(4):046111, 2013.

[13] José Javier Campos Bueno and Antonio Martin Araguz. Neuron doctrine and conditional reflexes at the xiv international medical congress of madrid of 1903. *Psychologia Latina*, 3(1):10–22, 2012.

[14] Carmen C Canavier. Phase response curve. *Scholarpedia*, 1(12):1332, 2006.

[15] BJ Casey, Matthew Davidson, and Bruce Rosen. Functional magnetic resonance imaging: Basic principles of and application to developmental science. *Developmental Science*, 5(3):301–309, 2002.

[16] Peter Chen. Principles of biological science. www.bio1152.nicerweb.com/ Locked/media/ch48/neuron.html, 2009.

[17] Eric H. Chudler. Neuroscience for kids; lights, camera, action potential. www.soton.ac.uk/jrc3/chudler/neurok.html, 2003.

[18] David Cohen. Magnetoencephalography: Evidence of magnetic fields produced by alpha-rhythm currents. *Science*, 161(3843):784–786, 1968.

[19] David Cohen and B Neil Cuffin. Demonstration of useful differences between magnetoencephalogram and electroencephalogram. *Electroencephalography and Clinical Neurophysiology*, 56(1):38–51, 1983.

[20] Stephen Coombes. Mathematical neuroscience. *Journal of Mathematical Biology*, 54(2):305–307, 2007.

[21] Stephen Coombes. Neuronal networks with gap junctions: A study of piecewise linear planar neuron models. *SIAM Journal on Applied Dynamical Systems*, 7(3):1101–1129, 2008.

[22] Stephen Coombes. Large-scale neural dynamics: Simple and complex. *Neuroimage*, 52(3):731–739, 2010.

[23] Fernando Lopes da Silva and A Van Rotterdam. *Electroencephalography: Basic principles, clinical applications and related fields*, chapter Biophysical aspects of EEG and Magnetoencephalogram generation, pages 107–126. Lippincott Williams & Wilkins, 2005.

[24] FH Lopes Da Silva, A Hoeks, H Smits, and LH Zetterberg. Model of brain rhythmic activity. *Kybernetik*, 15(1):27–37, 1974.

[25] Mathew P Dafilis, Federico Frascoli, Peter J Cadusch, and David TJ Liley. Chaos and generalised multistability in a mesoscopic model of the electroencephalogram. *Physica D: Nonlinear Phenomena*, 238(13):1056–1060, 2009.

[26] Olivier David and Karl J Friston. A neural mass model for MEG/EEG: Coupling and neuronal dynamics. *NeuroImage*, 20(3):1743–1755, 2003.

[27] Gustavo Deco, Giulio Tononi, Melanie Boly, and Morten L Kringelbach. Rethinking segregation and integration: Contributions of whole-brain modelling. *Nature Reviews Neuroscience*, 16(7):430–439, 2015.

[28] Hannah Devlin. What is functional magnetic resonance imaging (fMRI). *Psych Central. Accessed on June*, 16:2012, 2008.

[29] PM Drysdale, JP Huber, PA Robinson, and KM Aquino. Spatiotemporal BOLD dynamics from a poroelastic hemodynamic model. *Journal of Theoretical Biology*, 265(4):524–534, 2010.

[30] Albert Einstein. *Investigations on the Theory of the Brownian Movement*. Courier Corporation, 1956.

[31] Bard Ermentrout. Type I membranes, phase resetting curves, and synchrony. *Neural Computation*, 8(5):979–1001, 1996.

[32] G B Ermentrout. *Simulating, analyzing, and animating dynamical systems: A guide to XPPAUT for researchers and students*. SIAM Books, Philadelphia, 2002.

[33] Thomas Euler and Winfried Denk. Dendritic processing. *Current Opinion in Neurobiology*, 11(4):415–422, 2001.

[34] Andrew A Fingelkurts, Alexander A Fingelkurts, and Seppo Kähkönen. Functional connectivity in the brain. Is it an elusive concept? *Neuroscience & Biobehavioral Reviews*, 28(8):827–836, 2005.

[35] K Friston, C Price, D Glaser, A Mechelli, and R Turner. Haemodynamic modelling. In *Human Brain Function*, chapter 11. Academic Press, San Diego, CA, 2004.

[36] Karl J Friston. Functional and effective connectivity: A review. *Brain Connectivity*, 1(1):13–36, 2011.

[37] Karl J Friston et al. Functional and effective connectivity in neuroimaging: A synthesis. *Human Brain Mapping*, 2(1-2):56–78, 1994.

[38] Karl J Friston, Andrea Mechelli, Robert Turner, and Cathy J Price. Nonlinear responses in fMRI: The Balloon model, Volterra kernels, and other hemodynamics. *NeuroImage*, 12(4):466–477, 2000.

[39] KJ Friston, CD Frith, PF Liddle, and RSJ Frackowiak. Functional connectivity: The principal-component analysis of large (pet) data sets. *Journal of Cerebral Blood Flow and Metabolism*, 13:5–5, 1993.

[40] R F Galán, G B Ermentrout, and N N Urban. Efficient estimation of phase-resetting curves in real neurons and its significance for neural-network modeling. *Physical Review Letters*, 94:158101, 2005.

[41] Wulfram Gerstner and Werner M Kistler. *Spiking neuron models: Single neurons, populations, plasticity*. Cambridge University Press, 2002.

[42] Christian Giaume, Annette Koulakoff, Lisa Roux, David Holcman, and Nathalie Rouach. Astroglial networks: A step further in neuroglial and gliovascular interactions. *Nature Reviews Neuroscience*, 11(2):87–99, 2010.

[43] Pierre Gloor. Hans berger on electroencephalography. *American Journal of EEG Technology*, 9(1):1–8, 1969.

[44] Carmem Gottfried and Rudimar Riesgo. Antipsychotics in the treatment of autism. *Autism spectrum disorders: from genes to environment, T. Williams, Intech: Rijeka*, pages 23–46, 2011.

[45] W Govaerts and B Sautois. Computation of the phase response curve: A direct numerical approach. *Neural Computation*, 18:817–847, 2006.

[46] François Grimbert and Olivier Faugeras. Bifurcation analysis of Jansen's neural mass model. *Neural Computation*, 18(12):3052–3068, 2006.

[47] J Guckenheimer. Isochrons and phaseless sets. *Journal of Mathematical Biology*, 1:259–273, 1975.

[48] Boris S Gutkin, G Bard Ermentrout, and Alex D Reyes. Phase-response curves give the responses of neurons to transient inputs. *Journal of Neurophysiology*, 94(2):1623–1635, 2005.

[49] Peter Hansen, Morten Kringelbach, and Riitta Salmelin. *MEG: An introduction to methods*. Oxford University Press, 2010.

[50] J Woodland Hastings and Beatrice M Sweeney. A persistent diurnal rhythm of luminescence in gonyaulax polyedra. *The Biological Bulletin*, 115(3):440–458, 1958.

[51] Jan Hauke and Tomasz Kossowski. Comparison of values of pearson's and spearman's correlation coefficients on the same sets of data. *Quaestiones Geographicae*, 30(2):87–93, 2011.

[52] Jaroslav Hlinka and Stephen Coombes. Using computational models to relate structural and functional brain connectivity. *European Journal of Neuroscience*, 36(2):2137–2145, 2012.

[53] Alan L Hodgkin and Andrew F Huxley. A quantitative description of membrane current and its application to conduction and excitation in nerve. *The Journal of Physiology*, 117(4):500–544, 1952.

[54] Frank C Hoppensteadt and Eugene M Izhikevich. Weakly coupled neural networks, 1997.

[55] Barry Horwitz. The elusive concept of brain connectivity. *Neuroimage*, 19(2):466–470, 2003.

[56] Xiaoping Hu and Essa Yacoub. The story of the initial dip in fMRI. *Neuroimage*, 62(2):1103–1108, 2012.

[57] Scott A Huettel, Allen W Song, and Gregory McCarthy. *Functional magnetic resonance imaging*, volume 1. Sinauer Associates Sunderland, 2004.

[58] Eugene M Izhikevich. *Dynamical systems in neuroscience*. MIT Press, 2007.

[59] Eugene M Izhikevich and Yoshiki Kuramoto. Weakly coupled oscillators. *Encyclopedia of Mathematical Physics*, 5:448, 2006.

[60] Ben H Jansen and Vincent G Rit. Electroencephalogram and visual evoked potential generation in a mathematical model of coupled cortical columns. *Biological Cybernetics*, 73(4):357–366, 1995.

[61] Ben H Jansen, George Zouridakis, and Michael E Brandt. A neurophysiologically-based mathematical model of flash visual evoked potentials. *Biological cybernetics*, 68(3):275–283, 1993.

[62] Eric R. Kandel, J. H. Schwartz, and Thomas M. Jessell. *Principles of Neural Science*. McGraw-Hill Medical, 4th edition, July 2000.

[63] Kiyoshi Kotani, Ikuhiro Yamaguchi, Yutaro Ogawa, Yasuhiko Jimbo, Hiroya Nakao, and G. Bard Ermentrout. Adjoint method provides phase response functions for delay-induced oscillations. *Physical Review Letters*, 109:044101, 2012.

[64] Rolf Kötter. Online retrieval, processing, and visualization of primate connectivity data from the cocomac database. *Neuroinformatics*, 2(2):127–144, 2004.

[65] Thomas Kreuz. Measures of spike train synchrony. *Scholarpedia*, 6(10):11934, 2011.

[66] Y Kuramoto. Chemical oscillations, waves and turbulence. 1984.

[67] Kenneth K Kwong, John W Belliveau, David A Chesler, Inna E Goldberg, Robert M Weisskoff, Brigitte P Poncelet, David N Kennedy, Bernice E Hoppel, Mark S Cohen, and Robert Turner. Dynamic magnetic resonance imaging of human brain activity during primary sensory stimulation. *Proceedings of the National Academy of Sciences*, 89(12):5675–5679, 1992.

[68] Jean-Philippe Lachaux, Eugenio Rodriguez, Jacques Martinerie, Francisco J Varela, et al. Measuring phase synchrony in brain signals. *Human Brain Mapping*, 8(4):194–208, 1999.

[69] Elmar W Lang, AM Tomé, Ingo R Keck, JM Górriz-Sáez, and CG Puntonet. Brain connectivity analysis: A short survey. *Computational intelligence and neuroscience*, 2012:8, 2012.

[70] David TJ Liley, Peter J Cadusch, and Mathew P Dafilis. A spatially continuous mean field theory of electrocortical activity. *Network: Computation in Neural Systems*, 13(1):67–113, 2002.

[71] David TJ Liley, Peter J Cadusch, and James J Wright. A continuum theory of electro-cortical activity. *Neurocomputing*, 26:795–800, 1999.

[72] David TJ Liley, BL Foster, and I Bojak. A mesoscopic modelling approach to anaesthetic action on brain electrical activity. In *Sleep and Anesthesia*, pages 139–166. Springer, 2011.

[73] Pierre-Marie Lledo, Armen Saghatelyan, and Morgane Lemasson. Inhibitory interneurons in the olfactory bulb: From development to function. *The Neuroscientist*, 10(4):292–303, 2004.

[74] Nikos K Logothetis and Brian A Wandell. Interpreting the bold signal. *Annu. Rev. Physiol.*, 66:735–769, 2004.

[75] Michael Luchtmann, Katja Jachau, Daniela Adolf, Friedrich-Wilhelm Röhl, Sebastian Baecke, Ralf Lützkendorf, Charles Müller, and Johannes Bernarding. Ethanol modulates the neurovascular coupling. *Neurotoxicology*, 34:95–104, 2013.

[76] Gisiro Maruyama. Continuous markov processes and stochastic equations. *Rendiconti del Circolo Matematico di Palermo*, 4(1):48–90, 1955.

[77] Sergei Maslov and Kim Sneppen. Specificity and stability in topology of protein networks. *Science*, 296(5569):910–913, 2002.

[78] Ali Mazaheri and Ole Jensen. Rhythmic pulsing: Linking ongoing brain activity with evoked responses. *Frontiers in Human Neuroscience*, 4(0), 2010.

[79] Florian Mormann, Klaus Lehnertz, Peter David, and Christian E Elger. Mean phase coherence as a measure for phase synchronization and its application to the EEG of epilepsy patients. *Physica D: Nonlinear Phenomena*, 144(3):358–369, 2000.

[80] Suhita Nadkarni and Peter Jung. Dressed neurons: Modeling neural–glial interactions. *Physical Biology*, 1(1):35, 2004.

[81] T Netoff, M A Schwemmer, and T J Lewis. *Phase response curves in neuroscience: Theory, experiment, and analysis*, chapter Experimentally estimating phase response curves of neurons: Theoretical and practical issues, pages 95–129. Springer, Berlin, 2012.

[82] Ernst Niedermeyer and FH Lopes da Silva. *Electroencephalography: Basic principles, clinical applications, and related fields*. Lippincott Williams & Wilkins, 2005.

[83] Viktor Novičenko and Kestutis Pyragas. Computation of phase response curves via a direct method adapted to infinitesimal perturbations. *Nonlinear Dynamics*, 67(1):517–526, 2012.

[84] V Novičenko and K Pyragas. Phase reduction of weakly perturbed limit cycle oscillations in time-delay systems. *Physica D*, 241:1090–1098, 2012.

[85] Takayuki Obata, Thomas T Liu, Karla L Miller, Wen-Ming Luh, Eric C Wong, Lawrence R Frank, and Richard B Buxton. Discrepancies between BOLD and flow dynamics in primary and supplementary motor areas: application of the Balloon model to the interpretation of BOLD transients. *NeuroImage*, 21(1):144–153, 2004.

[86] Hae-Jeong Park and Karl Friston. Structural and functional brain networks: From connections to cognition. *Science*, 342(6158):1238411, 2013.

[87] George Howard Parker. *The elementary nervous system*, volume 1920. JB Lippincott, 1919.

[88] WD Penny, V Litvak, L Fuentemilla, E Duzel, and K Friston. Dynamic causal models for phase coupling. *Journal of Neuroscience Methods*, 183(1):19–30, 2009.

[89] Gertrudis Perea, Marta Navarrete, and Alfonso Araque. Tripartite synapses: Astrocytes process and control synaptic information. *Trends in Neurosciences*, 32(8):421–431, 2009.

[90] Arkady Pikovsky, Michael Rosenblum, and Jürgen Kurths. *Synchronization: A universal concept in nonlinear sciences*, volume 12. Cambridge University Press, 2003.

[91] Adrián Ponce-Alvarez, Gustavo Deco, Patric Hagmann, Gian Luca Romani, Dante Mantini, and Maurizio Corbetta. Resting-state temporal synchronization networks emerge from connectivity topology and heterogeneity. *PLoS Computational Biology*, 11(2):e1004100, 2015.

[92] Liina Pylkkanen. Functional neuroimaging. www.psych.nyu.edu/pylkkanen/NeuralBases/07slides/05Methods.pdf, 2005.

[93] Wilfrid Rall. Electrophysiology of a dendritic neuron model. *Biophysical Journal*, 2(2 Pt 2):145, 1962.

[94] John Rinzel and G Bard Ermentrout. *Methods in Neuronal Modeling: From Synapses to Networks*, chapter Analysis of neural excitability and oscillations, pages 135–169. MIT Press, Cambridge Massachusetts, 1st edition, 1989.

[95] Paulo N Rosa, Patricia Figueiredo, and Carlos J Silvestre. On the distinguishability of HRF models in fMRI. *Frontiers in Computational Neuroscience*, 9:54, 2015.

[96] A Van Rotterdam, FH Lopes Da Silva, J Van den Ende, MA Viergever, and AJ Hermans. A model of the spatial-temporal characteristics of the alpha rhythm. *Bulletin of mathematical biology*, 44(2):283–305, 1982.

[97] Elena Rykhlevskaia, Gabriele Gratton, and Monica Fabiani. Combining structural and functional neuroimaging data for studying brain connectivity: A review. *Psychophysiology*, 45(2):173–187, 2008.

[98] Timothy Sauer. Numerical solution of stochastic differential equations in finance. In *Handbook of Computational Finance*, pages 529–550. Springer, 2012.

[99] Nathan W Schultheiss, Astrid A Prinz, and Robert J Butera. *Phase response curves in neuroscience: Theory, experiment, and analysis*. Springer Science & Business Media, 2011.

[100] Michael A Schwemmer and Timothy J Lewis. The theory of weakly coupled oscillators. In *Phase Response Curves in Neuroscience*, pages 3–31. Springer, 2012.

[101] Farzaneh Shayegh, Jean-Jacques Bellanger, Saied Sadri, Rasoul Amirfattahi, Karim Ansari-Asl, and Lotfi Senhadji. Analysis of the behavior of a seizure neural mass model using describing functions. *Journal of Medical Signals and Sensors*, 3(1):2, 2013.

[102] Zarrar Shehzad, AM Clare Kelly, Philip T Reiss, Dylan G Gee, Kristin Gotimer, Lucina Q Uddin, Sang Han Lee, Daniel S Margulies, Amy Krain Roy, Bharat B Biswal, et al. The resting brain: Unconstrained yet reliable. *Cerebral cortex*, 19(10):2209–2229, 2009.

[103] Roy M Smeal, G Bard Ermentrout, and John A White. Phase-response curves and synchronized neural networks. *Philosophical Transactions of the Royal Society B: Biological Sciences*, 365(1551):2407–2422, 2010.

[104] Stephen M Smith, Peter T Fox, Karla L Miller, David C Glahn, P Mickle Fox, Clare E Mackay, Nicola Filippini, Kate E Watkins, Roberto Toro, Angela R Laird, et al. Correspondence of the brain's functional architecture during activation and rest. *Proceedings of the National Academy of Sciences*, 106(31):13040–13045, 2009.

[105] Roberto C Sotero and Nelson J Trujillo-Barreto. Modelling the role of excitatory and inhibitory neuronal activity in the generation of the BOLD signal. *Neuroimage*, 35(1):149–165, 2007.

[106] Roberto C Sotero and Nelson J Trujillo-Barreto. Biophysical model for integrating neuronal activity, EEG, fMRI and metabolism. *Neuroimage*, 39(1):290–309, 2008.

[107] Murray R Spiegel and John J Schiller. Schaums outline. *Probability and Statistics*, 2000.

[108] Olaf Sporns. Brain connectivity. www.scholarpedia.org/article/Brainconnectivity, 2007.

[109] Olaf Sporns. *Networks of the Brain*. MIT Press, 2011.

[110] Ramesh Srinivasan. Methods to improve the spatial resolution of EEG. *International Journal of Bioelectromagnetism*, 1(1):102–111, 1999.

[111] E M Tansey. Not committing barbarisms: Sherrington and the synapse, 1897. *Brain Research Bulletin*, 44(3):211–212, 1997.

[112] Huizhong W Tao and Mu-ming Poo. Activity-dependent matching of excitatory and inhibitory inputs during refinement of visual receptive fields. *Neuron*, 45(6):829–836, 2005.

[113] Peter Tass, MG Rosenblum, J Weule, J Kurths, A Pikovsky, J Volkmann, A Schnitzler, and H-J Freund. Detection of n:m phase locking from noisy data: Application to magnetoencephalography. *Physical Review Letters*, 81(15):3291, 1998.

[114] T Tateno and H P C Robinson. Phase resetting curves and oscillatory stability in interneurons of rat somatosensory cortex. *Biophysical Journal*, 92:683–695, 2007.

[115] Robert W Thatcher. EEG operant conditioning (biofeedback) and traumatic brain injury. *Clinical EEG and Neuroscience*, 31(1):38–44, 2000.

[116] Robert Ton, Gustavo Deco, and Andreas Daffertshofer. Structure-function discrepancy: Inhomogeneity and delays in synchronized neural networks. *PLoS Computational Biology*, 10(7), 2014.

[117] Jonathan Touboul, Fabrice Wendling, Patrick Chauvel, and Olivier Faugeras. Neural mass activity, bifurcations, and epilepsy. *Neural Computation*, 23(12):3232–3286, 2011.

[118] Nicole Voges, Solenna Blanchard, Fabrice Wendling, Olivier David, Habib Benali, Théodore Papadopoulo, Maureen Clerc, and Christian Bénar. Modeling of the neurovascular coupling in epileptic discharges. *Brain Topography*, 25(2):136–156, 2012.

[119] Hugh R Wilson and Jack D Cowan. Excitatory and inhibitory interactions in localized populations of model neurons. *Biophysical Journal*, 12(1):1, 1972.

[120] Hugh R Wilson and Jack D Cowan. A mathematical theory of the functional dynamics of cortical and thalamic nervous tissue. *Kybernetik*, 13(2):55–80, 1973.

[121] A Winfree. *The Geometry of Biological Time*. Springer-Verlag, New York, 2nd edition, 2001.

[122] Lillian Xue and Stephanie Ganzeveld. Magnetic resonance imaging. www.slideshare.net /sganzeveld29/mri-presentation-final, 2013.

[123] Edward Zamrini, Fernando Maestu, Eero Pekkonen, Michael Funke, Jyrki Makela, Myles Riley, Ricardo Bajo, Gustavo Sudre, Alberto Fernandez, Nazareth Castellanos, et al. Magnetoencephalography as a putative biomarker for alzheimer's disease. *International Journal of Alzheimers disease*, 2011.

[124] Chadia Zayane and Taous Meriem Laleg-Kirati. A sensitivity analysis of fMRI Balloon model. *Computational and Mathematical Methods in Medicine*, 2015.